2021-04-08

Investigation of Water Imbibition Behavior in Nanopores in Shale Reservoirs

Zhang, Linyang

UNIVERSITY OF CALGARY

Investigation of Water Imbibition Behavior in Nanopores in Shale Reservoirs

by

Linyang Zhang

A THESIS

SUBMITTED TO THE FACULTY OF GRADUATE STUDIES

IN PARTIAL FULFILMENT OF THE REQUIREMENTS FOR THE

DEGREE OF DOCTOR OF PHILOSOPHY

GRADUATE PROGRAM IN CHEMICAL AND PETROLEUM ENGINEERING

CALGARY, ALBERTA

APRIL, 2021

Abstract

Shale gas is emerging as an important source of energy supply worldwide. The economic production of shale gas has become feasible because of the increasing global energy demand and advanced multistage hydraulic fracturing technologies. A huge amount of a fracturing fluid is usually injected into a shale formation during a fracturing process, but only a small fraction of the fracturing fluid can be recovered. The main reason for the low recovery of a fracturing fluid is the spontaneous imbibition of the fracturing water into the shale matrix. The current understanding of the water imbibition behavior in shale is still poor, since a pore network of shales is usually complex and heterogeneous, consisting of abundant nanopores. At such confined conditions, a surface to volume ratio is very large and surface forces dominate over volume forces. Therefore, the characteristics of a solid surface have crucial effects on flow properties, and macroscopic hydrodynamic models are insufficient to be applied to water imbibition behavior in shale. To investigate water imbibition behavior in shale and develop its theoretical models, unique properties should be considered, including the slip behavior, an increased viscosity effect, a dynamic contact angle, and the propagation of precursor films. In this thesis, the dynamics of water flow in a quasi-continuum flow regime are investigated. The mechanisms of friction at a liquid-solid interface are firstly investigated, and a relationship between the friction and the slip velocity is established. Moreover, a theoretical model for the effective viscosity of water in nanopores is proposed based on a molecular kinetic Theory, and the factors that affect the effective viscosity are discussed. Besides, a unified model in a quasi-continuum flow regime is established by inserting the effective viscosity model and a slip length model into the traditional Hagen-Poiseuille model. The impact of the wettability condition on the effective viscosity is investigated. Furthermore, the spreading of precursor films is investigated. A model for water imbibition in nanopores is proposed, considering the propagation of the precursor films ahead of a main meniscus. All the models proposed in this thesis have been validated by experimental and simulation results in the literature. The research results in this thesis can be beneficial to an understanding of the water flow behavior in nanopores and will have many applications in the chemical and petroleum industry.

ACKNOWLEDGMENTS

I would like to express my gratitude to my supervisor, Dr. Zhangxing (John) Chen, and Dr. Keliu Wu, for their support, encouragement, and supervision during my doctoral study in the Department of Chemical and Petroleum Engineering. They have provided me with a precious opportunity, academic vision, valuable advice, and encouragement to enable me to pursue challenging problems in my dissertation. I have benefited from their excellent guidance, technical discussions, paper revisions, and great patience. Their support and encouragement in all aspects, both academically and personally, have helped me complete my research work and thesis.

I would like to express my appreciation to Dr. Hassan Hassanzadeh and Dr. Hemanta Sarma from the Department of Chemical and Petroleum Engineering, Dr. Peter Kusalik from the Department of Chemistry, and Dr. Amy Tsai from the University of Alberta for serving on my dissertation committee.

My appreciation is also extended to every team member in the Reservoir Simulation Group, including project managers, research associates, post-doctoral fellowships, and previous and current students. They provided open communications and discussions during my study and life. I am truly grateful to my family members and friends for personal encouragement during my study at the University of Calgary.

Table of Contents

List of Tables

List of Figures

Nomenclature

A_{H}	Hamaker constant
ε_0	Permittivity of vacuum
ε_r	Relative permittivity of film
ζ	Electric potentials of an interface
k	Constant of structural force
h^*	Critical thickness
μ_{bulk}	Bulk fluid viscosity
γ	Surface tension between the wetting and non-wetting fluids
θ_{e}	Contact angle at equilibrium condition
λ	The average length of the molecular displacement
k_{B}	Boltzmann's constant
T	Temperature
F_{f}	Force exerted by the surface friction on the liquid motion
N_{coll}	Number of particle collisions with the solid wall
m	Mass of the particles colliding with the wall
Δu_{w}	Mean velocity change for the particles
S_0	Initial spreading coefficient
S	Spreading coefficient under the equilibrium state
f_{Y}	Young capillary force per unit length of a contact line
σ_{lg}	The surface tension of a liquid-vapor interface
θ_{t}	Dynamic contact angle
σ_{sg}	The surface tension of a dry solid substrate in contact with a gas
σ_{sl}	Solid-liquid interfacial tension
L_{f}	Length of the precursor film
V	The velocity of the meniscus
Π	Disjoining pressure
h	Distance to a solid surface
$\Delta\zeta$	Difference of the electric potentials of two interfaces separating the film
κ	Reciprocal of the Debye length
D_{f}	Self-diffusion coefficient
r_{ij}	Intersite distance between atoms
$\varepsilon_{\mathrm{ij}}$	Well depth
σ_{ij}	Size parameter
r_{cutoff}	Cut-off radius
ν	Hopping rate
h_{P}	Planck constant
ΔG_0	Energy barrier
F_{a}	An external force acting on the molecule
δ	Length for each hopping event

τ	Shear stress
V_{m}	Molecular volume
ΔE	A variance of the total potential energy
f_{N}	External normal load
Δz	Vertical distance
ΔE_{ad}	Adsorption energy difference at different sites
f_{x}	Position-dependent force
f_{f}	Friction force
Δx	Distance of one period of the movement
f_{ext}	Force pointing downward to graphene
f_{rep}	Force pointing upward
P_{IJ}	Pressure tensor
N	Number of atoms in the system
N’	All atoms in the system and periodic image atoms outside the central box
Z	Vertical position to a solid surface
N_{t}	Number of total water molecules in the system
N_{s}	Number of water molecules in the two slip planes
U	Internal energy
f	A fitting factor
σ_{LL}	The liquid-liquid L-J size parameter
σ_{LS}	Liquid-solid L-J size parameter
l	Distance to a solid surface
W	Channel width
H	Channel height
r^*	Distance from the boundary of the two water density layers to the middle of the streamline
D	Diameter of a nano capillary tube
P_{C}	Capillary pressure
K	pErmeability
μ_{eff}	effective viscosity
l_{s}	Slip length
μ_{le}	local effective viscosity
L	The imbibition length
t	Time
R'	The radius of the macroscopic region in the capillary tube
H'	A macroscopic region in the channel
κ^0	Rate of the hopping process
ρ_{b}	Bulk phase density
ρ	The density of the solidified water layers and the precursor films
A_{f}	The cross-section area of the precursor film
A_{m}	The cross-section area of the macroscopic region
MD	Molecular Dynamics

OM	Organic matters
TOC	Total organic content
BSE	Backscattered electron
L-W	Lucas-Washburn
EDL	Electrical double layer
DL	Debye length
TPCL	Three-phase-contact-line
vdW	van der Waals
U_{bond}	The potential energy of bond stretching
U_{angle}	Potential energy required to bend the angle formed by three atoms
L-J	Lennard-Jones
LAMMPS	Large-scale Atomic/Molecular Massively Parallel Simulator
OVITO	Open Visualization Tool
GCMC	Grand Canonical Monte Carlo
NEMD	Non-Equilibrium Molecular Dynamic
EMD	Equilibrium Molecular Dynamic
LB	Lattice Boltzmann

CHAPTER 1 Introduction

1.1 Problem Statement

Shale gas has become an important source of energy supply. The increasing global energy demand coupled with the advanced multistage hydraulic fracturing technologies has shifted the attention of the petroleum industry to shale gas reservoirs [1–3]. During a fracturing process, a huge amount of a fracturing fluid is injected into a shale formation to create fractures. However, most field observations found that only a small fraction of the fracturing fluid can be recovered during a flowback process [4–6]. The main reason for the low recovery of a fracturing fluid is the spontaneous imbibition of a fracturing water into the shale matrix [7,8]. In addition to the petroleum industry, understanding and modeling dynamic imbibition behaviors of fluids through nanopores have numerous applications in the chemical engineering field, such as energy conversion/storage and next-generation seawater desalination [9–13]. Many processes, such as imbibition of liquid reactants into pores in porous catalysts and adsorbents in reactor beds, and spreading of liquid condensate on fuel cell membranes, require a deep understanding of dynamic imbibition for fluids.

The current understanding of the water imbibition behavior in nanopores is still poor, which hinders the recognition of water distributions in shale formations. The primary reason for the lack of understanding this topic lies in that a pore network of shales is usually complex and heterogeneous, consisting of abundant micropores and nanopores [14,15]. At such confined conditions, the water flow properties are different from the macroscopic hydrodynamics, as a surface to volume ratio can be very large at the nanoscale, and the effect of a solid surface cannot be neglected [16–19]. This is because the interactions between the solid substrate will be different compared with the interactions within water molecules. As water molecules near a solid surface will interact with both surrounding water molecules and solid molecules, the flow properties of water near a solid surface will be modified. Hydrodynamics at the

macroscale is dominated by viscous forces within fluids and the Navier-Stokes equations hold at such a continuum condition. However, surface forces dominate over volume forces at the nanoscale, and thus the characteristics of a solid surface, such as wettability and surface roughness, have crucial effects on the flow properties at the nanoscale [20,21]. Therefore, theoretical models used in the macroscopic hydrodynamics are insufficient to be applied to water imbibition behavior in shale. To investigate this research topic, an approach is to quit the continuum level and turn directly to the atomistic description of fluid flows as a collection of moving molecules. However, this is computationally demanding, which prevents the attainment of space and time macroscopic scales of experimental interest. Theoretical models that can be applied in the water imbibition problems are still lacking.

To propose theoretical models for water imbibition in shale, unique properties should be considered. Many phenomena exist for flowing water under nanoconfined conditions. The first one is the slip behavior for water near a solid surface. The traditional no-slip boundary condition that can apply to macro-hydrodynamics will be significantly violated when the flow dimension is down to nanometers. Besides, a density profile is usually inhomogeneous. Many Molecular Dynamics (MD) simulations showed that there were density layering phenomena for water molecules near a solid surface, indicating density peaks within a water boundary layer [22–29]. This arises from strong interactions between water molecules and the solid surface. Moreover, viscosity was found to be spatially varying for water flow under nanoconfined conditions, and the effective viscosity was different under various wettability conditions. MD simulations performed by Sendner showed that on hydrophobic surfaces the water dynamics were purely diffusive, while transient binding or trapping of water over times of the order of hundreds of picoseconds occurred for water close to a hydrophilic surface [26]. Accordingly, it was demonstrated that excess water in an interface region at the hydrophobic condition diffused faster compared with the bulk phase [26,27,30–33]. Besides, the viscosity in a water boundary layer under hydrophilic conditions was higher than the bulk phase due to stronger interactions with a solid surface [34–39]. Furthermore, a research topic that draws

increasingly wide attention is the fluid imbibition behavior in nanopores with the existence of precursor films. The precursor film propagation is a prevalent phenomenon during a wetting process, which may occur for water imbibition in a shale formation. Additionally, there are many other unique phenomena for water flow at the nanoscale, such as hydrogen bonding depletion [40,41], electrostatics in surface-charge-governed transport [42], and single-file flow under extreme confinement [35]. All these phenomena and their applications in engineering problems require further research in nanofluidics, in terms of experiments, computational work, and theoretical investigations.

In this thesis, the dynamics of water flow in a quasi-continuum flow regime are investigated. This precondition indicates a bulk phase flow in the middle of a flow region and a unique boundary flow near a solid surface [43]. Thus, the continuum theory is still valid, as a bulk phase exists. According to the definitions of the continuum system, the behavior of a liquid can be described in terms of infinitesimal volumetric elements that are small compared to the flow domain but have well-defined thermophysical properties. Newton's second law can be applied to such a system and the Cauchy and Navier-Stokes equations can be obtained. However, in a system where the size of a liquid molecule is comparable to the size of the flow domain, the notion of a representative volumetric element is invalid and the continuum-based relations are violated. Within such subcontinuum systems, the movement of individual molecules must be considered when predicting mass and momentum transport. In this work, the quasi-continuum flow regime is investigated, and the proposed models can be applied at a continuum level, rather than a molecule level, and the parameters used in the models are macro-scale parameters.

Moreover, a region under the influence of solid surfaces may take a non-negligible proportion of the whole cross-section for fluid flow in nanopores, and thus the unique physics of a fluid near the solid surfaces need to be considered [16,17]. It was confirmed that for simple fluids, there is no expected deviation from the continuum framework of hydrodynamics for confinement larger than around 1 nm [44–47]. Chan and Horn predicted that the Reynolds formula was valid for confinement larger than typically ten molecular

diameters [48]. Moreover, MD simulations were also applied to investigating a threshold for the validity of the continuum hydrodynamics, and a value of approximately 1.66 nm for water was achieved by Thomas and McGaughey [49–51]. They examined the structure and flow of water inside carbon nanotubes with diameters ranging from 0.83 to 1.66 nm using MD simulation. Below a tube diameter of 1.66 nm, the bulklike water structure vanishes and the water structure becomes stacked hexagonal rings. Besides, the relationship between the flow enhancement and the tube diameter becomes nonlinear when the tube diameter is below 1.66 nm. This threshold may be various for other solid materials. In this work, the proposed models can only be applied for water flow behavior confined in nanopores with a diameter of larger than 1~2 nm.

Most of the research in this thesis is theoretical work. MD simulations are applied in topic 1 to validate the proposed model, and the last three topics use experimental results reported in the literature to validate the proposed models. Experiments are not performed in this work.

1.2 Objectives

The primary aim of this thesis is to investigate mechanisms of water imbibition at the molecular scale and develop theoretical approaches to model water imbibition in shale formations. Four specific objectives are listed as follows:

1) Investigate the mechanisms of friction between water and a solid surface and propose theoretical foundations between a friction force and a slip velocity;
2) Examine the impact of surface forces on water flow properties and propose a theoretical model for the spatially varying viscosity phenomena for water imbibition in shale;
3) Propose unified approaches to model water imbibition behavior under various wettability conditions for a quasi-continuum water flow problem;
4) Investigate the spreading behavior of precursor films and propose theoretical models for the capillary dynamics with the existence of the precursor films.

The novelties in this thesis are summarized as follows.

For the first topic, this can be discussed in two aspects. The first one is that similar mechanisms among all friction processes are found. In literature, the mechanisms of liquid-solid friction are commonly distinguished from those of solid-solid friction and friction within liquids. In this work, it is found that for simple structure particles, the friction mechanisms among all friction processes may be similar, in terms of energy barrier. The second one is that there are some papers on the relationship between the friction force and the slip velocity, but the authors only use MD simulations to obtain this relation. In this work, the molecular kinetic theory is applied to establish this relation, and MD simulations are used to validate it. A theoretical relation with clear physical meanings is obtained.

The other three topics talk about the water imbibition behavior in nanopores. There are two main contributions. First, a theoretical model for the effective viscosity is proposed and validated. There are some effective viscosity models in the literature, but most of them have drawbacks. In some models, the authors divided the flow region into the bulk phase and the interface region, and then use two constant viscosity values in the two regions. This assumption cannot be argued, because the viscosity is spatially varying, and it should be a function of the distance to a solid surface. Besides, some authors use fitting parameters in the models, which have no clear physical meanings. There are no such limitations in the proposed model in this work. The second one is that the dynamics of the precursor films are investigated in the context of the capillary filling process. Very few works have been directed to the study of precursor films for the case of capillary filling, and no theoretical models can be found in the literature. To the best of my knowledge, this is the first theoretical model to describe the capillary dynamics with the precursor films in a capillary filling problem.

The main results obtained in this work can be widely applied in the petroleum and chemical engineering industry.

First, the proposed models can guide the field operations on soaking processes. During the production of shale gas, many oilfield cases have confirmed the validity of soaking to increase production. But the estimation of the invasion depth of fracturing water requires theoretical models. Therefore, understanding the water imbibition behavior can help to make better strategies on the soaking processes.

Second, the proposed models can help to recognize the water distribution in the shale formation. Some researchers showed that fracturing water may migrate upward from a shale formation and enter a shallow aquifer, but some other scholars suggested that this is impossible. Understanding water imbibition can help to resolve this issue. Finally, the proposed theoretical models in this thesis can be used for the simulation of fluid flow in unconventional reservoirs, because theoretical models for water imbibition in shale are still lacking.

Besides, in the chemical engineering industry, there are also numerous applications, such as energy conversion/storage and next-generation seawater desalination. Many processes require a deep understanding of imbibition behavior for fluids, such as imbibition of liquid reactants into porous catalysts and adsorbents in reactor beds, and spreading of liquid condensate on fuel cell membranes. For example, in topic 4 of this thesis, the propagation of the precursor films is investigated, and it is found that the dynamic contact angle has a minimal effect on the capillary dynamics for a complete wetting case. So, the propagation of the precursor films may improve the nano-channel-coating efficiency. This finding can be applied to hide the chemical and geometrical details of the nano-channel walls, and making better strategies on the nano-channel–coating problems.

1.3 Outline

There are seven chapters in this thesis. The first chapter introduces the research topic, major challenges, and primary research objectives. The second chapter presents a literature review on five parts, including characteristics of shale reservoirs, an introduction of hydraulic fracturing and flowback processes, water imbibition behavior in shale formations, unique water flow phenomena under nanoconfined conditions,

and an introduction of the molecular kinetic theory. The third chapter proposes the computation of the friction force and discusses its relationship with the slip behavior. The fourth chapter establishes a theoretical model for the effective viscosity, and the fifth chapter discusses a quasi-continuum flow problem under various wettability conditions. In the sixth chapter, the behavior of precursor films are investigated, and the main conclusions are given in the seventh chapter, the last chapter.

Chapter 2 Literature Review

2.1 Shale reservoirs

The world energy market has witnessed a significant increase in the production of unconventional reservoirs in recent years, the primary of which is shale gas reservoirs. Given that the enormous potential for shale gas resources, the economic production of shale gas exerts profound effects on the global energy market where conventional supplies are already on the decline, but the energy demand is on the rise [52]. Apart from its huge geological storage, one more important advantage of shale gas is the cleanness and efficiency compared with traditional fossil fuels, which contributes to reducing air pollutants and greenhouse emissions [53,54]. Owing to advances in multistage hydraulic fracturing and policy support, the development of shale gas resources has made a series of breakthroughs throughout the world. The global shale gas resources are fairly abundant and widely distributed, and the recoverable shale gas resources are estimated to be approximately 2.21×10^{14} m^3 under current technical and economic conditions, accounting for nearly one-third of total natural gas resources [55]. **Figure 2.1** shows the top 10 countries holding the largest resources of shale gas. Among these countries, the United States was the first one to achieve success in the development of shale gas resources, followed by Canada and China. Other resource-rich countries, such as Argentina and Algeria, also promoted the exploitation of shale gas [56–58]. The abundant explored resources coupled with the technical revolutions indicate the huge potential to develop shale gas, which has profound effects on the global energy and petroleum industry.

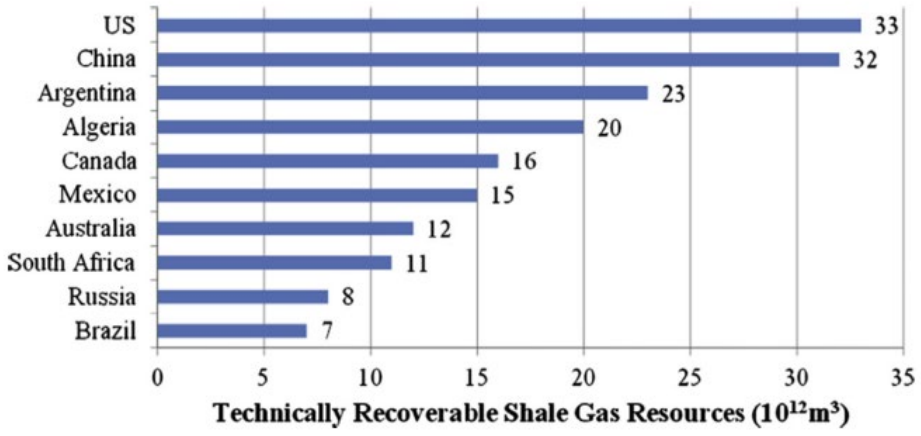

Figure 2. 1 Top 10 countries with technically recoverable shale gas resources [55]

The extraction of shale gas is much more expensive compared with conventional natural gas resources. Despite the abundant storage of gas, economic production can be achieved only when their flow properties are enhanced by artificially induced fractures. The primary reason lies in the special geological characteristics of the shale reservoirs.

The shale formations are composed of organic-rich mudstones, which act as seals and flow barriers in conventional reservoirs due to their low permeability and high capillary entry pressure [59]. Commonly, the mudstones in shale comprise a mixture of clay minerals, non-clay minerals, and organic matter [60–66]. Clay minerals include illite, chlorite, smectite, kaolinite and non-clay minerals consist of quartz, chert, and feldspar. Organic matters (OM), denoted by the total organic carbon content, are mainly kerogen which is composed of carbon, hydrogen, oxygen, nitrogen, and smaller amounts of sulfur. Milliken et al. examined many shale rock samples from the Marcellus Formation of Pennsylvania, and they found that the Total organic carbon content (TOC) ranges from 2.3 % to 13.6 % [65]. Although OM only takes a small percentage of the total weight, it usually acts as a significant source for gas storage, owing to its advantages for gas adsorption, such as low density and varying wettability [67,68].

The pore network of shales is complex and heterogeneous, consisting of abundant micropores (< 2 nm), mesopores (2-50 nm), and macropores [14]. **Figure 2.2** illustrates the pore size distribution estimated from

the Horn River reconstruction which indicates that small pores dominate in number [69]. The larger internal surface area in the micropores contributes the majority to gas adsorption and storage in reservoirs compared to macropores and mesopores. However, the macropores and mesopores provide a connected pathway for fluids to flow through micropores and play an important role in establishing pore networks of shale matric and fracture systems. Chalmers et al. examined the pore system of cores obtained from the Barnett, Marcellus, Woodford, Haynesville shale formations in the United States, and Doig formation of northeastern British Columbia, Canada [70]. Results showed that the gas shales in the United States are clay and quartz-rich, while the Doig Formation samples are quartz and carbonate dominated. Total porosity from helium pycnometry ranges from 2.5 to 6.6%, TOC content ranges between 0.7 and 6.8 wt. % and vitrinite reflectance measured between 1.45 and 2.37%.

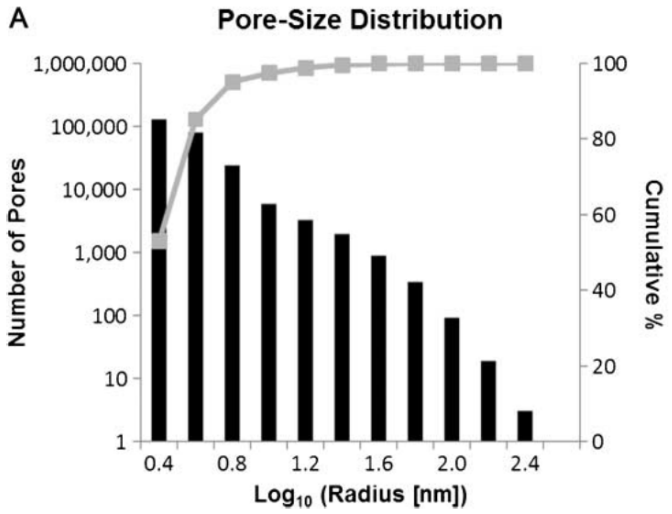

Figure 2. 2 The pore size distribution estimated from the Horn River reconstruction [69]

The shale rocks are usually classified by clay content, TOC, and porosity. For example, the Upper Wood Formation is characterized as high quartz content, low TOC, and high porosity [71]. In addition, much research focused on the classification of the pore types of the shale formations. The types of pores in shale formations are various. Loucks et al. gave a pore classification consisting of interparticle pores, intraparticle pores, and organic-matter pores. The interparticle pores are found between particles and

crystals, intraparticle pores are located within particles and organic-matter pores are intraparticle pores located within OM [72]. The former two pore types are associated with the mineral matrix while the third pore type is associated with OM. Interparticle mineral pores have a higher probability of being part of an effective pore network than intrapartical mineral pores because they are more likely to be interconnected. Besides, OM pores are also likely to be part of an interconnected network because of the interconnectivity of OM particles although they are intrapartical pores.

Moreover, a variety of shapes of the pores can be detected in porous systems, such as slit-type pores, cylindrical-type pores, and cross-linked pores [73]. A backscattered electron (BSE) image of a cross-sectioned Haynesville Shale sample is demonstrated in **Figure 2.3** [69]. Phyllosilicate porosity in the form of triangular and linear pores can be seen. Many other scholars also verified that the number of slit pores is huge in shale formations.

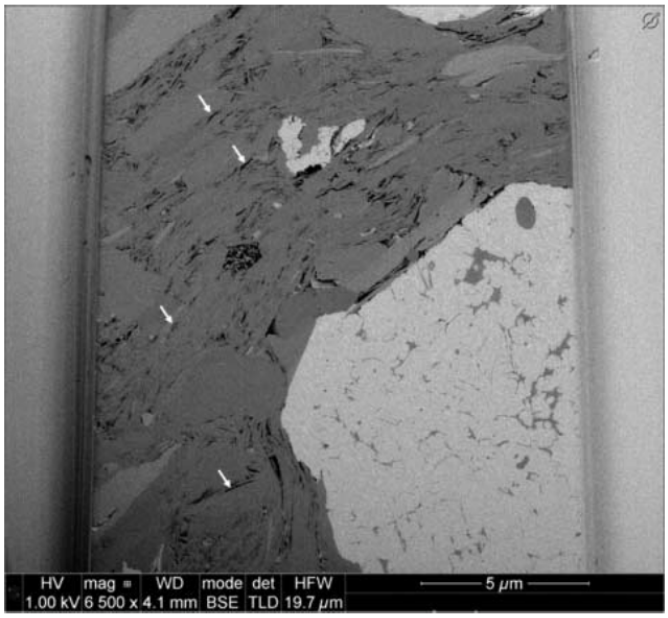

Figure 2. 3 Backscattered electron (BSE) image of a cross-sectioned Haynesville Shale sample [69]

2.2 Hydraulic fracturing and flowback fluid

It is acknowledged that the traditional exploitation operations cannot efficiently extract hydrocarbons to the ground from shale formations. Hydraulic fracturing (HF) is the primary technology employed to break

the rock matrix and establish a high-permeable pathway to obtain an economical production. Such stimulating techniques are usually coupled with more recent advances in horizontal drilling [74]. Generally, large volumes of proppant, a mixture of chemicals, sands, and water, are injected under high pressure into low permeable reservoirs during hydraulic fracturing operations. The high-pressure stimulation creates fractures in the rock and small fractures are induced during multi-stage hydraulic fracturing operations, which usually extend 100 to 200 meters in the matrix [75]. The overview of this process is illustrated in **Figure 2.4** [76].

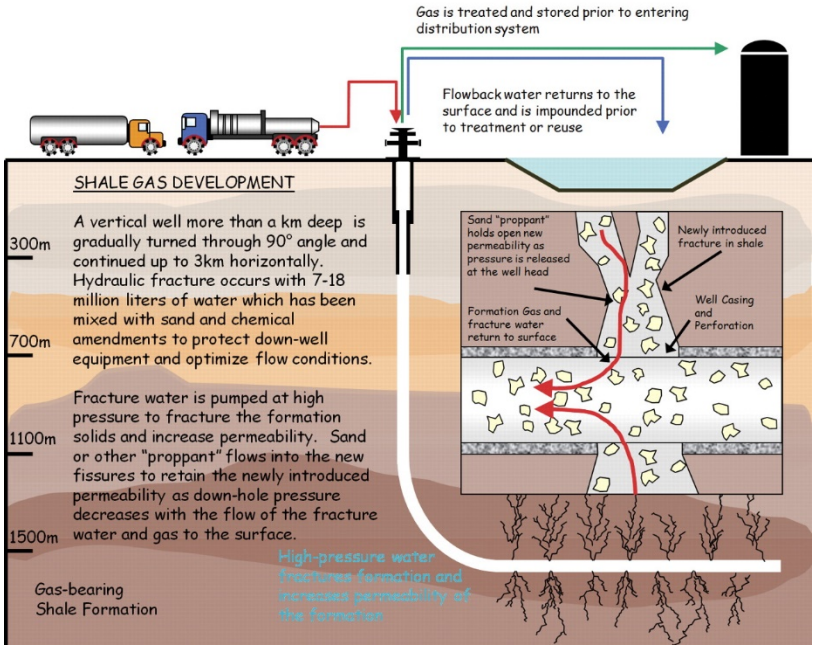

Figure 2. 4Overview of how hydraulic fracturing is used to produce natural gas from shale [76]

Once the fracturing is completed, the injection pressure is reduced and the fluid mixture returns up the well to the ground for a brief period (around10 days), followed by shutting-in the well for a soaking process (approximately a few weeks to months) before hydrocarbon production [3,77]. Sometimes, the well is shut-in without a brief flow back period after fracturing operation. The mixture of the flowback fluid usually consists of fractions of injected fluids, co-extracted formation water, and other substances as a result of various hydro-geochemical processes, as shown in **Figure 2.5** [78,79].

Most field observations found that the flowback fluid only takes up a small fraction of the total fluid injected [4–6,80], and the low recovery of a fracturing fluid could be due to several mechanisms, including retention within fractures due to fracture volume closure during early flowback depletion, and imbibition into the shale matrix [81–83]. Many researchers reported that micro-fractures can be created because of swelling of clays by adsorbing water which take up a significant amount of water [84–86]. Moreover, the spontaneous imbibition of fracturing fluid into shale formations is regarded as the primary factor for fluid loss and its impact on hydrocarbon production is controversial. Many scholars claimed that the spontaneous imbibition process leads to the water block damage, indicating that an increase of water saturation near the induced fractures reduces the relative permeability of shale gas [87–89]. In addition, it was reported that water imbibition can obviously reduce fracture connectivity, resulting from the strength weakness of shale rocks [90]. Moreover, many oilfield cases have confirmed the validity of soaking to increase hydrocarbon production recently [91,92], which is attributed to the counter-current imbibition during a flowback process [93,94]. Therefore, this process has both beneficial and detrimental effects on the production of hydrocarbon in shale formations.

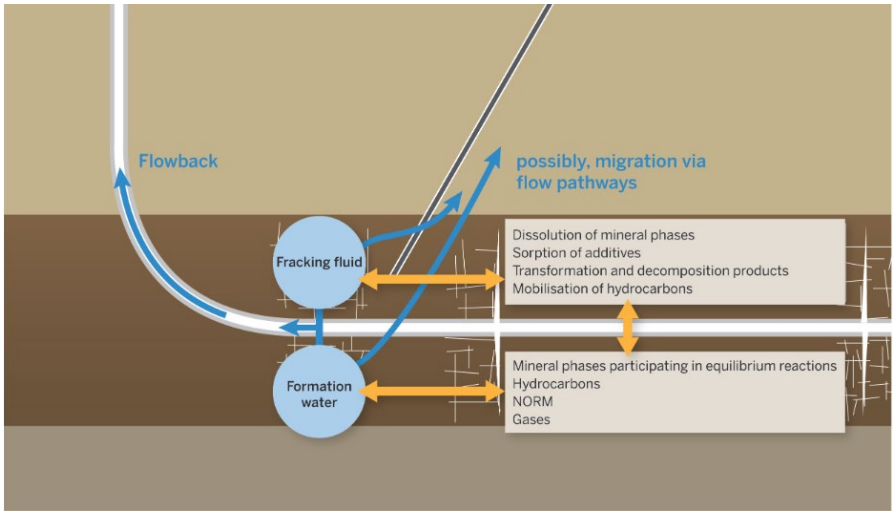

Figure 2. 5 Schematic depiction of flowback formation via mixing of fracking fluids and formation water in connection with hydro-geochemical processes [78]

2.3 Spontaneous imbibition in shale formations

The issue of substantial fracturing fluid loss inside shale did not draw much attention for a decade. In the past few years, many researchers began to investigate various processes by which water imbibes into shale rocks and understand the mechanisms behind each process that contributes to fluid uptake in shale. The main reason for a low recovery of fracturing fluid is the spontaneous imbibition of a fracturing fluid into the shale matrix and capillary pressure is the primary driven force for this process.

There is more and more research focusing on the imbibition behavior of water in nanopores within shale formations [95,96]. Among all mechanisms that lead to spontaneous imbibition in shale formations, a capillary force is the dominant one [37,97,98]. In the field of nanoscale capillarity research, many experimental and simulation works have been conducted to investigate the unique imbibition behavior [99–102]. For example, Cihan et al. stated that the water flow regime in nanopores may transfer from adsorption-diffusion type to a capillary condensation type after a critical relative humidity (RH) [103]. In addition, Stroberg et al. presented a calibrated water model combined with a dissipative particle dynamics thermostat in MD simulations, which successfully predicted surface tension, density, and viscosity of water in a capillary filling problem [104].

To investigate the spontaneous imbibition in shale nanopores, the wettability condition and the nanoconfined condition are the two main factors that need considerations.

2.3.1 Wettability of shale formations

As the wettability of a rock is one of the key factors controlling capillary pressure, numerous experimental research has been focused on the wettability of shale reservoir rocks [105–109]. Typically, the kerogen-rich shales are oil-wet or mixed-wet, and the wettability of shale reservoir rocks are different for various components. Commonly the inorganic minerals are hydrophilic and organic matters are hydrophobic. Observations from most of the experiments on shale rocks from a variety of formations indicated that kerogen-rich shales tend to have a higher affinity for oil than for water. However, some authors [81,110]

reported conflicting results by contact angle measurement. The main reason for these counter-intuitive results lies in the difference between the contact angle under macroscopic and microscopic conditions. The meniscus will be highly deformed at the nanoscale due to the influences of the solid surface, which leads to a different value of the contact angle. Additionally, the role of surface tension becomes less important compared to the line tension at the three-phase contact line under the nanoconfined conditions, which further deviates the microscopic contact angle [111–114]. To avoid this problem, a cylindrical droplet is usually measured in MD simulations to obtain a contact angle that is not affected by the line tension [115].

The imbibition tests have been performed extensively. A schematic showing the general imbibition behavior of oil and water within the same sample of rock is illustrated in **Figure 2.6** [88]. The results obtained by these authors demonstrated that the normalized imbibed mass of the oil phase was higher than that of the water phase at the initial stages, owing to a higher affinity for oil by the shale samples. This implies that the shale rock sample used in these experiments is generally oil-wet. However, the oil imbibition rate reached a plateau sooner than the water phase and the total imbibed volume of oil was less than that of water. This was ascribed to the strong adsorption of water by clay in the shale samples. Kerogen-rich shales tend to have a higher affinity for oil than for water, however, the oil phase does not have an affinity to absorb on clay. Therefore, there also exists hydrophilic minerals in this shale rock sample. The clay minerals can absorb a large amount of water, which could also generate micro-fractures and, as a result, increase sample permeability.

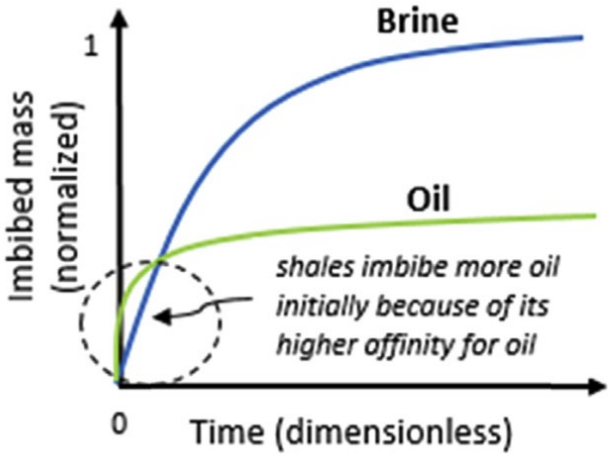

Figure 2. 6 General imbibition behavior of oil and water within the same sample of rock [88]

2.3.2 Capillarity at the nanoscale: The influence of the disjoining pressure

The spontaneous imbibition behavior of fracturing fluid is usually simplified to a capillary filling process which can be modeled by the Lucas-Washburn (L-W) equation. Lucas [116] and Washburn [117] investigated the fluid invasion in the capillaries with negligible gravity and inertia and found a linear relationship between the capillary rise and the square root of time. This relation can be derived based on the classic Hagen-Poiseuille equation [118]. As the wetting phase invades the non-wetting phase inside the pores because of capillary pressure acting on the meniscus of the interface, it has to resist its own viscous force within the wetting fluid. However, when the confinement is down to the nanoscale, the classic L-W which is derived at the macroscale is not applicable. A review by Honschoten et al. summarized unique phenomena for capillarity at the nanoscale [34]. It is stated that under nanoconfinement conditions, the microscopic structure of the contact line and the meniscus will be highly deformed due to the influence of the surface forces, which are associated with the disjoining pressure and the wetting films. It is acknowledged that the capillary meniscus can coexist with the liquid films [119–121]. Water in nanopores will be in the form of film adsorbed on solid surfaces when the relative humidity is low, and its thickness raises as the relative humidity increases until a critical value. Capillary condensation occurs if the relative humidity further increases [121]. Li et al. deemed that capillary

condensation only occurs when water films reach the critical thickness [68,122,123]. After this threshold, water is regarded to not be influenced by a solid surface and is defined as the bulk phase. The calculation of this critical value is usually based on the concept of disjoining pressure proposed by Derjaguin et al. [124]. Disjoining pressure is defined as the pressure difference between water in the thin film and that in bulk liquid, which represents the influence of solid surface forces. It is characterized by the sum of molecular component Π_m, electrical component Π_e, and structural component Π_s. Each term can be calculated as follows [124–126]:

$$\Pi_m(h) = \frac{A_H}{h^3}$$

$$\Pi_e(h) = \frac{\varepsilon\varepsilon_0}{8\pi}\frac{(\zeta_1 - \zeta_2)^2}{h^2}$$

$$\Pi_s(h) = ke^{-h/\lambda} \tag{2.1}$$

where A_H is the Hamaker constant, ε_0 is the permittivity of vacuum and ε_r is the relative permittivity of film. ζ_1 and ζ_2 are the electric potentials of two interfaces between film, respectively, k is the constant of structural force and λ is the characteristic thickness of the hydration layer.

The Critical thickness h^* for the water film is obtained by:

$$\frac{\partial\Pi(h)}{\partial h}_{h=h^*} = 0 \tag{2.2}$$

Furthermore, there are other special phenomena under nanoconfined conditions. For example, the electro-capillarity may occur when a solid surface is charged, as in the case of water absorption by clay minerals. The presence of electric fields induces an extra stress term to be added in the Young-Laplace equation. A typical example is the formation of the Taylor cone, essential in the theory of electrospray.

2.3.3 Other factors

Apart from capillary pressure, other mechanisms may also contribute to liquid imbibition in shale formations, including clay hydration, osmosis effect, creation of microfractures, and evaporation due to gas expansion. These mechanisms were reviewed and discussed by Singh [88].

Clay hydration is an important mechanism for liquid uptake by shale formations, which can also be explained by osmosis. The abundant charged clay minerals can adsorb water molecules through interlayer spaces. Some researchers reported that imbibed volume in some core samples can be greater than the initially measured pore volume, indicating strong adsorption of water by the semi-permeable clay membranes [106,127,128]. The theory of the electrical double layer (EDL) theory is usually used to explain the interactions between the clay membranes and aqueous solutions. The characteristic thickness of the EDL is generally referred to as Debye length (DL), representing the length over which the electrostatic effects persist. Tuning the dynamics of the fluid in the EDL or modifying its structure is expected to affect the whole response of the system and exert a macroscopic impact on the fluid dynamics at scales much larger than the Debye length [35]. Thus the Debye length plays a significant role in nanofluidics and the impact of clay hydration on fluid flow properties cannot be neglected. **Figure 2.7** gives an illustration of the general concept of EDL [88].

Moreover, low pore connectivity, as well as strong heterogeneity in pore types and pore geometries, are other important factors. All these mechanisms lead to a non-linear relationship between imbibition length and the square root of time, which makes the imbibition characteristics more complex than capillary filling.

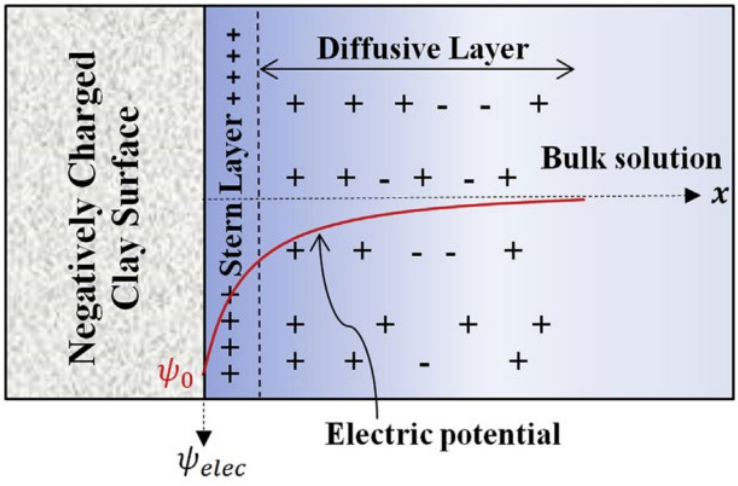

Figure 2. 7 Schematic to depict the charge distribution around the clay surface and to illustrate the general concept of EDL [88]

2.4 Unique flow properties at the nanoscale

The reason why nanofluidics deserves its own terminology is primarily attributed to the considerable progress made over the last two decades in developing nano-fabrication technologies and computational techniques, like MD simulations, which give the possibility of investigating fluid behavior at the nanometer scale. In this subsection, literature is reviewed in terms of experiments, computational work, and theoretical analysis, which focus on unique properties and physical phenomena for water flow at the nanoscale. The slip behavior and the molecular-scale friction force are firstly reviewed, as this is an important research topic and this behavior highly affects the total flow rate. Then, the changed viscosity effect and the dynamic contact angle for nanoconfined water are investigated. Finally, the spreading behavior of the precursor films is reviewed, which may occur in the context of fracturing fluid imbibition in shale.

2.4.1 Friction force and the slip behavior

The dynamics of flow in confined geometries can be thoroughly understood only if the physics of the flow at the fluid-solid interface is accurately described. One of the most important steps towards this understanding lies in the determination of the correct boundary conditions for liquid flow. It is acknowledged that the traditional no-slip boundary condition does not hold for all conditions, as fluid molecules near the solid surface could not bear the infinite stress. Thus, as long as the shear stress at the solid-liquid interface is large enough, the interactions between the solid surface and liquid molecules could be conquered and the slip could occur [129]. Recent experiments and MD simulations have shown that liquid flow at the nanoscale can be many orders of magnitude higher than that predicted from the conventional fluid flow theory with a no-slip boundary condition [130–132]. Therefore the slip behavior is essential for nanofluidics, which highly affects flow properties.

The primary mechanism contributing to slip is believed to arise from a stronger viscous force between liquid molecules compared with that between liquid molecules and solid surfaces. Slip is much more

prevalent when the solid-liquid interactions are weak or the shear rate is high, and thus, wettability and the shear rate are believed to be the most important factors affecting slip. Many works have proved that hydrophobic surfaces tend to induce slip compared with hydrophilic surfaces as the strength of the molecular potential between the fluid and wall molecules is lower [133–136]. Huang et al. obtained a quasi-universal relationship between the slip length and the contact angle [137], which was verified to fit many MD results [134,138,139]. Besides, many researchers found that the slip length increases rapidly with the shear rate [140–145]. However, whether slip is shear-dependent is still controversial, as many experiments agreed with a constant slip length model [146–152].

Moreover, apart from this primary mechanism, there are many other factors, such as surface roughness and possible dissolution of gas [139,153–156], which can give rise to slip behavior. Owing to these factors, wettability may not be the dominant mechanism under some circumstances, as many works have verified that slip behavior can also exist under hydrophilic conditions [151,157–160]. Due to the complexity of the slip behavior, current techniques do not appear to be capable of providing an accurate physical description of boundary slip behavior. This is also responsible for the scattered results of slip length published in current literature. Kannam et al. reviewed the existing literature on water flow in carbon nanotubes and within graphene sheets, and they found that the slip length reported were scattered over 5 orders of magnitude for nanotubes of diameter 0.81-10 nm [161]. Some scholars even found slip lengths exceeding 1000 nm under experimental conditions [132,162,163]. Besides, MD simulation studies showed slip lengths spanning from 1 nm to 1000 nm for the tube diameter range of 0.81-7 nm. It is well known that the slip length will be higher for a curvature surface, and it increases sharply when the radius of curvature is down to several nanometers. Under the same external force field, the slip length will be the smallest for a flat geometry [33]. For a flat graphene, the slip lengths span the range of 1-100 nm in the literature [29,161]. For example, experimental measurements conducted by Qin et al. obtained a slip length of around 10 nm [164]. Additionally, slip lengths measured by MD simulations were reported from

35-80 nm [165–170]. For instance, Wagemann et al. found a constant slip length around 50 nm before a critical shear rate for water flow within graphene nanochannels with separations of 2-2.8 nm [28]. All these scattered results reflected the complexity of the slip behavior, and thus there is a strong need for both theoretical work and simulations in this area so as to provide more understanding for the experimental results [171].

In addition, the mechanisms of friction are closely related to the slip behavior at the liquid-solid interface [172–176], and a precise prediction of the slip boundary condition is crucial for a thorough description of fluid dynamics at the nanoscale [16,132,162,177–182]. Therefore, understanding mechanisms of liquid-solid friction process and relating friction to the slip behavior play a key role in hydrodynamics of a nano-confined water flow. Ma et al. found that the data from MD simulation fitted very well using a general inverse hyperbolic sine relation between shear stress and slip velocity [145,183]. Besides, the friction coefficient is usually computed to relate slip length and the magnitude of friction force [184–187]. This parameter can be expressed in terms of equilibrium properties in the form of the Green-Kubo relation [183,188]. However, this coefficient is a macroscale parameter, and there is limited work focusing on molecular-scale friction due to the complexity of the liquids at the nanoscale.

Commonly, the mechanisms of liquid-solid friction are distinguished from those of solid-solid friction and friction within a liquid, even when the system is down to nanoscale [149,189–192]. For solid-solid friction at the nanoscale, the dominant mechanisms are adhesion hysteresis and deformation of asperities [193–199]. For friction within a fluid, the viscous force which represents the interaction strength between fluid molecules is the main factor contributing to friction. As for liquid-solid friction, both the interactions between the solid substrate and liquid, as well as interactions between fluid molecules have significant impacts on the friction at a liquid-solid interface [200,201]. Among the investigations of liquid-solid friction at the nanoscale, most researches were conducted in the context of lubrication processes [202,203].

Commonly, these liquid molecules have long and complicated structures, which highly affect the magnitude of friction [204,205].

However, many studies have prompted the uniformity between water-solid friction and solid-solid friction, regarding both complex fluids and simple fluids like water. For example, Michael et al. compared the solid-solid friction and the advancement of a liquid drop's triple line through a solid substrate and found that both of them were closely related to adhesion hysteresis resulting from chemical heterogeneity and surface roughness [206]. Moreover, Lichter et al. modified the Frenkel-Kontorova model which was usually used to describe dislocation motion in solids and applied the modified equation (vdFK model) to successfully model liquid dynamics at a liquid-solid interface [207]. Furthermore, Bocquet and Barrat proposed and validated a systematic derivation of the friction coefficient by considering the structure factor of the fluid. The incorporated term measures commensurability of the fluid with the underlying solid structure, in full analogy with solid-solid friction [50,208]. Thus, solid-solid friction and liquid-solid friction should have similar mechanisms at the molecular scale, which deserves further investigation.

Moreover, the effect of surface friction on liquid imbibition was researched in the context of dynamic contact angle and many scholars attempted to propose theoretical foundations for friction coefficient that account for the effect of surface roughness and confinement [209–213]. Kelly et al. showed that the solid-liquid interactions at the nanoscale lead to increased viscosity compared to the bulk phase [214]. They proposed a simple expression for viscosity accounting for surface friction in the imbibition dynamics as follows:

$$\mu_{eff} = \mu_{bulk}\{1 + \frac{1}{\rho_{bulk}\lambda^3}\exp\left[\frac{\gamma(1+cos\theta_e)\lambda^2}{k_BT}\right]\} \tag{2.3}$$

where μ_{bulk} is the bulk fluid viscosity, γ is the surface tension between the wetting and non-wetting fluids, θ_e is the contact angle at equilibrium condition, λ is the average length of the molecular displacement (of the order of the distance between the adsorption sites on the solid surface), k_B is the Boltzmann's constant,

and T is the temperature. Another approach to consider the effect of the surface force is to use the tangential momentum transferred by the liquid particles colliding with the wall [210]:

$$F_f = \frac{N_{coll} m \Delta u_w}{\Delta t} \tag{2.4}$$

where F_f is the force exerted by the surface friction on the liquid motion, N_{coll} is the number of particle collisions with the solid wall in time Δt, m is the mass of the particles colliding with the wall, and Δu_w is the mean velocity change for the particles colliding with the wall.

2.4.2 The increased viscosity effect for fracturing fluid imbibition in shale

For a spontaneous imbibition process under a nanoconfined condition, the most important effect induced by the solid surface is that the effective viscosity of water is different from the bulk phase value. It was found that the effective viscosity under a hydrophilic condition is usually higher than that of the bulk phase, while it is lower under a hydrophobic condition [33,215–217]. For a spontaneous imbibition process, water will imbibe into hydrophilic pores, and the effective viscosity will be higher than that of the bulk phase. The increase of the viscosity results from the stronger interactions between water molecules in the near-surface region and the solid surface, compared to viscous interactions among water molecules [218]. In the direction normal to water flow, the strong interactions make it easier for water molecules to be attached to the solid surface, and thus the flow resistance becomes higher, leading to the increased viscosity effect [34]. To predict the water imbibition behavior in shale formations precisely, the increased viscosity effect must be considered. Many experiments verified that the L-W model can still be applied in a capillary filling problem at the nanoscale, as long as the viscosity is correctly calibrated [34,219–222]. However, there are two important assumptions for the validation of the L-W model. The first one is that the radius of a nano capillary or the width of a nanochannel is large enough to ensure the existence of a bulk phase in the middle of the flow region. The L-W model is a continuum model that is derived from the Hagen-Poiseuille equation, and it cannot be used under a sub-continuum condition. As mentioned in Chapter 1, the threshold for the validity of the continuum hydrodynamics is approximately

1.66 nm. Therefore, the L-W model can only be used for nanopores with a diameter of larger than 1.66 nm. The second one is that the L-W model assumes a force balance between capillary forces driving the flow and viscous drag. This is only observable in the initial states of an imbibition process, and eventually, gravity comes into play, ceasing the imbibition process. Therefore, this model can only be used in the early time of the imbibition process.

The key to model the water flow behavior under nanoconfined conditions is to predict the effective viscosity precisely. Some theoretical research on this issue has been performed. For example, Tomas and McGaughey divided the flow area into the bulk phase and interaction region and used a constant viscosity as well as a constant thickness of the interaction region to calculate the total flow rate [33]. A similar treatment was adopted by Vo et al. to predict the effective viscosity for nanoconfined water [223]. However, the assumption that the viscosity within the interaction region is a constant is not strictly valid, as this value should be a function of the distance to the solid surface. Moreover, some approaches were proposed with the fitting methods of the experimental data, and there were parameters with unclear physical meanings [224,225]. Therefore, a simple theoretical model that captures physics under nanoconfined conditions is still lacking.

2.4.3 The dynamic contact angle

The most common model to describe a dynamic imbibition process, the L-W model, uses a constant contact angle, which is the equilibrium one under Young's condition. However, during a dynamic imbibition process, a moving three-phase contact line (TPCL) experiences surface roughness and chemical heterogeneities, leading to a dynamic contact angle [226]. It was observed from many experiments that a dynamic contact angle is dependent on the meniscus velocity [227,228]. Cherry and Holmes proposed a theoretical model for the dynamic contact angle, where the wetting process was considered as an activated rate process. This theory was based on the Molecular Kinetic Theory proposed by Eyring, which was applied to describing viscous flow mechanisms [229,230]. It was assumed that a TPCL moved along

successive equilibrium positions across intervening activation energy barriers during a liquid spreading process [231]. Later, Blake and Yarnold improved this theory and claimed that the driving force for the motion of a TPCL arose from the unbalanced surface tension. The adsorption equilibrium was disturbed during the motion of the TPCL, leading to a changed curvature of a meniscus [232–234]. It was verified that the Molecular Kinetic Theory is sufficient to describe a capillary filling process when hydrodynamic regimes play a dominant role after an inertia effect at the initial stage [235,236].

2.4.4 Spreading of the precursor films

Recently, a research topic that draws increasingly wide attention is the fluid imbibition behavior in nanopores with the existence of precursor films. The precursor film propagation is a prevalent phenomenon during a wetting process, and the dynamic imbibition behavior with the precursor films has extensive applications in nanotechnology and chemical engineering [237]. For example, the performance of the external wetting of porous solids plays a key role in widely employed trickle bed reactors, which is associated with a lubrication approximation for thin film flow on an external surface [238]. The thin films propagating ahead of the main meniscus may manage to hide the chemical and geometrical details of the nano-channel walls, thereby exerting a major influence on the efficiency of nano-channel–coating strategies [139,239]. Furthermore, for fracturing water imbibition in shale formations, the non-negligible precursor films may also occur. Therefore, the physics of the precursor films need to be considered when modeling the spontaneous imbibition process of water in shale.

A wetting process with the existence of precursor films was first investigated in the context of droplet spreading on a substrate. A special case that a droplet spreads from an initial non-equilibrium configuration with $S_0>0$ towards its equilibrium shape where $S=0$ has been the subject of extensive experimental and theoretical investigations, where S_0 is an initial spreading coefficient, and S is the spreading coefficient under the equilibrium state. The pioneering work by Hardy reported the observation of a precursor film ahead of the edge of a macroscopic drop [240], and numerous experiments verified

this observation later [241–244]. A consensus in this area has been reached that precursor films are omnipresent in a liquid-solid-vapor wetting system, even when liquid droplets only partially wet a solid surface. These films spread ahead of their meniscus as lubricants for the macroscopic part of drops, resulting from the competition between the gain in entropy and the balance of liquid-solid interactions and viscous interactions within fluids [245].

It is well acknowledged that the water dynamics in the bulk phase are different from that in a thin film attached to a solid surface. Philip proposed a unitary approach to capillary condensation and adsorption in porous media [246]. A liquid-vapor interface is considered as a surface of constant partial specific Gibbs free energy. The bulk phase water is controlled by a capillary component while the water in the film is dominated by an adsorptive component. Moreover, the driving force for a capillary filling process is composed of two components, the liquid-vapor interfacial tension and the spreading power of a solid surface. This force is given in the following equation:

$$f_Y = S_0 + \sigma_{lg}(1 - \cos\theta_t) \tag{2.5}$$

where f_Y is the Young capillary force per unit length of a contact line, σ_{lg} is the surface tension of a liquid-vapor interface, and θ_t is the dynamic contact angle. S_0 is given by

$$S_0 = \sigma_{sg} - \sigma_{lg} - \sigma_{sl} \tag{2.6}$$

where σ_{sg} is the surface tension of a dry solid substrate in contact with gas and σ_{sl} is the solid-liquid interfacial tension. The driving force due to the spreading power of the solid surface cannot be neglected at the nanoscale, which can be comparable to that arising from the liquid-vapor interfacial tension.

For an imbibition process under strongly hydrophilic conditions, the initial spreading coefficient is usually positive. Under such conditions, S_0 indicates the driving force for film spreading, and the other term represents the driving force for capillary filling. Hervet and de Gennes found that for a complete wetting case where S_0 is non-negative, the entire spreading power S_0 is dissipated in a film [247,248]. This remarkable finding resolved the paradox that the spreading of a macroscopic meniscus is independent of

S_0 in a complete wetting case [249,250]. Therefore, the bulk water will flow above films, which act as a pre-wetted substrate for the sliding of the bulk water.

The motion of precursor films is fast compared with the bulk phase water during a capillary filling process. It was verified that the primary mechanism of film propagation is surface diffusion of molecules from the edge of a meniscus, and a precursor film itself is solid-like [241,251,252]. This is consistent with the observation that the viscosity of water close to a solid surface is increased dramatically, and the mobility of water is highly reduced. Moreover, the structure of water molecules near a solid surface can be changed by surface forces. Epitaxial layers in a fluid that mimic the solid structure near a solid surface were observed by many simulations and experiments [134,216,253,254]. A consensus has been reached that the fluid structure close to the solid surface is detrimental to the slip behavior under the strongly hydrophilic conditions, as a solid wall can drag fluid molecules more efficiently when the epitaxial layers form [217]. Furthermore, water molecules tend to be layered near a solid surface, leading to the multi-layer sticking phenomenon [215]. This arises from the changed structure of water molecules near the solid surface. Thus, the density of the water layers close to the solid surface is normally higher than the bulk phase value. Numerous MD simulations showed that a density peak usually occurs for the first water layer near a solid surface, and the bulk phase density can be obtained beyond two water layers [47,255,256]. Additionally, it is found that the ratio of the peak density to the bulk density is related to a contact angle, indicating that water layering is more prevalent under strongly hydrophilic conditions [257]. **Figure 2.8** illustrates the water layering phenomenon for the first two water layers close to a solid surface, which arises from the strong adsorptive forces induced by the solid surface. The water molecules whose motion is highly restricted in the first two layers have an ordered molecular arrangement, while, in the bulk region, the water molecules can move randomly due to thermal motion. Besides, there is a void region between the solid surface and the first layer of water, resulting from strong repulsion at short ranges.

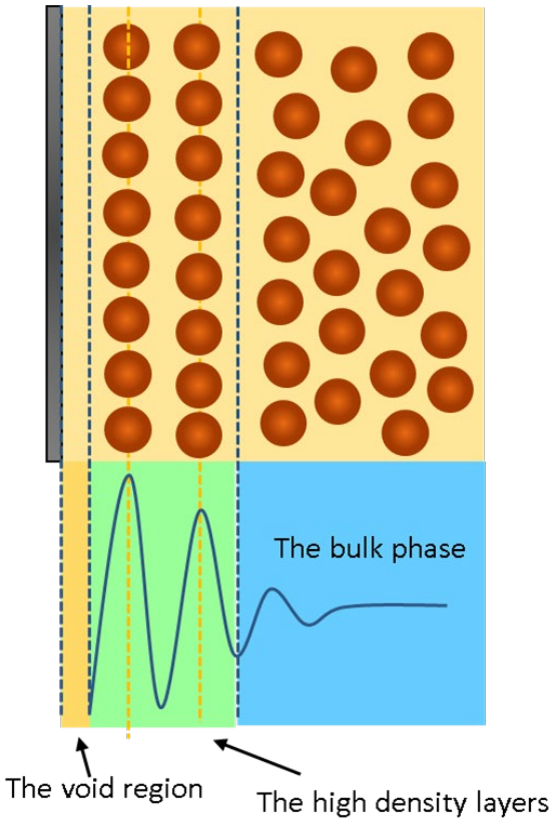

Figure 2. 8 The density layering phenomenon for water near a solid surface in half of a nano-channel

the pioneering work conducted by Hervet, de Gennes, and Joanny provided a thorough description of the spreading of precursor films which includes a contribution of long-ranged forces [247,258,259]. Theoretical analysis showed that when a meniscus advances slowly and a film reaches a stationary shape very rapidly at time scales that are much shorter than the scales at which the velocity of the meniscus varies, the spreading of the precursor film arises from the drift of the meniscus. In this case, the length of the precursor film increases very slowly, which can be regarded as a constant. The length of the precursor film is calculated by [260]:

$$L_f = \sqrt{\frac{A_H S}{6\pi {\mu_b}^2 V^2}} \tag{2.7}$$

where L_f is the length of the precursor film, A_H is the Hamaker constant, μ_b is the bulk phase viscosity, V is the velocity of the meniscus, and S is the spreading coefficient, which can be computed by [245]:

$$S = \int_h^\infty \Pi(h)dh \tag{2.8}$$

where Π(h) is the disjoining pressure and h is the film thickness. The disjoining pressure can be calculated by [124]:

$$\Pi(h) = \frac{A_{\mathrm{H}}}{h^3} + \frac{\varepsilon_r \varepsilon_0}{8\pi}\frac{\Delta\zeta^2}{h^2} + ke^{-\kappa h} \tag{2.9}$$

where ε_0 is the permittivity of vacuum, ε_r is the relative permittivity of a film, $\Delta\zeta$ is the difference of the electric potentials of two interfaces separating the film, k is the constant of the structural force, and κ is the reciprocal of the Debye length.

Moreover, it was found that at a long-timescale when a film reaches microscale, the motion of the precursor film is because of the gradient of the disjoining pressure along the film, and the film increases diffusively. This is because the supplement of water from its meniscus is negligible compared with the film length, and in this case, the film length can be computed by:

$$L_f = \sqrt{D_f t} \tag{2.10}$$

where D_f is a self-diffusion coefficient, which is verified to be comparable to an Einstein-Stokes self-diffusion coefficient [245]. Therefore, the film length is proportional to the square root of time [259,260]. Although the film thickness under various conditions ranges from molecular size to over 1000 nm, this dependence holds very generally for self-diffusive films. Only diffusivity depends on the particular feature of a liquid-solid system. Many factors, including the molecular weight, the bulk phase viscosity, the surface energy, and the relative humidity, were found to affect the diffusivity of a precursor film [261–264].

2.5 Fundamental theories of molecular interactions and Molecular kinetic theory

2.5.1 Molecular interactions

Understanding the fundamental theories of molecular interactions is the first step towards the establishment of a theoretical approach modeling nanoconfined water flow. These basic theories are also adopted in MD simulations, which have been applied in all parts of science and engineering backgrounds

due to the development of high-performance computing during the last few decades. It provides a straightforward method for analyzing a system in the detail such as interactions between atoms, topological structures of molecules, and thermodynamic properties. The various kinds of interactions between molecules are introduced below. Moreover, the governing equations and the Integration of equations of motion used in MD simulations are briefly introduced.

The interactions between molecules can be classified into intramolecular interactions and intermolecular interactions. The former includes bond stretching, angle bending, torsion around bond while the latter consists of van der Waals (vdW) and electrostatic interactions.

The bonded interaction has the same physical meaning as the intramolecular interaction which can be written as:

$$U_{bonded} = U_{bond} + U_{angle} + U_{diherals} + U_{impropers} \tag{2.11}$$

where U_{bond} refers to the potential energy of bond stretching. U_{angle} implies the potential energy required to bend the angle formed by three atoms, which varies with time due to vibration. The dihedral and improper terms represent the interactions between four bodies which are common for molecules with long chains.

The non-bonded interactions can be expressed as:

$$U_{non-bonded} = U_{electrostatic} + U_{vdw} \tag{2.12}$$

The Lennard-Jones (L-J) 12-6 potential is the most common model to describe the van der Waals force:

$$E(r_{ij}) = \begin{cases} 4\varepsilon_{ij}\left[\left(\frac{\sigma_{ij}}{r_{ij}}\right)^{12} - \left(\frac{\sigma_{ij}}{r_{ij}}\right)^{6}\right] & r_{ij} \le r_{cutoff} \\ 0 & r_{ij} > r_{cutoff} \end{cases} \tag{2.13}$$

where r_{ij} represents the intersite distance between atoms i and j, ε_{ij} is the well depth of the Lennard-Jones (L-J) potential, σ_{ij} is the L-J size parameter, and r_{cutoff} is a cut-off radius, beyond which the interaction is negligible. Cross interaction parameters for unlike pairs are determined by the Lorentz-Berthelot combining rule:

$$\sigma_{ij} = \frac{1}{2}\left(\sigma_{ii} + \sigma_{jj}\right) \tag{2.14}$$

$$\varepsilon_{ij} = \sqrt{\varepsilon_{ii}\varepsilon_{jj}} \tag{2.15}$$

The electrostatic interactions are typically long-range forces. The partial charges of each atom are generally obtained according to electronegativity differences and quantum mechanics, which can replicate the dipole moment of molecules.

Particles' evolution with time the MD simulation system applies Newton's equation of motion for classical mechanics. The force exerting on each atom is described as the negative gradient of the potential energy U(r) between two atoms with a distance r:

$$F = -\nabla U(r) \tag{2.16}$$

The force exerting on each particle in the system is firstly calculated according to its position relative to other particles, and then the position of each particle at the time of $t+\delta t$ is updated by integrating the equations of motions. Therefore, the time evolution of the system, the momentum, and the position of each atom at each time step can all be obtained. The Verlet algorithm and the Leapfrog algorithm are commonly used for this calculation.

2.5.2 Molecular kinetic theory

A classic theory of the transport properties of liquids was developed by Eyring et al. [229,230,265], which gave a quantitative estimation of viscosity and diffusion based on the statistical mechanical theory of reaction rates. This theory is revisited to bridge the gap between behavior water at the molecular scale and macroscopic hydrodynamics.

According to this theory, liquid molecules are largely confined within energy barriers formed by their neighbors because of the close packing. The motion of liquid molecules is regarded as the molecule overcoming energy barriers and hopping to the next low energy site. When fluid molecules are under external forces, shear stress, for instance, the energy barriers along the direction of the external force will be changed, as shown in **Figure 2.9**. The rate of hop under external force is given by:

$$v = v_+ - v_- = \frac{kT}{h_P}\exp\left(\frac{-\Delta G_0}{kT}\right)\left[\exp\left(\frac{-F_a\delta}{kT}\right) - \exp\left(\frac{F_a\delta}{kT}\right)\right] \quad (2.17)$$

where v is the hopping rate, v_+ is the forward hopping rate in the direction of the external force, and v_- is the backward hopping rate. T is temperature, k is Boltzmann constant and h_P is Planck constant. ΔG_0 is the energy barrier, F_a is the external force acting on the molecule and δ is the length for each hopping event. F_a multiplied by δ is the work done by the external force, which can also be calculated by:

$$W = \frac{\tau V_m}{2} \quad (2.18)$$

where τ is shear stress and V_m is the molecular volume. The velocity profile is considered to be linear over a very small distance between two water layers, and thus:

$$-\frac{dv_x}{dy} = \frac{a}{\delta}(v_+ - v_-) = \frac{2akT}{\delta h}\exp\left(\frac{-\Delta G_0}{kT}\right)\sinh\left(\frac{-F_a\delta}{kT}\right) \quad (2.19)$$

Combined equations (2.17)-(2.19), the viscosity can be computed by:

$$\mu = \frac{\tau}{-\frac{dv_x}{dy}} = \frac{F_a\delta^2 h}{4akTV_m}\exp\left(\frac{\Delta G_0}{kT}\right)\operatorname{csch}\left(\frac{-F_a\delta}{kT}\right) \quad (2.20)$$

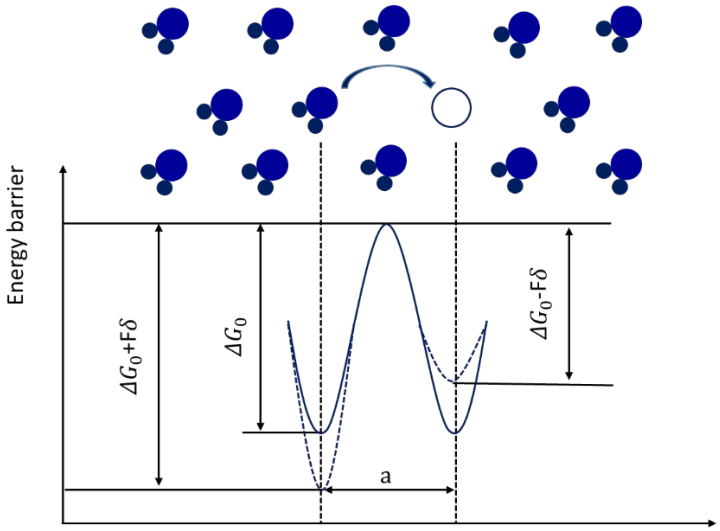

Figure 2. 9 Illustration of the hopping event for a water molecule

Chapter 3 Molecular-scale friction and the slip behavior

Understanding molecular-scale friction at a liquid-solid interface in a nanofluidic system is essential, as friction affects slip behavior and flow properties at the nanoscale. In this Chapter, the molecular-scale friction at a water-graphene interface is computed, combined with theoretical analysis and MD simulation. A solid-solid friction model is modified, regarding a new method to calculate the work done by the substrate. The reliability of the computations is validated by MD results. It is manifested that liquid-solid friction, solid-solid friction, and viscous friction within liquids have similar mechanisms, in terms of energy barriers. Moreover, the relationship between the slip behavior and friction process is analyzed, and a theoretical foundation between the slip velocity and the friction force is obtained based on a classic molecular kinetic theory. This foundation indicates a hyperbolic-like relation between the friction force and the slip velocity for a single water molecule, which is almost linear under realistic experimental conditions. This foundation provides a new way to determine the boundary condition for water flow between graphene sheets.

3.1 Computation of the molecular-scale friction force

In this section, we modify a solid-solid friction model proposed by Zhong and Tomanek [266], to verify its application to model water flow between parallel solid sheets. Graphene is chosen as the solid substrates due to its simple structure. The main difference between liquid-solid friction and solid-solid friction is that the work done to liquid molecules by the substrate is not the vertical distance multiplied by the external normal force. This is due to that the normal force acting on fluid molecules is not a fixed external load as in the case of solid-solid friction. To take this difference into account, the trajectories of water molecules within the first density layer are analyzed, and an approach to calculate the work done by the graphene substrate is proposed based on the trajectories and total L-J curves.

3.1.1 A model for solid-solid friction process

Zhong and Tomanek quantified the atomic-scale friction associated with a layer of Palladium atoms moving across a graphite substrate by the first-principles theory, which is shown in **Figure 3.1** [266]. As Palladium atoms experience periodic potential energies along their trajectories, the friction is induced owing to the variance of the total potential energy ΔE along a trajectory. This energy variance results from the work against an external load applied to an adsorbate, which is partly compensated by the adsorption energy difference at different sites. The total potential energy variance ΔE is calculated by:

$$\Delta E = f_{\mathrm{N}} \Delta z - \Delta E_{\mathrm{ad}} \tag{3.1}$$

where f_{N} is the external normal load, which is balanced by the repulsive force induced by the substrate against it. Δz is the vertical distance, and ΔE_{ad} is the adsorption energy difference at different sites. As a result of variations of E, there is a position-dependent force f_{x} along the x direction, defined as the direction of atoms' movement. This force is given by:

$$f_{\mathrm{x}} = \partial E / \partial x \tag{3.2}$$

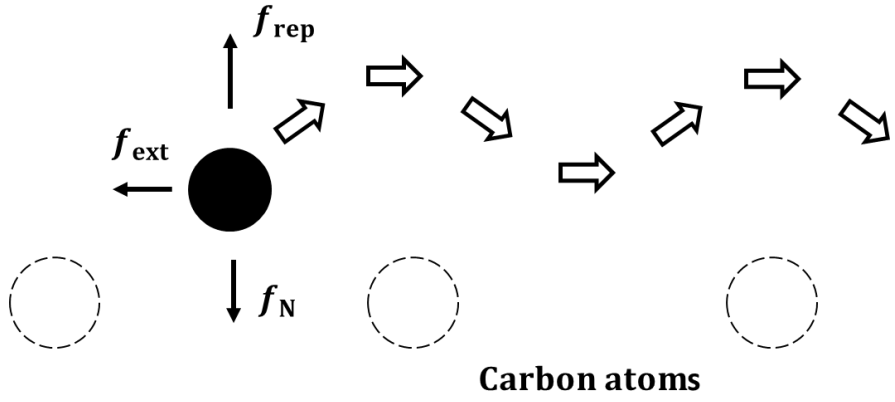

Figure 3. 1 A schematic of a palladium atom sliding on a graphene substrate

According to Sacco's theory, a potential energy increase will be transferred into friction loss, and the energy dissipated by friction ΔE_{f} equals the maximum potential energy variance ΔE_{max} [267]. Moreover, as ΔE_{f} equals the work done by a friction force f_{f}, it is obvious that f_{x} equals f_{f}. Since friction is a conservative process, the friction force should be zero when the potential energy is decreased, otherwise,

a decrease of E along x generates a negative value of friction force and offsets the friction force during the increased stage of the total potential energy, which is unrealistic. Thus, f_f equals f_x when E increases and equals zero when E decreases. The potential energy E and the friction force f_f are plotted as a function of x, as shown in **Figure 3.2** (a) and (b), respectively.

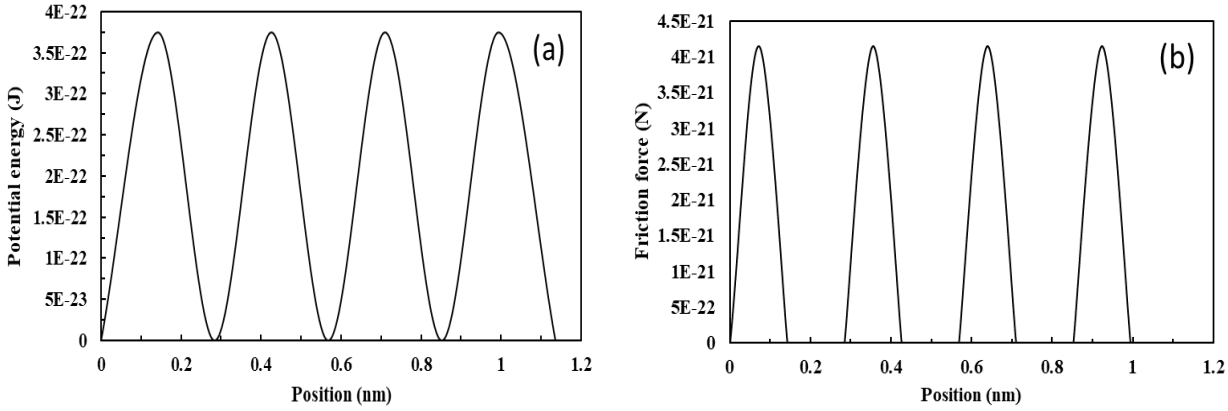

Figure 3. 2 (a) Potential energy variance; (b) Friction force variance

For a sliding process, the friction force should be obtained as a weighted average over f_x from the energy dissipated in the friction along the flow direction. It is illustrated in **Figure 3.2** that for a period of a molecule's movement, the work done by friction equals the maximum potential energy variance ΔE_{max} because f_x is the differential of potential energy with the horizontal position x. Therefore the gliding friction force is computed as follows:

$$f_f = \Delta E_{max}/\Delta x \tag{3.3}$$

where Δx is the distance of one period of the movement.

3.1.2 Molecular-scale friction at the water-graphene interface

An accurate calculation of ΔE_{max} for a water-graphene friction process is important. Carbon atoms in graphene form a structure shape of a regular hexagon, with one carbon atom on each vertex. The central position of the hexagon is defined as H, and the position in the middle of two neighboring carbon atoms is defined as B. The adsorption energy E_{ad} for a single oxygen atom as a function of the vertical position z above these two positions can be calculated by a pairwise sum of L-J interactions with carbon atoms

within a cut-off range, which are illustrated in **Figure 3.3**. It is obvious that the liquid molecules preferentially occupy the sites between solid molecules with the lowest energies, due to stronger adsorption [268,269]. The adsorption energy indicates the van der Waals interactions between the carbon atoms and a water molecule. When the water molecule moves from site H to site B, the adsorption energy is decreased, which will partly offset the positive work done by the repulsive force applied to the water molecule, resulting in the total potential energy variance ΔE between the two sites. As a result, the water molecules within the slip plane will flow above a substrate with periodic energy, and the trajectories of water will be waved due to the influence of the energy substrate, as shown in **Figure 3.4**.

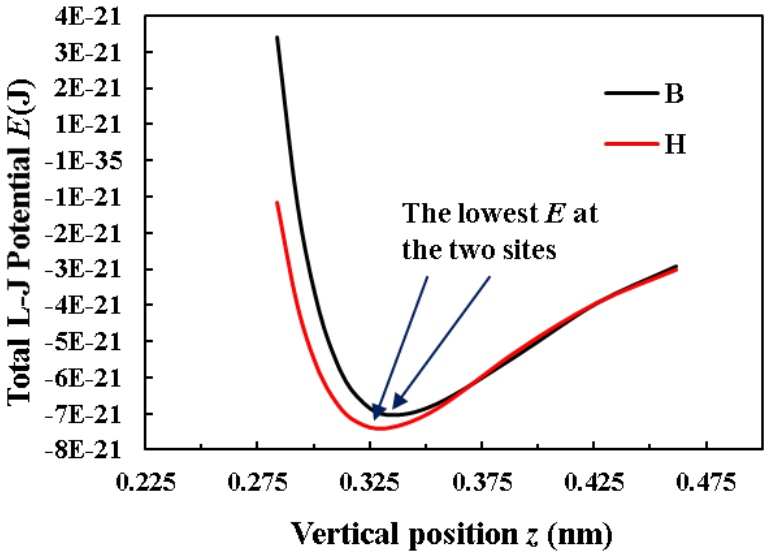

Figure 3. 3 The total potential energy *E* as a function of *z* above two sites

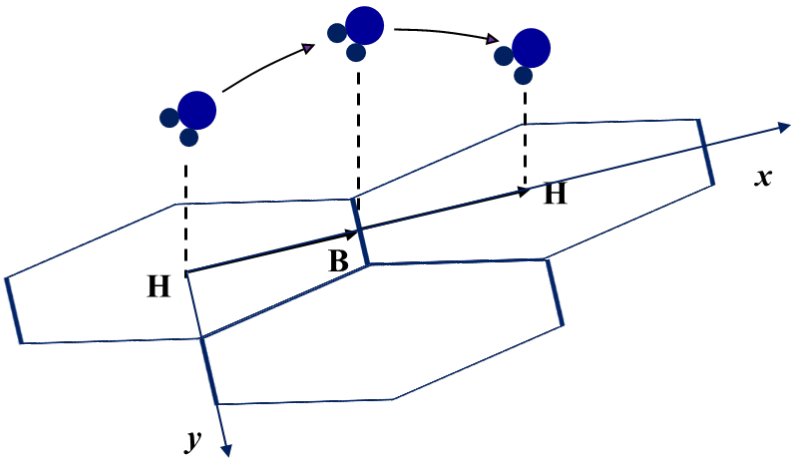

Figure 3. 4 The schematic of the trajectory for a single water molecule above a graphene substrate

To compute the friction force on a single water molecule by using the solid-solid friction model, the normal load exerting on the molecule should be considered. As there is force balance in the z direction, two opposite forces, equal in magnitude, are acting on the water molecule. These two forces are denoted as f_{ext}, and f_{rep}, respectively. f_{ext} represents a force pointing downward to graphene, which has a similar physical meaning with the external normal load in the solid-solid friction. f_{rep} is a force pointing upward which is against f_{ext}. These two forces arise from all interactions acting on a single water molecule within a cut-off range. It is known that a normal force pointing downward will push the molecule towards the graphene until the repulsive force induced by graphene balances it. Thus, f_{rep} is the repulsive force induced by graphene, which equals the differential of the total L-J curve because the repulsive force is due to that the water graphene interaction enters the repulsive region on the total L-J curve. All other interactions, including interactions with other water molecules, dipoles motion, water molecule orientation, and interactions between hydrogen atoms and the graphene, are incorporated in f_{ext}.

To consider these interactions as well as compute f_{ext} and f_{rep} decently, MD simulation is used to obtain the pressure tensors. The average normal pressure tensors exerting on water molecules in the slip plane are determined by using the virial theorem. Here the slip plane represents the first peak density layer in the density profile, which is the outermost water layer close to the interface region. The equation adopted in MD simulation is given by:

$$P_{IJ} = \frac{\sum_k^N m_k v_{kI} v_{kJ}}{V'} + \frac{\sum_k^{N'} r_{kI} f_{kJ}}{V'} \tag{3.4}$$

where P is the pressure tensor, I and J stand for the directions in a Cartesian coordinate, m is the mass of the atom, v is the velocity, and V' is the system volume. N is the number of atoms in the system, N' includes all atoms in the system and periodic image atoms outside the central box. r and f denote position and force, respectively. The calculation for the pressure tensors involves a kinetic term and a virial term, and the latter one includes the sum of all pair-wise interactions and bonded interactions, which considers

all kinds of interactions mentioned above. The normal pressure tensor P_{zz} is used among all pressure tensors, which represents a force and is different from the general physical concept to describe the isotropic pressure in the bulk phase. P_{zz} can be easily transferred into f_{ext} and f_{rep}. When f_{ext} increases, the water molecules in the slip plane will be pushed closer to the solid substrate, leading to a smaller void space within the liquid-solid interface and a higher friction force. A schematic illustrating this influence is shown in **Figure 3.5**.

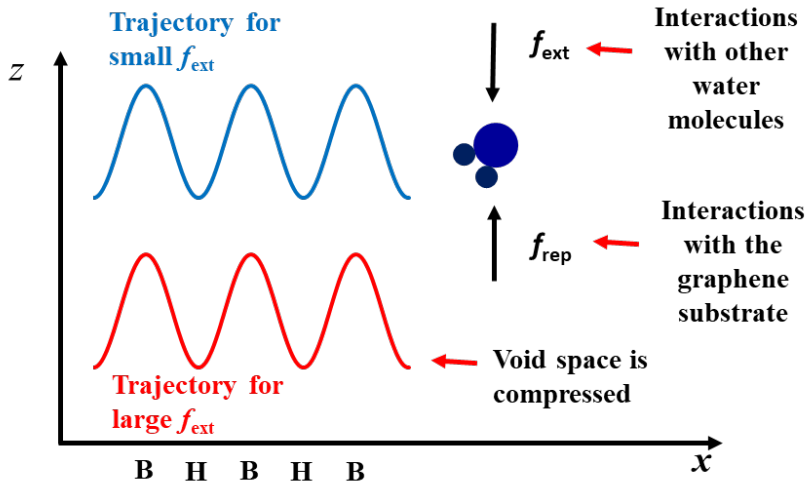

Figure 3. 5 The schematic of the trajectories for a single water molecule under different f_{ext}

As the repulsive force f_{rep} is the differential of the L-J potential with the vertical position z, a tangent line that represents this force can be drawn on the total L-J curves. The coordinates on the horizontal axis corresponding to the points of tangency are the equilibrium vertical positions above the two sites, denoted as Z_H and Z_B, respectively. Those on the vertical axis are the total potential energies for water at the two sites, denoted as E_H and E_B, respectively. These energies and positions are shown in **Figure 3.6** (a). The friction force on a single water molecule can be computed based on E and z for the two sites, using the solid-solid friction model introduced before.

However, the traditional method in the solid-solid friction model to calculate the work done by graphene cannot be used in the liquid-solid friction. For solid-solid friction, the external normal load f_N is usually fixed during the motion of the solid particles, and thus the work done by the graphene is f_N multiplied by

the distance Δz. For a liquid-solid friction process, there is no actual external load acting on the water molecule, and f_{ext}, in this case, is not a fixed load, but rather a statistical concept, representing an average of all interactions acting on the water molecule.

Thus we propose a method to calculate the work done by graphene based on the total L-J curves. The position above site B whose distance to graphene equals Z_H is defined as Z_M, and the potential energy at this location is termed E_M. This potential energy can be found on the total L-J curve for site B. When moving a molecule horizontally from Z_H to Z_M, the work done in the vertical direction is zero, since the repulsive force is in the normal direction, and does no work in the horizontal direction. Thus the total work done when taking a molecule from Z_H to Z_B equals that done when moving the molecule from Z_M to Z_B. This work equals E_M - E_B because the repulsive force above site B is the differential of the L-J potential function above site B. According to the solid-solid friction model as introduced before, this work is partly compensated by the adsorption energy difference ΔE_{ad}, which equals E_B - E_H, and thus ΔE_{max} and the friction force can be calculated as follows:

$$\Delta E_{\max} = (E_M - E_B) - (E_B - E_H) \tag{3.5}$$

$$f_f = \Delta E_{\max}/\Delta x = (E_H + E_M - 2E_B)/\Delta x \tag{3.6}$$

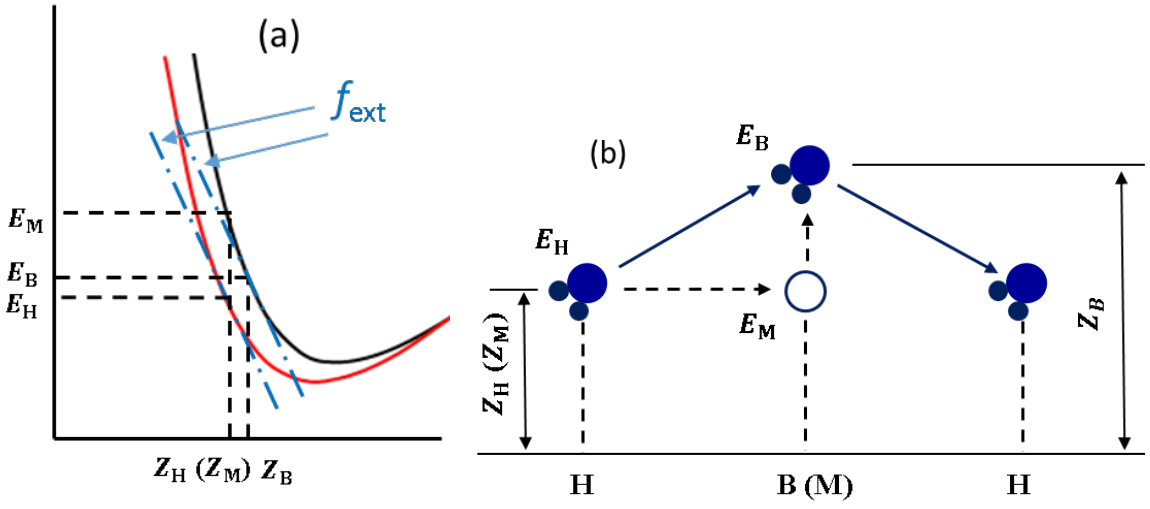

Figure 3. 6 (a) Determination of potentials and equilibrium vertical positions; (b) Parameters used in the calculation of the friction force

3.1.3 MD simulation

The MD simulation is used for the computation of the friction force. The planar Poiseuille flow geometry of water between two parallel graphene sheets driven by an applied force is analyzed. We use Non-equilibrium MD simulation by the Large-scale Atomic/Molecular Massively Parallel Simulator (LAMMPS) package [270], and visualization is realized by using the Open Visualization Tool (OVITO) software [271]. A single graphene layer is used for each wall, and each carbon atom is tethered to its lattice site by a linear spring. Periodical boundary conditions are applied in the *x* and *y* directions in the simulation cell. The dimensions of the simulation box in the *x* and *y* directions are 51.6 Å and 52.3 Å, respectively. The distance between the mean center of mass of the innermost wall atoms is 50 Å. The initial water molecule configuration obtained by Grand Canonical Monte Carlo (GCMC) simulation, as shown in **Figure 3.7**, is used as input for MD simulation.

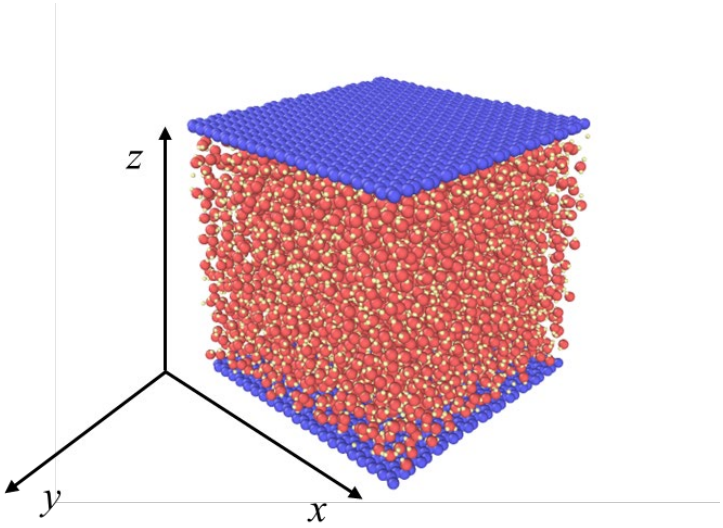

Figure 3. 7 The initial configuration of the system in MD simulation

An NVT ensemble is used for 1 ns to achieve the initial thermo-equilibrium, then an additional force is applied to each water molecule following equilibration. During the non-equilibrium process, water is allowed to heat up due to shear, while the temperature of the walls is maintained at 300 K using a Nosé-Hoover thermostat. The atom velocities and pressure tensors are updated under an NVE ensemble. Four

cases are run for comparison, with different applied forces from 1×10^{-15} ~ 2×10^{-14} N per molecule. Simulation is run with a time step of 1 fs to a minimum duration of 5 ns for the non-equilibrium process. It is found that the obtained velocity data by using a time step of 1 fs will not lead to significant deviations from that by using a time step of 0.5 fs.

3.2 Validation and discussion of the proposed model

3.2.1 Validation of the computations

Firstly, the velocities and pressures are obtained from MD simulation when the average velocity of water molecules stays constant and the system reaches a steady state. **Table 3.1** summarizes the average cross-section velocities and pressure tensors for all cases during the non-equilibrium dynamic process. The pressure tensors are computed for the slip plane with a height of 3 angstroms in MD simulation.

Table 3. 1 Summary of velocities and pressure tensors for all cases

Case	Force per molecule ($\times10^{-14}$ N)	Velocity (m/s)	Pressure tensor in the normal direction (MPa)
1	0.5	7.51	12.91
2	1	16.9	13.18
3	1.5	27.36	13.31
4	2	38.15	13.72

To validate the modified model proposed, firstly the friction force is computed by using the modified model as shown in equation (3.6), denoted as Method 1. In addition, another method is used to compare the results. It is known that at steady state conditions, the total applied force exerting on all molecules equals the total friction force acting on the two slip planes, and thus the friction force acting on a single water molecule can be computed, denoted as Method 2. This method is given by:

$$f_{\mathrm{f}} = F_{\mathrm{a}} \times N_{\mathrm{t}}/N_{\mathrm{s}} \tag{3.7}$$

where F_a is the applied force acting on a single molecule, N_t and N_s stand for the number of total water molecules in the system, and the number of water molecules in the two slip planes, respectively. Both N_t and N_s are output from MD simulation. Moreover, the friction force without correction for the work done by the substrate is also calculated, using the repulsive force multiplied by the vertical distance, denoted as Method 3. This method is given by:

$$f_f = (f_N \Delta z - \Delta E_{ad})/\Delta x \tag{3.8}$$

Figure 3.8 shows the comparisons. The horizontal coordinates stand for the friction force calculated by Method 1 and Method 3, while the vertical coordinates represent that obtained by Method 2. It is shown that Method 1 can quantify the friction at a water-graphene interface, and the traditional method without correction leads to errors in the calculation of the friction force. As mentioned in Section 3.1, there is no actual normal load acting on the water molecule, which is the main difference between a solid-solid friction process and a liquid-solid friction process.

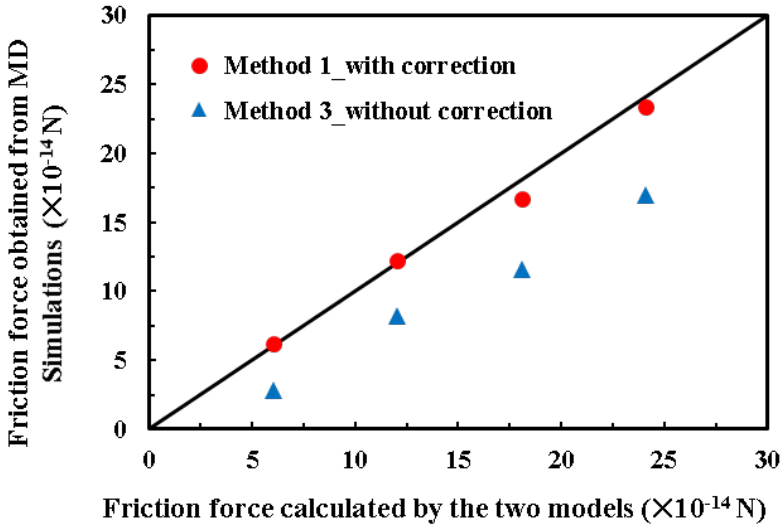

Figure 3. 8 Comparison of friction force obtained from MD simulation and that calculated by the model with and without corrections

3.2.2 Similarities between solid-solid, liquid-solid, and liquid-liquid friction processes

As the validated model is modified based on a model for solid-solid friction, it is exhibited that solid-solid friction and liquid-solid friction have similar mechanisms at the molecular scale, when the molecular structure of moving particles are simple. The contributions from the complex molecular structure of moving particles to friction are omitted, and the friction results from periodic energy barriers induced in the direction of relative motion between the contacting particles, which is due to the inhomogeneity of chemical energy and molecular structure of the substrate. Solid or liquid needs energy to overcome energy barriers and ensure relative motion, and the process to dissipate this energy leads to friction. Therefore, the energy barrier is the intrinsic source of friction. From this point of view, the friction process within liquid molecules is also related to energy barriers. Eyring proposed a theory for the mechanisms of momentum transport in liquids, according to which liquid flow is a process that molecules overcome the energy barriers under shear stress [229]. The energy barrier and viscosity follow an exponential form of relationship and the shear stress reduces the energy barrier in the flow direction. Equation (2.17) displays the hopping rate for a single water molecule under the applied external force based on Eyring's theory. It is noted that δ has a similar physical meaning with Δx for a liquid-solid friction process. The liquid-solid friction process is associated with water molecules overcoming the energy barriers which are reduced by the applied force. Thus, liquid-solid friction, solid-solid friction, and viscous friction within fluid at the molecular scale are all associated with overcoming energy barriers.

Moreover, one thing to mention is that the hopping rate equation predicts a non-zero velocity as long as an applied force exists. But in some realistic cases, the water molecules will be locked on the solid surface and the fluidity is highly reduced. This will be prevalent under strong hydrophilic conditions, where the energy barriers for water molecules are high, and epitaxial ordering may occur [216]. Under these cases, the slip behavior occurs occasionally. Some water molecules can diffuse into the bulk phase from the first peak density layer, leaving vacancies behind. The water molecules behind can hop and occupy the

vacancies, contributing to the slip behavior. Therefore, the slip behavior is not prevalent in these cases, which is termed molecular slip [269].

3.3 The relationship between friction force and slip behavior

For liquid-solid friction, the magnitude of the energy barrier is closely related to the slip behavior. As shown in equation (2.17), the hopping rate of a single water molecule is affected by the magnitude of the energy barrier, and each hopping event contributes to slip flow. The slip velocity resulted from the motion of a single water molecule equals the hopping rate times the distance for each hop:

$$V_s = \nu \times \delta \tag{3.9}$$

In order to establish a theoretical foundation between friction force and slip velocity for a single water molecule, two relationships need to be quantified. The first one is the relation between the friction force and the applied force acting on the water molecule, and the second one is the relation between the friction force and the energy barrier.

On one hand, the relationship between the friction force and the applied force exerting on a single water molecule in the slip plane is acquired from equation (3.7) when the system achieves equilibration. From MD simulation, the number density profiles for all cases are plotted, as illustrated in **Figure 3.9**. The first peak density layer in this Figure has the same physical meaning as the slip plane, which is beyond the water-graphene interface and is experienced by the friction force.

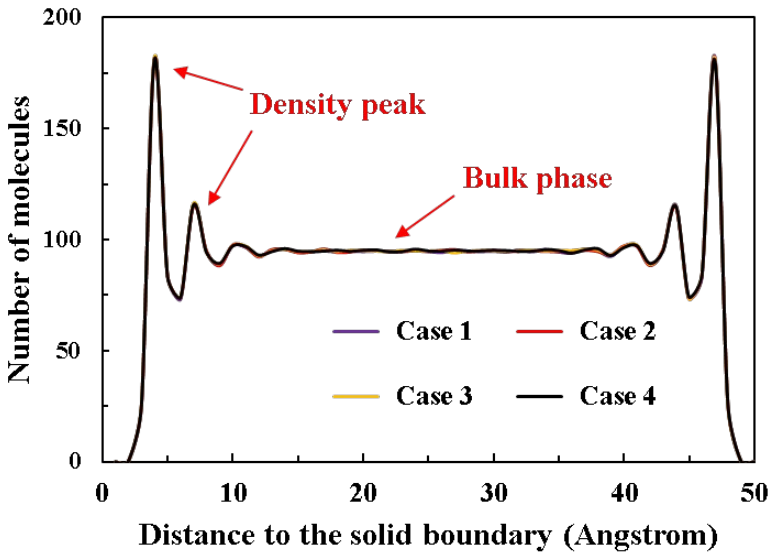

Figure 3. 9 Number density profiles for all cases

On the other hand, the relationship between the energy barrier ΔG_0 and the friction force can be discussed based on the concept of Gibbs free energy. The energy barrier is also termed activation energy by some scholars, indicating the extra energy required for a molecule to hop from an equilibrium state to a transition state [36,41,272–274]. The Gibbs free energy is lowest when water is at the equilibrium state, and a transition state corresponds to the highest Gibbs free energy [41,274]. Based on the definition of Gibbs free energy change, an energy barrier, or activation energy, is characterized by:

$$\Delta G_0 = \Delta U + \Delta(PV_m) - \Delta(TS) \tag{3.10}$$

where P is pressure, V_m is the volume of a molecule, U is the internal energy, and S is entropy. It is assumed that the entropic term TS is constant [269]. Besides, the kinetic energy of the molecule does not change as the water temperature is constant, and thus the change in the Gibbs free energy is the sum of the potential energy difference and the volume work done by graphene. It is noted that the potential energy difference is the adsorption energy difference, as both terms represent van der Waals interactions between molecules. Therefore, equation (3.10) can be reduced to:

$$\Delta G_0 = \Delta E_{ad} + \Delta(PV_m) \tag{3.11}$$

For a hopping event from site H to site B, the positive work done by graphene is equivalent to reducing the volume of the molecule, so that $\Delta(PV_{\mathrm{m}})$ will be negative [268]. Besides, the adsorption energy difference between the final state at site B and the initial state at site H will be positive, as can be seen in **Figure 3.3**. As introduced in Section 3.1, the maximum potential energy variance $\Delta E_{\max}$ is induced owing to the work done by the repulsive force which is partly compensated by the adsorption energy difference, therefore, a theoretical foundation can be obtained by:

$$\Delta G_0 = \Delta E_{\mathrm{ad}} - W_{\mathrm{rep}} = (E_{\mathrm{B}} - E_{\mathrm{H}}) - (E_{\mathrm{M}} - E_{\mathrm{B}}) = -\Delta E_{\max} \tag{3.12}$$

In addition, the maximum potential energy variance $\Delta E_{\max}$ equals the friction force f_{f} multiplied by the distance δ from the view of dissipation. Thus, the relationship between the friction force and the energy barrier is obtained by:

$$\Delta G_0 = -f_{\mathrm{f}} \times \delta \tag{3.13}$$

Combined equations (2.17), (3.7), (3.9), and (3.13), the relationship between the friction force and the slip velocity is eventually obtained by:

$$V_{\mathrm{s}} = \frac{\delta kT}{h}\{\exp\left[\frac{(1+\frac{N_S}{N_t})f_{\mathrm{f}}\delta}{kT}\right] - \exp\left[\frac{(1-\frac{N_S}{N_t})f_{\mathrm{f}}\delta}{kT}\right]\} \tag{3.14}$$

This theoretical relation is plotted in **Figure 3.10**, and the data for slip velocity-friction force relation obtained from MD simulation for each case are also shown for comparison. As the velocity data points obtained from MD simulations are statistical, error bars are added. The range of the error bar is set as 5 m/s, because it is found that most data points are within this range.

It is displayed that the theoretical relation fits very well with the MD results, and thus the theoretical relationship is validated.

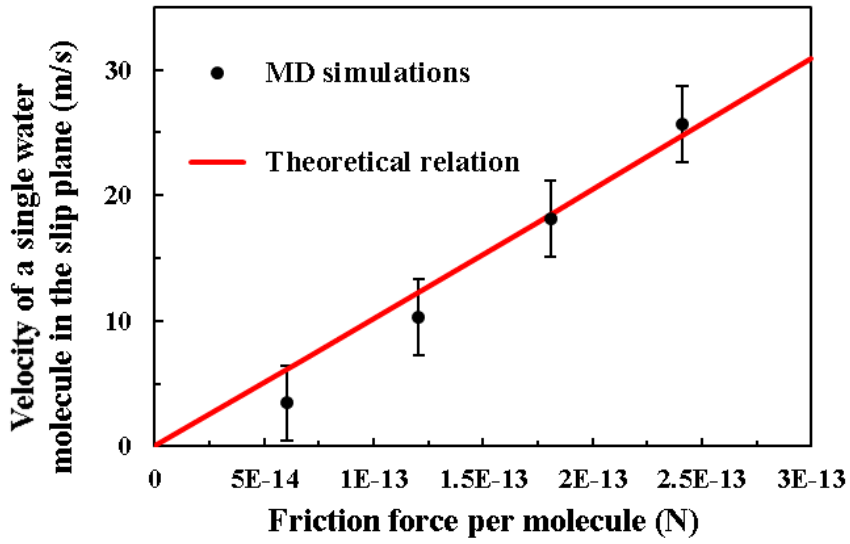

Figure 3. 10 Comparison of the data obtained from MD simulation and that calculated by the theoretical foundation

It is therefore concluded that the slip velocity of the slip plane and the friction force at the interface follow a hyperbolic-like relationship, and a linear relationship is acquired when the friction force is low. In reality, when this relation is beyond the linear regime, the applied driven force will be too high for a real experiment. The velocities and temperatures of the slip plane for more cases with higher applied driven forces are also plotted, as shown in **Figure 3.11**. It can be observed that when the applied force is higher, the temperature of the slip plane will exceed 300 K, which means that the thermostat will be unreliable. Moreover, it is shown that in these cases, the slip velocity is over 50 m/s, beyond which the non-linear in the flow rate begins to occur, which is unrealistic. It is reported that the velocity of molecules should be one order of magnitude lower than the thermal velocity (340 m/s) to be reliable [275,276].

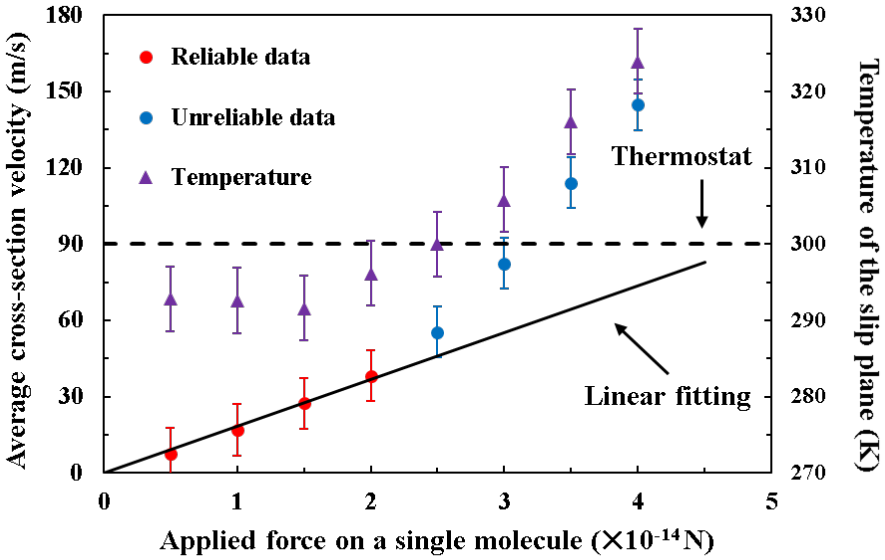

Figure 3. 11 Velocities and layer temperatures of the slip plane for more cases

It is acknowledged that the fast slip of water above the graphene substrate arises from two aspects, including a weak interaction between water molecules and the graphene substrate, and a smooth structure of graphene [137,170,277–279]. Both aspects contribute to a small energy barrier for a motion of the water molecule, leading to a significant slip behavior. In **Figure 3.12**, the average cross-section flow rates for water flow between graphene sheets with a separation of 5 nm, and that with a traditional no-slip boundary condition are plotted. It is displayed that the slip behavior contributes significantly to the total flow rate for water flow between graphene sheets, and thus a precise estimation of the boundary condition is important.

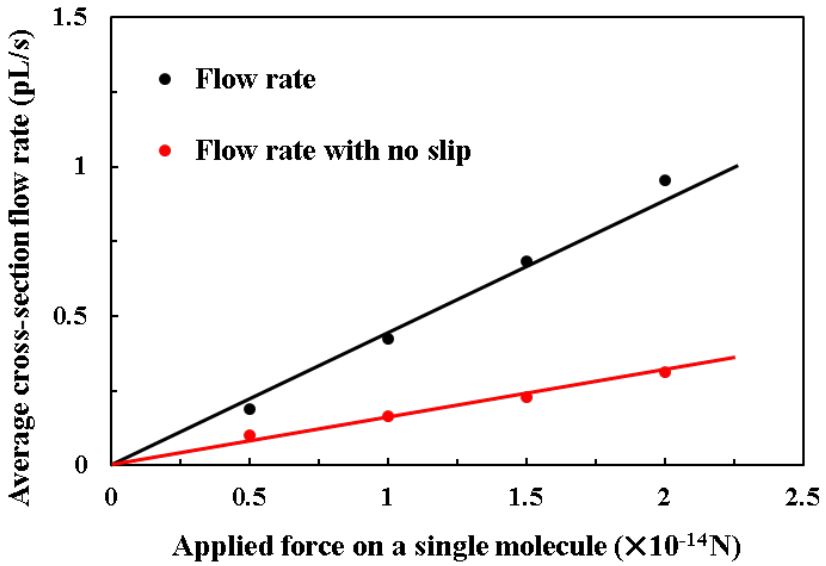

Figure 3. 12 Average cross-section flow rate with and without slip velocity

In this theoretical foundation, all parameters have clear physical meanings and there are no empirical parameters. Moreover, it omits the necessity to compute the slip length, which is usually difficult to quantify. The reported slip lengths in literature are scattered, spanning over several orders of magnitude [33,132,161–164]. Therefore, the proposed foundation between the friction force and the slip velocity provides a new way to determine the boundary condition for the flow of simple liquids at nanoconfined conditions.

3.4 Summary

In this part, the molecular-scale friction force at the water-graphene interface is computed, by a modified solid-solid friction model combined with MD simulation. A new method to calculate the work done by the graphene substrate is proposed to capture the physics of water, based on the total L-J potential curves. The reliability of the results is validated by force balance during the non-equilibrium dynamic process. It is concluded that liquid-solid friction has similar mechanisms compared with solid-solid friction, in terms of the energy barrier. Both friction processes arise from the dissipation of the energy that is acquired by

the molecules to overcome energy barriers. Moreover, this theory can be extended and compared with a classic molecular kinetic theory, which reveals the origin of viscous force within fluid molecules.

In addition, the relationship between the slip process and friction is analyzed, and a theoretical foundation between slip velocity and friction force is obtained. The velocity of the water molecule in the slip plane and the friction force acting on it follow a hyperbolic-like relationship, and a linear relation can be recovered under realistic experimental conditions. This theoretical foundation provides a new way to determine the boundary condition for simple liquids flow above the graphene substrate.

Chapter 4 The increased viscosity effect for fracturing fluid imbibition in shale

Understanding water imbibition behaviors in shale formations plays an essential role in shale gas development. The effective viscosity of water in shale nanopores is usually different from that of the bulk phase because of the confined conditions. In this part, a model considering interactions between water and a solid surface is proposed to predict the effective viscosity of water at the nanoscale, which is inserted into the classic L-W model to describe the water imbibition behavior in shale formations. This model is derived based on a molecular kinetic theory and incorporates the disjoining pressure. Published experimental data is used to validate the model. It is demonstrated that the effective viscosity of water in hydrophilic nanopores is much higher than that of the bulk phase due to strong interactions between water and a solid surface, and the deviation significantly increases when the separation is below 10 nm. For a hydrophilic capillary tube with a diameter of 10 nm, the water effective viscosity is approximately 2.5 times higher than that of the bulk phase. Moreover, this deviation is larger for a capillary tube compared with a capillary channel, due to the curvature effect. Besides, the effective viscosity for water under a hydrophobic condition is smaller than the bulk phase water, because the structural repulsive force dominates under a hydrophobic condition. This work establishes a theoretical foundation to calculate the effective viscosity for water flow at the nanoscale. Furthermore, it helps to understand fracturing fluid imbibition behavior in shale gas reservoirs, which will benefit the simulation of fluid flow at the reservoir scale.

4.1 Models for effective viscosity and spontaneous imbibition

According to the Molecular kinetic theory, the impact of surface forces on water flow properties is reflected in the difference of an energy barrier ΔG_0. Water molecules within the bulk phase only interact with other water molecules surrounded. However, those molecules near the solid surface interact both

with water molecules and solid molecules. Thus, energy barriers are spatially varying for water molecules at different locations. Some scholars defined the concept of an energy barrier as activation energy, meaning extra energy required for a molecule to hop from an equilibrium state to a transition state. The Gibbs free energy is lowest when water is at the equilibrium state, and a transition state corresponds to the highest Gibbs free energy [274]. Based on the definition of Gibbs free energy, an energy barrier, or activation energy, is characterized by:

$$\Delta G_0 = \Delta U + \Delta(PV) - \Delta(TS) \tag{4.1}$$

where U is the internal energy in J and S is the entropy in J/K. P and V are pressure in Pa and volume in m^3, respectively. The solid surface is assumed smooth, and the variation of adsorption energy along the surface is negligible, indicating that ΔU is zero. Also, the entropic term TS and pressure P are usually assumed constant for a hopping event [268,269]. Therefore, equation (4.1) reduces to:

$$\Delta G_0 = P\Delta V \tag{4.2}$$

ΔV is considered as the volume difference of vacancy in the transition state and equilibrium state, and its calculation is proposed by Glasstone et al. [230]:

$$\Delta V = -f\frac{4\pi}{3}\left(\frac{\sigma}{2}\right)^3 \tag{4.3}$$

where f is a fitting factor, which equals unity when the applied shearing is small, and σ is the L-J size parameter. For water in the bulk phase, the liquid-liquid L-J size parameter σ_{LL} is used, while the liquid-solid L-J size parameter σ_{LS} is applied for water near a solid surface. It is known that the first two layers with a thickness of approximately 0.7 nm are strongly affected by the solid surface, as there are usually two density peaks on water density profiles [255]. Therefore, it is regarded that the water within the first two layers use the liquid-solid L-J size parameter σ_{LS}, and that beyond these two layers apply the liquid-liquid L-J size parameter σ_{LL}.

For water molecules at different locations, the pressure is different due to the impact of surface forces. If P_0 is defined as the pressure in the bulk phase and P_l as the pressure of water at a location with a distance

l to the solid surface, the difference between P_l and the pressure in the bulk phase is called the solvation pressure, which has the same physical meaning as the disjoining pressure $\Pi(l)$ [268,269]. Thus the viscosity ratio of water under the influence of a surface force to that in the bulk phase can be calculated by:

$$\frac{\mu_l}{\mu_0} = \exp\left(\frac{\Delta G_0(l) - \Delta G_0(0)}{kT}\right) \tag{4.4}$$

Combining equations (4.2) to (4.4), this relation can be expressed as:

$$\frac{\mu_l}{\mu_0} = \exp\left[\frac{(P_0 - P_l)\Delta V}{kT}\right] = \exp\left(-\frac{\Pi_l \pi \sigma^3}{6kT}\right) \tag{4.5}$$

To apply the above theory to the description of a spontaneous imbibition process, an effective viscosity is necessary to ensure the application of a continuum model. The effective viscosity for a slit nanopore is calculated by:

$$\mu_e(H) = \frac{\int_0^{\frac{H}{2}} \mu_l dA}{A} = \frac{\int_0^{r^*} [W\mu_0 \exp\left(\frac{\Pi_l \pi {\sigma_{LL}}^3}{6kT}\right)]dr + \int_{r^*}^{\frac{H}{2}} [W\mu_0 \exp\left(\frac{\Pi_l \pi {\sigma_{LS}}^3}{6kT}\right)]dr}{W\frac{H^*}{2}} \tag{4.6}$$

where l is the distance to a solid surface, W is a channel width, H is a channel height, r is the distance to the middle of a streamline, and r^* is the distance from the boundary of the two water density layers to the middle of the streamline. Additionally, the effective viscosity for a cylindrical nanopore is given by:

$$\mu_e(D) = \frac{\int_0^{r^*} [2\pi r\mu_0 \exp\left(\frac{\Pi_l \pi {\sigma_{LL}}^3}{6kT}\right)]dr + \int_{r^*}^{\frac{D}{2}} [2\pi r\mu_0 \exp\left(\frac{\Pi_l \pi {\sigma_{LS}}^3}{6kT}\right)]dr}{\pi(\frac{D}{2})^2} \tag{4.7}$$

where D is the diameter of a nano capillary tube.

A spontaneous imbibition process is usually described by the L-W model, which relates the imbibition length to time. The classical L-W model is modified by incorporating the effective viscosity as follows:

$$L(t) = \left(\frac{2KP_C}{\mu_e}\right)^{\frac{1}{2}} t^{-\frac{1}{2}} \tag{4.8}$$

where P_C is the capillary pressure and K represents permeability given by [280]:

$$K(H) = \frac{H^2}{12}$$

$$K(D) = \frac{D^2}{32} \tag{4.9}$$

where K(H) is permeability for a nanochannel in m^2 when its width is much larger than the channel height, and K(D) is permeability for nanocapillary in m^2. Therefore, the spontaneous imbibition length can be estimated by combing equations (4.6) – (4.9).

4.2 Model validation

In order to check the validity of the proposed model, the results predicted by the model are compared with the published experimental data [219,221,222,281]. The calculating parameters are listed in **Table 4.1**.

Table 4. 1 A summary of parameters in calculations

Parameter	Symbol	Unit	Value	Reference Value
Temperature	T	K	297	
Viscosity of bulk phase	μ_0	Pa s	0.001	
Boltzmann constant	k	10^{-23} J/K	1.38	
Liquid-solid L-J size parameter for clay	σ_{LS}	nm	0.225	0.22-0.23 [282]
Liquid-solid L-J size parameter for organic matters in shale	σ_{LS}	nm	0.34	0.3-0.35 [283]
liquid−liquid L-J size parameter for bulk phase water	σ_{LL}	nm	0.32	
Contact angle for clay	θ	Dimensionless	0	0 [219,221]
Contact angle for organic matters in shale	θ	Dimensionless	100	100 [122]
Surface tension	γ	N/m	0.073	
Hamaker constant for clay	A_H	10^{-20} J	5.0	4.7-5.0 [284]
Hamaker constant for organic matters in shale	A_H	10^{-20} J	0.1	0.1-1.0 [285]
Permittivity of vacuum	ε_0	10^{-12} F/m	8.85	

Relative permittivity of water	ε	Dimensionless	81.5	
Difference of electric potentials	$\Delta\zeta$	mv	50	0-80 [286]
Coefficient of structural force for clay	k	10^7 N/m^2	1	-5-2 [286]
Coefficient of structural force for shale	k	10^7 N/m^2	-1	-5-2 [286]
Thickness of hydration layer	λ	nm	1.5	1.0-2.0 [286]

4.2.1 Validation of the effective viscosity

Figure 4.1 shows the ratio of the effective viscosity to the bulk viscosity calculated by the proposed model and those acquired from the literature [33,41,219,221,222,287,288]. The vertical axis represents the ratio calculated by the model and the horizontal axis corresponds to the results obtained from experiments. The effective viscosity values obtained in the literature are calculated based on the imbibition curves reported by the authors. The effective viscosity is calculated according to the slope of the L^2 vs t straight line. As there are usually small tolerances for the data points, the error bars are added to the effective viscosity values.

Equation (4.6) is used to calculate the effective viscosity ratio for a nano-channel, and equation (4.7) is used to predict that for a nano-capillary. A diagonal line is shown for comparison. The results match very well for all experiments, which validates the effective viscosity model. Moreover, the ratio of the effective viscosity to the bulk viscosity is also plotted as a function of the channel height for nano slits and compared with those from published data, as shown in **Figure 4.2**. The proposed effective viscosity model for a nano-channel can predict the effective viscosity ratio for different channel widths. Numerous values for various channel widths are calculated, and a curve is obtained as shown in this Figure. The data points in this Figure are also from the experimental results. It is illustrated that all of the data points are close to the blue curve, and thus the proposed effective viscosity model is validated. Moreover, this Figure shows the proposed viscosity model is capable of predicting the trend of the viscosity ratio as a function of the channel height, and it can be seen that the effective viscosity significantly deviates the bulk phase value for a channel with a width of below 10 nm.

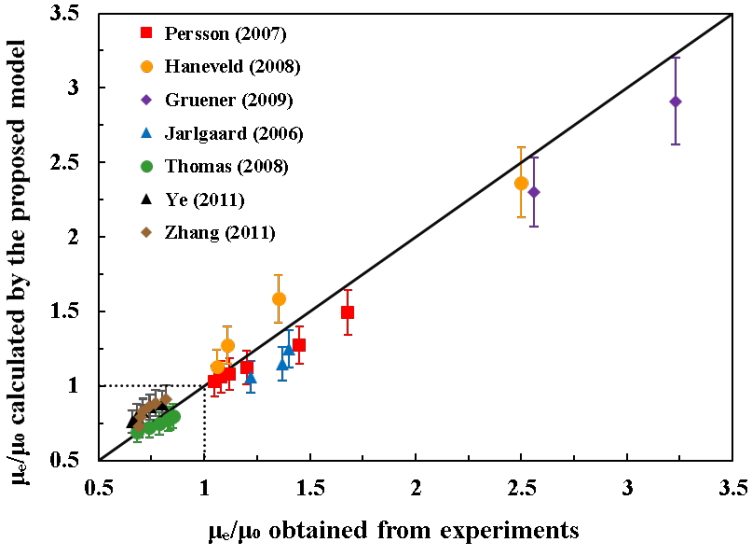

Figure 4. 1 Comparison of the viscosity ratio calculated by the model and those obtained from experiments

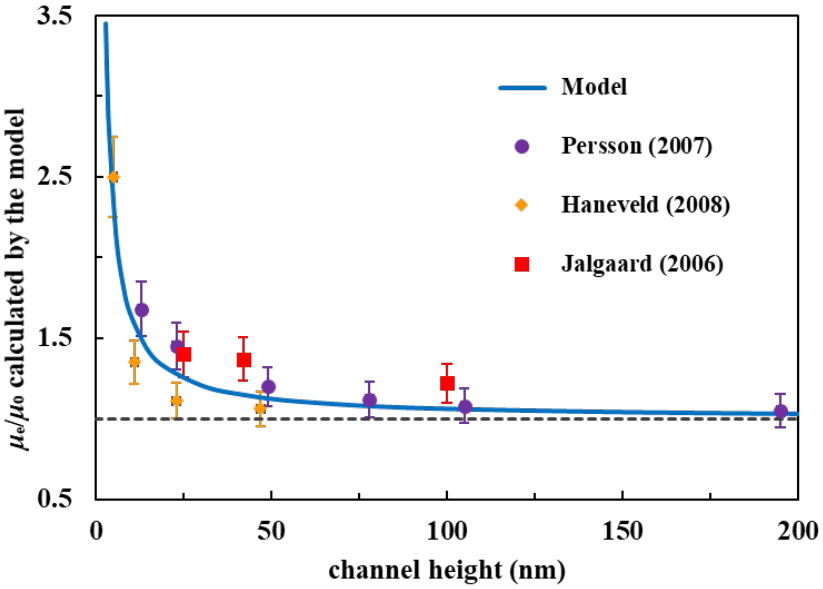

Figure 4. 2 Comparison of the viscosity ratio as a function of channel height calculated by the model and those obtained from experiments

4.2.2 Validation of the spontaneous imbibition

The validity of the model for spontaneous imbibition is also checked by published data from the literature. The experiments conducted by Haneveld et al. [221] are chosen for this validation. In their experiments,

the solid material is a silicon-based rectangular pore, and the pore height is 5, 11, 23, and 47 nm, respectively, while the width is 20 μm. In **Figure 4.3**, the imbibition behavior predicted by equation (4.8) and that obtained from experiments are compared. The data points in this Figure show the recorded imbibition length as a function of time. Moreover, the imbibition rate is calculated as a function of time, and four curves are plotted. These four curves correspond to the imbibition behavior for water in a nanochannel with the four channel widths used in the experiments. It can be seen that the data points and the plotted curves match reasonably well, and thus the modified L-W model is validated. However, it can be seen that for channel widths of 5 nm and 11 nm, the predicted imbibition length is slightly higher than the measured imbibition length. This small deviation is attributed to two reasons.

First, the surface roughness may further increase the flow resistance. This influence can be estimated by correcting the effective height of channels with a small distance ΔH. Ouyang et al. estimated this value to be approximately 0.229 nm [289], and this value should depend on the materials and fabrication methods [290]. Second, the possible formation and entrapment of nanobubbles may occur at the advancing liquid meniscus, leading to an immediate decrease in the filling speed [291]. This effect is associated with the dissolved gas or contaminant. These two reasons may be responsible for the small deviation between the predicted imbibition length and the measured one for channel widths of 5 nm and 11 nm in **Figure 4.3**.

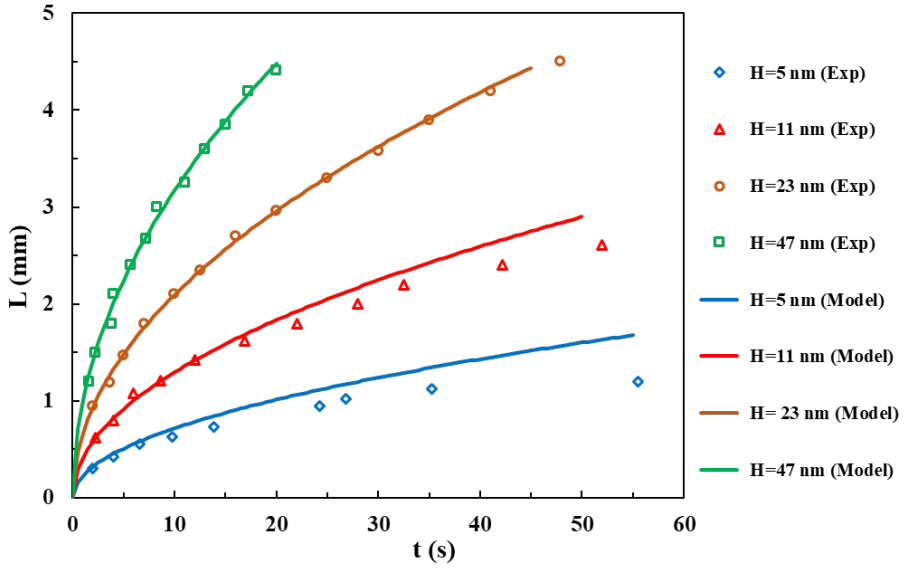

Figure 4. 3 Comparison of the imbibition length calculated by the model and that obtained from experiments

4.3 Results and discussion

4.3.1 Effective viscosity versus geometrical factors

The effect of geometrical factors on the effective viscosity is shown in **Figure 4.4**. The geometric factors include the shape of the cross-section for the flow area and the characteristic length of the cross-section. The characteristic length is the diameter for a capillary tube and the height for a capillary channel. In this Figure, the red curve for a nano-channel is plotted based on equation (4.6), and the blue curve for a nano-capillary is plotted according to equation (4.7). It is demonstrated that the effective viscosity increases rapidly when the characteristic length is down to 10 nm. This trend clarifies that extreme confinement leads to a significant deviation for the effective viscosity, due to the influence of surface forces induced by solid. When the characteristic length approaches approximately 100 nm, the viscosity ratio decreases closely to unity. This trend can be explained by a disjoining pressure curve. As shown in **Figure 4.5**, the disjoining pressure as a function of the distance to the lower solid surface is plotted for a slit nanopore. It is obvious that the disjoining pressure elevates fast when water approaches closely to the solid surface, meaning that the viscosity increases rapidly in a near-surface region. When the separation of the two solid surfaces is down to several nanometers, the region with a significantly increased viscosity accounts for a great proportion, and thus the effective viscosity is much larger than that of the bulk value. When the separation gets larger, the proportion of the region with a significantly increased viscosity becomes less, leading to a lower effective viscosity.

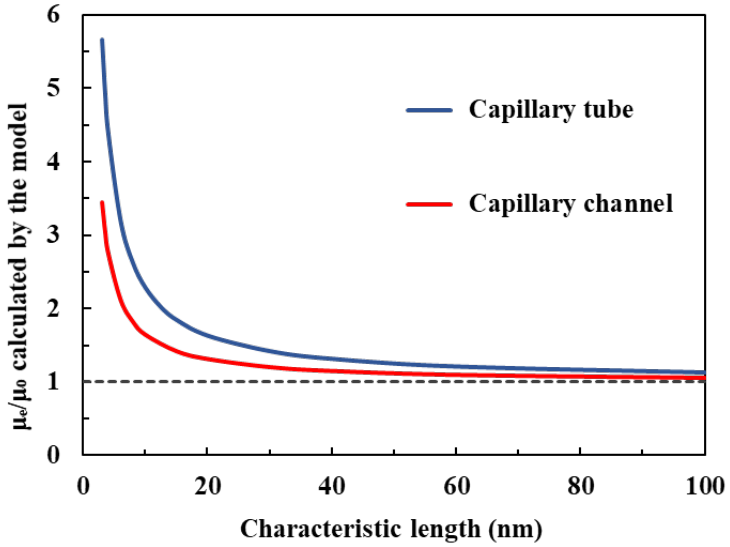

Figure 4. 4 Relationship between viscosity ratio and geometrical factors

However, it is noted that the proposed model is only applicable to nanopores whose characteristic length is larger than 1~2 nm. This precondition ensures that the confined water can be modeled by the continuum theory. When the confinement is so small that the regions influenced by surface forces from two solid surfaces overlap, new phenomena will occur during an imbibition process, which cannot be described by the continuum model. A review on various transport phenomena' at different length scales stated that when the limit is such that only one molecule can enter a confining pore, single-file water transport occurs [35]. In this case, the deviations from bulk hydrodynamics will be more drastic, and various specific phenomena show up, including non-Fickian transport, ion transfer, and stochastic flow. When the separation is large enough to ensure the existence of a bulk phase, the disjoining pressure curve will decrease to zero in the bulk phase, as shown in **Figure 4.5**.

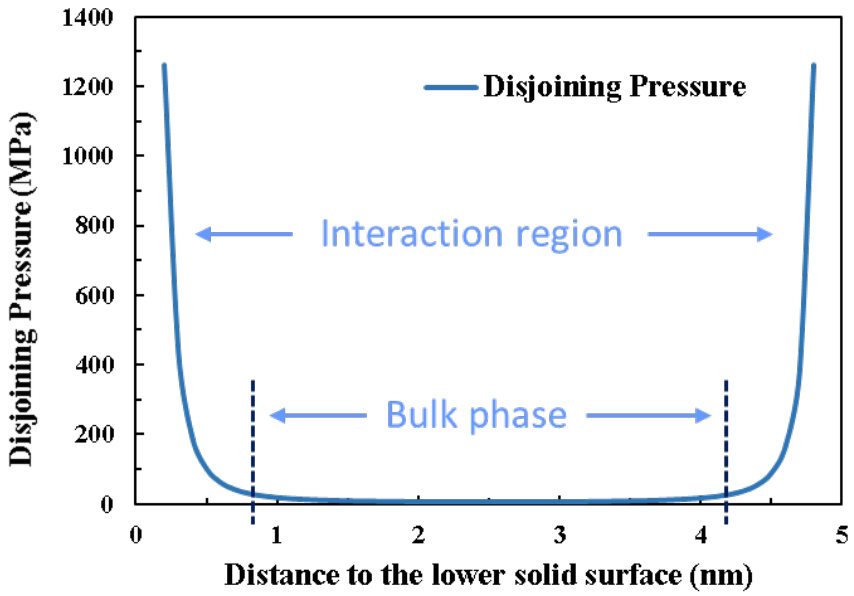

Figure 4. 5 Disjoining pressure curve for slit nanopore with a channel height of 5 nm

Apart from the characteristic length, another factor that affects the effective viscosity is the shape of a nanopore. For the same characteristic length, the effective ratio for a nanopore with a cylindrical shape is always larger than that with a slit shape, and this effect amplifies when confinement increases. This is due to the curvature effect induced within a cylindrical shape nanopore. If the solid material is the same for the cylindrical nanopore and slit nanopore, the region under the influence of a solid surface for a cylindrical nanopore is larger than that for a slit nanopore, leading to a larger effective viscosity.

4.3.2 Effective viscosity versus solid properties

Shale gas reservoirs are composed of inorganic matters and organic matters, and thus there are both hydrophilic and hydrophobic nanopores in shale gas reservoirs. The effective viscosity of confined water within pores with different wettability is different, as wettability represents the interaction strength between water and solid materials. **Figure 4.6** shows the comparison of the effective viscosity of water confined in slit nanopores of clay and organic matters in shale; the former represents hydrophilic inorganic matters and the latter stands for hydrophobic organic matters. Both curves are plotted based on equation

(4.6), but the parameters are different for the two wettability conditions. The values of parameters used in the calculations are listed in **Table 4.1**.

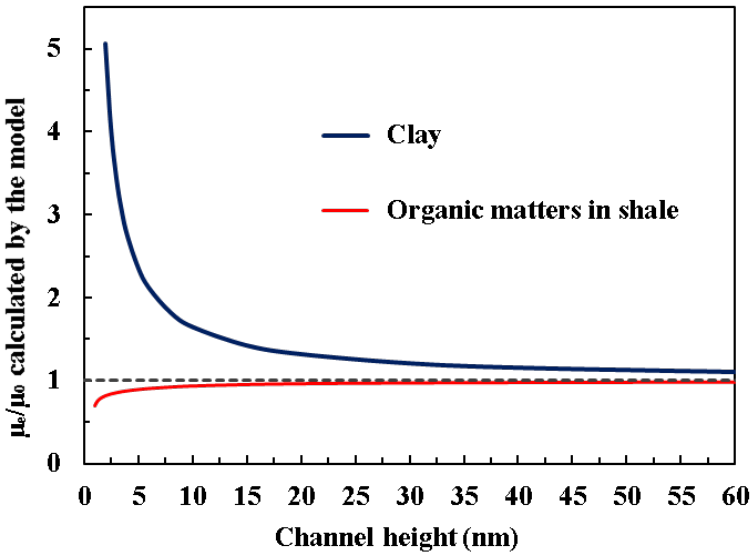

Figure 4. 6 Comparison of the effective viscosity of water confined in slit nanopores of clay and organic matters in shale

It can be seen that the effective viscosity for water in hydrophilic nanopores is always greater than the bulk phase viscosity while an opposite trend exists for that in the hydrophobic nanopores. This implies that wettability is a key factor that controls the effective viscosity for nanoconfined water flow. Moreover, the effective viscosity deviates more significantly under hydrophilic conditions compared with its decrease under hydrophobic conditions, especially when the channel height is below 10 nm. For example, the calculations show that for a channel height of 2 nm, the ratio of the effective viscosity to the bulk phase viscosity under the hydrophobic conditions is 0.822, while that under hydrophilic conditions reaches 5.056. Furthermore, this ratio reduces to 1.104 under the hydrophilic conditions when the channel height is 60 nm, and the increased effect is still non-negligible. However, the ratio approaches very close to the bulk phase value when the separation is over 20 nm. Furthermore, this reduced viscosity effect also explains why a water flow rate is much higher under hydrophobic conditions at the nanoscale. For a

spontaneous imbibition process that occurs under hydrophilic conditions, the effective viscosity is always greater than the bulk phase viscosity, which cannot be neglected.

In order to further analyze the impact of wettability on the effective viscosity, different components of the disjoining pressure that contribute to the effective viscosity are compared. As described in Chapter 2, there are three parts composing the disjoining pressure, including a molecular component, an electrical component, and a structural component. In equation (4.4), it is shown that the effective viscosity is determined by $\Delta G_0(l)$-$\Delta G_0(0)$. As $\Delta G_0(0)$ represents the energy barrier for water in the bulk phase, the difference between the energy barrier at a distance l and the bulk phase energy barrier is defined as the additional energy barrier, indicating the influence of the solid surface on the energy barrier. The additional energy barrier contributing from three components as a function of the distance of water to the solid surface under hydrophilic conditions is plotted in **Figure 4.7**. It is obvious that the molecular component dominates for water in clay nano slits. The electrical component is negligible compared with the molecular component, so is the structural component. Thus, under hydrophilic conditions, the van der Waals interactions between the solid surface and water tend to increase the viscous drag within water near the solid surface, which is the primary reason for the increased viscosity effect for spontaneous imbibition under hydrophilic conditions.

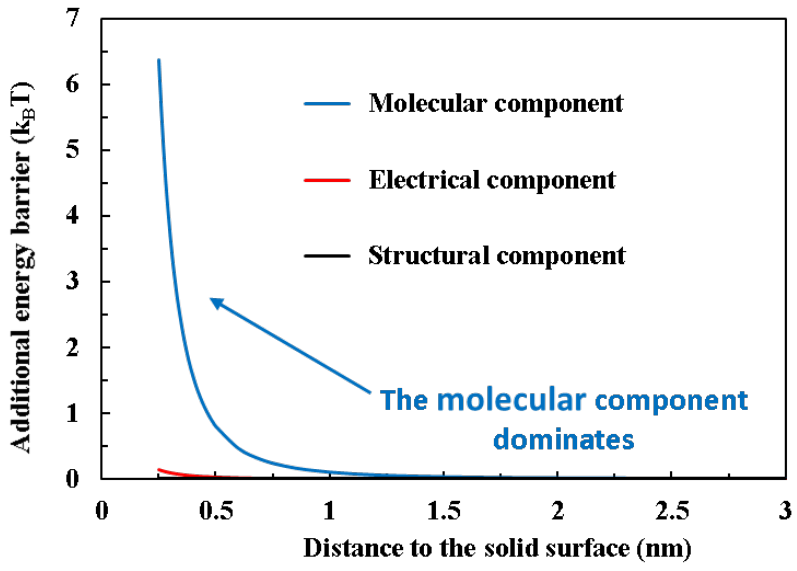

Figure 4. 7 Comparison of the contribution from different components to the additional energy barriers for water confined in slit nanopores of clay in shale

Besides, the relationship between the additional energy barrier and the distance of water to the solid surface under hydrophobic conditions is illustrated in **Figure 4.8**. It can be seen that the structural component is the dominant one compared with the other two components, and this component is a negative value, which tends to reduce the additional energy barrier of water. This is the main reason for the effective viscosity to be less than the bulk phase viscosity. The structural component implies the hydrophobic repulsive force acting on water molecules close to a pore wall inducted by a solid surface. It has a negative value because it has an opposite effect compared with the van der Waals interactions. The parallel orientations of water molecules to the solid surface may occur when this interaction is strong, as can be seen in **Figure 4.8**. This changed structure leads to reduced viscous drag within water near the solid surface, and thus the energy barrier, as well as the viscosity of water, are decreased. Besides, it can be seen that the magnitude of the additional energy barriers induced by these components is small compared with that caused by the molecular component under the hydrophilic conditions, thus the deviation from the bulk phase viscosity under the hydrophobic conditions is much less compared with that under hydrophilic conditions.

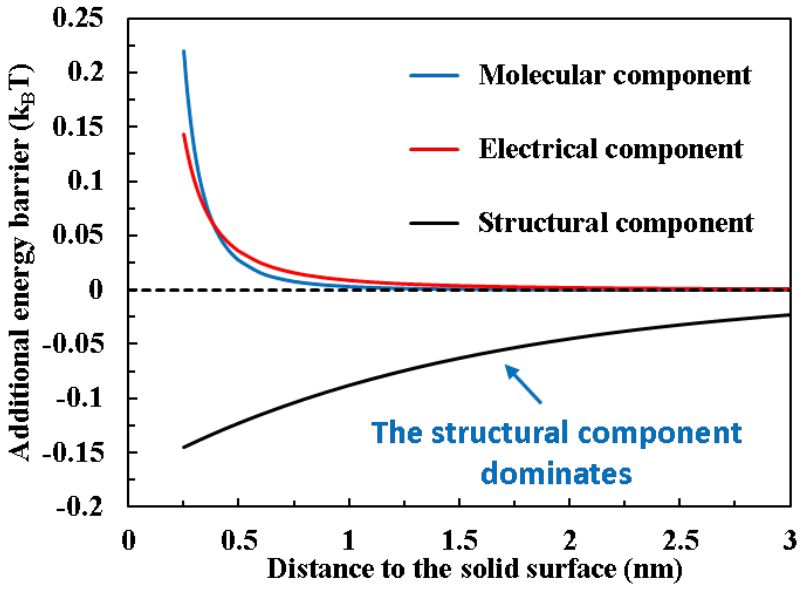

Figure 4. 8 Comparison of the contribution from different components to the additional energy barriers for water confined in slit nanopores of organic matters in shale

4.3.3 Spontaneous imbibition behavior

The L-W model is usually used to calculate the imbibition length. **Figure 4.9** compares the imbibition length calculated by the proposed model and that obtained by the classic L-W model without the correction for the effective viscosity. The solid lines are plotted according to equation (4.8), and the dashed lines are plotted based on the classic L-W model. It is shown that ignoring the effect of the effective viscosity leads to a deviation of the imbibition length, and the deviation becomes more significant when a channel height is small. This trend also shows that the effective viscosity increases with confinement. For a slit nanopore with a separation larger than 50 nm, the effect of the increased viscosity is much smaller. As there are abundant micropores and mesopores in shale gas reservoirs, the correction for the effective viscosity is necessary.

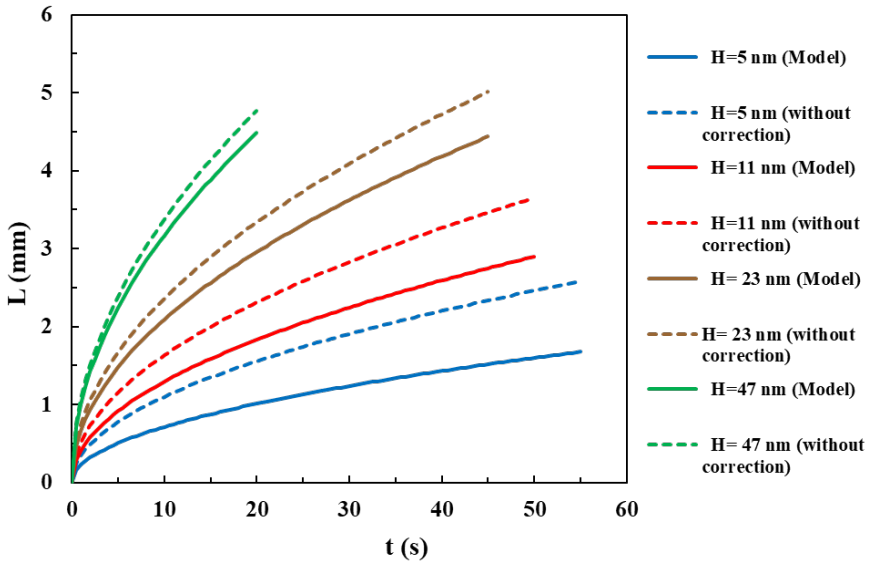

Figure 4. 9 Imbibition length predicted by the proposed model and the classic L-W model

Although the proposed model accounts for the effect of water-solid interactions by using an effective viscosity in the classic L-W model, this model still predicts that the imbibition length and the square root of time follow a linear relationship which the classic L-W model describes. However, this relationship

was found to deviate significantly from linearity in some core experiments [292]. This phenomenon arises from other factors leading to water retention in the shale matrix. For example, abundant charged clay minerals can adsorb water molecules through interlayer spaces, which is referred to as clay hydration. Some researchers reported that an imbibed volume in some core samples can be greater than an initially measured pore volume, indicating the strong adsorption of water by semi-permeable clay membranes [122]. Moreover, low pore connectivity and strong heterogeneity in pore types are other important factors. Furthermore, another important phenomenon that leads to the nonlinearity of the imbibition behavior is the deformation of the interface. Experimental evidence of irregular menisci has been reported in the literature. For example, Kim et al. observed multi-curvatures at the edge of a meniscus for low viscosity polymer flow in nanochannels, which results in a reduction of the effective cross-sectional area [293]. Van Honschoten et al. also found a deformed interface at the water imbibition front, the radius of which was much larger than that predicted by the macroscopic Kelvin equation [34]. Some models have been proposed to account for this effect. For example, Kelly et al. proposed a model that demonstrates how van der Waals forces lead to local menisci deformation and an average reduction in capillary pressure [214]. Moreover, Stoberg et al. verified by MD simulations that this effect can be accounted for by a dynamic contact angle [104]. However, the interfacial deformation phenomenon and a possible formation of a precursor film ahead of the meniscus under a strong hydrophilic condition requires further research. Therefore, many other mechanisms lead to a nonlinear relationship between the imbibition length and the square root of time, which makes the imbibition behavior more complex than a classic capillary filling.

One more thing to discuss is the initial water thickness in the shale formations. Li et al. proposed a reliable method for the estimation of the initial water film thickness under experimental conditions [68]. The initial water film thickness is calculated based on the relationship between the disjoining pressure and RH:

$$\Pi(l)V_m = -RTln\frac{P_v}{P_0} \tag{4.10}$$

This is an extended formula based on the Kelvin equation to describe the relationship between the RH and pressure difference of two phases [34]. The thickness of the initial water film can be computed based on the disjoining pressure curve.

The estimation of the initial water film thickness is meaningful, as it provides information on water distribution characteristics in shale formations. It is found that the initial water film thickness is approximately 1~3 nm, implying that the small pores with a characteristic length less than this value will be blocked by the initial water. These small pores are invalid for gas transport and storage, as well as spontaneous imbibition of fracturing fluid. Moreover, the proposed model is valid for nanopores larger than 1 to 2 nm as the continuum theory will be invalid for extreme confinement. For very small pores with a separation of less than 2 nm, the capillary condensation will occur under realistic reservoir conditions, as the initial water film is usually 1 to 3 nm. This means that the extremely narrow pores that cannot be described by the proposed model are usually filled with initial water and is not open for spontaneous imbibition. Larger pores that allow for imbibition can be described by the proposed model, and thus the proposed model is meaningful and useful. However, the effective flow area of a cross-section is reduced when there is an initial water film, which should be considered to ensure a precise quantification of an imbibition rate.

4.4 Summary

In this part, a theoretical model for the effective viscosity for water imbibition in shale formations is proposed, according to Eyring's molecular kinetic theory. The strong interactions between water molecules and solid surfaces are considered based on the disjoining pressure. The proposed viscosity model is validated by experimental results in the published literature. The main factors that affect the effective viscosity, including a pore size, a pore shape, and the properties of a solid material, are discussed. The main conclusions are summarized as follows:

(1) The effective viscosity is much higher for water under confined conditions, and it increases rapidly when the characteristic length of nanopores is lower than 10 nm. The effective viscosity for cylindrical nanopores is always larger than that for slit nanopores when the characteristic lengths are the same, and the difference is more obvious for small nanopores.

(2) Wettability is a key factor that controls the magnitude of the effective viscosity. The effective viscosity for water under hydrophilic conditions is much higher than that of the bulk phase while that under hydrophobic conditions is smaller. The molecular component is the dominant mechanism that contributes to the increased viscosity under the hydrophilic conditions, and the structural component induced by the repulsive force is the primary factor on the reduced viscosity under hydrophobic conditions.

(3) The proposed model considering the increased viscosity can predict spontaneous imbibition behavior, and ignoring this effect leads to huge errors, especially when the characteristic length is very small. Furthermore, other mechanisms may lead to water retention in reservoirs, including clay hydration and heterogeneity of pores.

(4) The disjoining pressure curve can be used to estimate the initial water film thickness. Moreover, for the pores in the shale formation which are open for imbibition, the proposed model can be applied as the small pores are usually filled with initial water.

Chapter 5 A unified model for quasi-continuum water flow under nanoconfined conditions

Although spontaneous imbibition only occurs under hydrophilic conditions, fracturing water can imbibe into hydrophobic nanopores when an external pressure exists. Besides, quasi-continuum water flow under hydrophobic conditions has tremendous applications in chemical engineering and nanotechnology. Therefore, it is important to investigate the quasi-continuum water flow regime under various wettability conditions. MD simulations performed by Sendner showed that on hydrophobic surfaces the water dynamics were purely diffusive, while transient binding or trapping of water occurred for water close to a hydrophilic surface [26]. Accordingly, some research demonstrated that the water near an interface region in the hydrophobic condition diffused faster compared with that in the bulk phase and the viscosity of water in a boundary layer under hydrophilic conditions was higher than in the bulk phase due to stronger interactions with a solid surface [34,36–39,214]. Moreover, the slippage effect cannot be neglected, especially under a hydrophobic condition. In this part, a slip length model based on a quasi-universal relationship between a contact angle and the slip length is applied. The L-W model is modified by combing the effective viscosity model and the slip length model. It is found that the effective viscosity of water is highly affected by a wettability condition, and a linear relationship exists between the contact angle and the interfacial viscosity. The main reason for this phenomenon lies in a different magnitude of the Hamaker constant under various wettability conditions. Besides, it is found that the applied slip length model considers most of the factors that affect the slip length, except for the molecular structure of a solid substrate. Furthermore, how these two factors contribute to the total flow rate under various wettability conditions are analyzed. It is validated that the proposed model can be used to predict the capillary filling behavior.

5.1 Models for slip length

There is much research on the slip behavior for water flow at the nanoscale, and the slip lengths have been estimated both by experiments and MD simulations. However, the reported slip lengths are quite scattered, spanning from several nanometers to tens of micrometers. Many factors affect the magnitude of a slip length, and the experimental measurements under such nanoconfined conditions will be impacted by contaminants and surface roughness. Moreover, reliable theoretical methods to calculate a slip length are still lacking, and most of the approaches rely on Non-Equilibrium Molecular Dynamic (NEMD) simulations or Equilibrium Molecular Dynamic (EMD) simulations. One of the most used methods to calculate a slip length was proposed by Huang et al., who established a theoretical foundation between the slip length and a contact angle based on the Green-Kubo formula [137]:

$$l_s = \frac{C}{(\cos\theta+1)^2} \tag{5.1}$$

where C is a fitting factor and it is found that a curve with C=0.41 fits the MD results very well. Combining the slip length model and the effective viscosity model, the total rate for water flow under nanoconfined conditions can be predicted. A model for fluid transport in a circular tube considering these two effects is given as follows [131]:

$$Q = \frac{\pi}{8\mu_{eff}}\left[\left(\frac{d}{2}\right)^4 + 4\left(\frac{d}{2}\right)^3 l_s\right]\frac{dp}{dl} \tag{5.2}$$

where Q is the total flow rate, μ_{eff} is the effective viscosity, d is the diameter of a tube, and l_s is the slip length.

Accurate estimations of the effective viscosity and the slip length are essential for the prediction of fluid transport at the nanoscale.

5.2 The impact of wettability on the effective viscosity

It is acknowledged that wettability plays a significant role in the effective viscosity. **Figure 5.1** summarizes the data gathered from the literature and those obtained in this work, which shows a

relationship between a contact angle and the local effective viscosity [33,274,294–298]. Here, the local effective viscosity is the viscosity of water under the influence of surface forces. It equals the effective viscosity within the first two layers of water, as this region is highly affected by a solid surface and the liquid-liquid L-J size parameter σ_{LS} is applied. For each type of solid material, there is only one value of the effective viscosity. Although in most experiments and simulations the authors reported a set of effective viscosity values for various channel heights, the local effective viscosity can be calculated by a reduction of the bulk phase viscosity. Moreover, some authors did not measure the contact angles in their experiments or simulations, but these values can be found in other papers in the literature. For example, Babu and Satian performed MD simulations and reported the effective viscosity for water flow in carbon nanotubes. Although the contact angle was not reported in their work, this value has been extensively measured, and a value of 175° was reported [162].

It is found that a nearly linear relationship exists between the local effective viscosity and the contact angle. Increasing the contact angle results in a lower local effective viscosity, which is lower than the bulk phase value under strongly hydrophobic conditions.

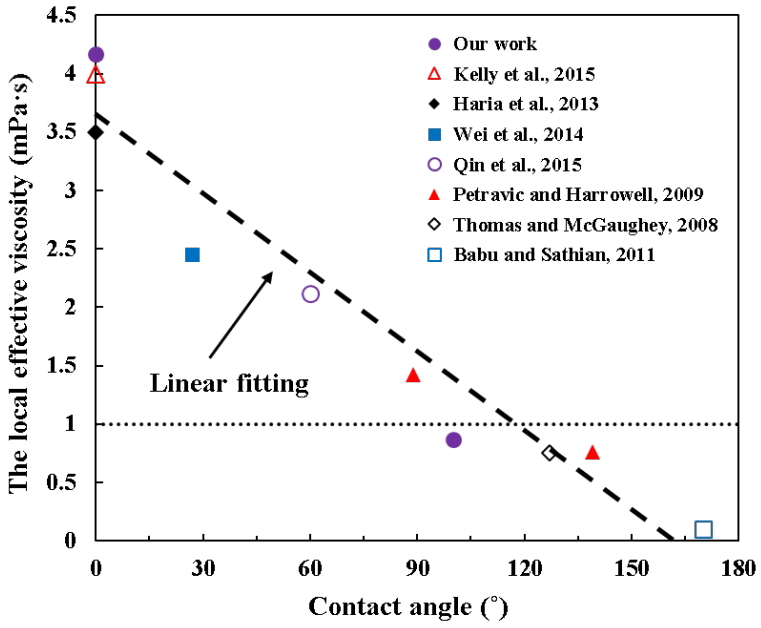

Figure 5. 1 A linear relationship between the contact angle and the local effective viscosity for various water-solid systems.

Moreover, the ratio of the mobility of water in the first two layers close to the solid surface to that of the bulk phase water is shown in **Table 5.1**. The mobility ratio is computed as the reciprocal of the viscosity ratio [129]. For a hydrophilic pore, the mobility in the first water layer is one order of magnitude lower than that of the bulk phase water, while that in the second water layer is only 10 percent lower than that of the bulk phase. Thus, the solid surface exerts a significant impact on the flow properties in the first water layer, while the effect becomes moderate in the second layer. In addition, the mobility of water in the first two layers under the hydrophobic condition exceeds the bulk phase value slightly, indicating that wettability is a major factor on the local effective viscosity.

Table 5. 1 Mobility ratio of water in the first two layers to that of the bulk phase water

	Hydrophilic slit pore	Hydrophilic cylindrical pore	Hydrophobic slit pore	Hydrophobic cylindrical pore
Mobility ratio of the first layer	0.1115	0.1067	1.0289	1.0667
Mobility ratio of the second layer	0.8964	0.8946	1.0095	1.0095

Furthermore, it is known that a hydrophilic condition tends to increase the effective viscosity while an opposite trend can be observed for a hydrophobic pore. Besides, the deviation from the bulk phase viscosity for a hydrophilic pore is much larger compared with a decrease in the effective viscosity for a hydrophobic pore. This trend can be discussed regarding different components of the disjoining pressure which contribute to the effective viscosity. As described in Chapter 4, there are three parts composing the disjoining pressure, including a molecular component, an electrical component, and a structural component. The effective viscosity is determined by $\Delta G_0(l)$-$\Delta G_0(0)$, which represents an additional energy

barrier at a distance *l* due to the influence of surface forces. The additional energy barrier contributed by the three components as a function of the distance of water to a solid surface under both the hydrophilic and hydrophobic conditions is plotted in **Figure 5.2**. Due to the small scale of the additional energy barrier under the hydrophobic condition, the additional energy barriers contributed by the three components are separately plotted. It can be observed that under the hydrophilic condition, the molecular component dominates, and the other two terms are negligible. However, under the hydrophobic condition, the molecular component is significantly reduced, and the hydrophobic repulsive force dominates compared with the van der Waals interactions, leading to parallel orientations of water molecules to the solid surface [68,123]. This altered structure leads to a reduced viscous drag within water near the solid surface, and thus the energy barrier, as well as the viscosity of water, are decreased.

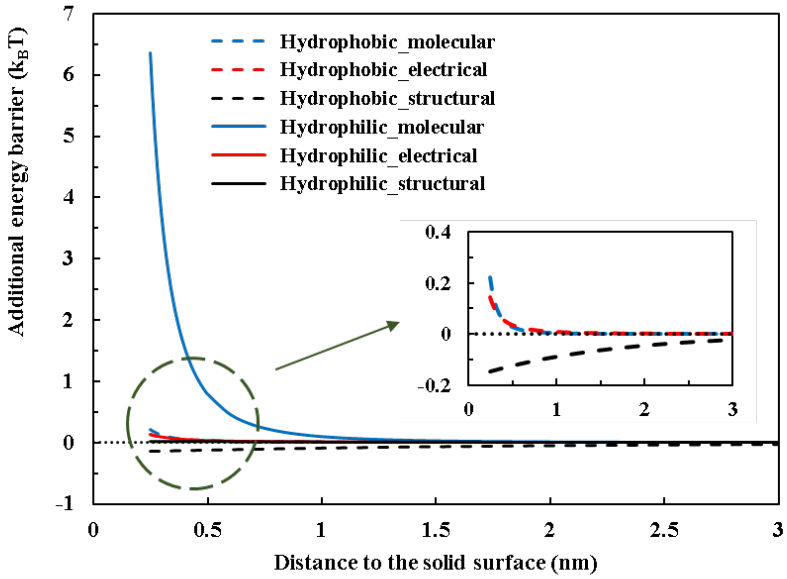

Figure 5. 2 The additional energy barrier contributing from the three components as a function of a channel height for hydrophilic and hydrophobic pores; The inset shows the additional energy barrier at an enlarged scale for hydrophobic pores.

It is, therefore, concluded that the magnitude of the molecular component is crucial to the local effective viscosity for hydrophilic pores, which represents the van der Waals interactions between a solid surface

and water. Despite the difficulty in the determination of a theoretical relationship between the local viscosity and the contact angle, a qualitative argument can be given. The molecular component is determined by the Hamaker constant A_H for a body-body interaction, which can be calculated as [299,300]:

$$A_{\mathrm{H}} = \pi^2 C \rho_1 \rho_2 \tag{5.3}$$

where ρ_1 and ρ_2 represent the number densities of the two interacting particles, and C is a coefficient in the pair interaction which is determined by the L-J interaction energy parameter ε. Moreover, Sinha derived a formulation of the Hamaker constant that is expressed in the form of L-J parameters as follows:

$$A_H = 4\sqrt{2}\pi^2 \frac{\varepsilon \sigma^6 \rho_2}{{R_0}^3} \tag{5.4}$$

where σ is the L-J distance parameter, representing the distance at which the intermolecular potential between the two particles is zero. R_0 is the lattice constant of the solid surface. From this equation, it is known that the increase of both the interaction energy parameter ε and the size parameter σ will lead to a higher Hamaker constant, and thus the local viscosity will be increased.

Furthermore, the impact of the two parameters on the contact angle can be described based on the L-J interaction curves. The interaction between an oxygen atom and a silicon atom is taken as an example. **Figure 5.3** shows the L-J curves between an oxygen atom and a silicon atom for various parameters. The black curve is plotted according to the parameters for an oxygen-silicon pair interaction, the purple one shows the curve based on a 20 percent increase of the size parameter σ, and the red one is that according to a double increase of the interaction energy parameter ε. The green dotted line is guided for comparison. It is illustrated that an increase in the two parameters will lead to a higher L-J potential between the two atoms. Thus, macroscopically, increasing these two L-J parameters can both enhance the interactions between a solid wall and water, resulting in a smaller contact angle. This analysis was verified by Voronov et al., who performed MD simulations and found that the contact angle will monotonically increase with a decrease in both the energy parameter and the size parameter [301]. In their work, the molecular

mechanism underlying the contact angle was explored through dimensionless analysis. The L-J parameters are grouped as follows:

$$\pi_1 = \frac{\varepsilon k_B T \sigma^3 \rho_f}{\varepsilon_{ff}{}^2 m_f} \tag{5.5}$$

where ε_{ff} is the interaction parameter between liquid-liquid molecules. It can be seen that this form is closely related to the Hamaker constant in the form of the L-J parameters, as compared with equation (5.4). They showed that the contact angle is a function of π_1, and the contact angle will decrease monotonically as π_1 increases. Therefore, the contact angle is also controlled by the Hamaker constant, which explains why the local viscosity is correlated with wettability.

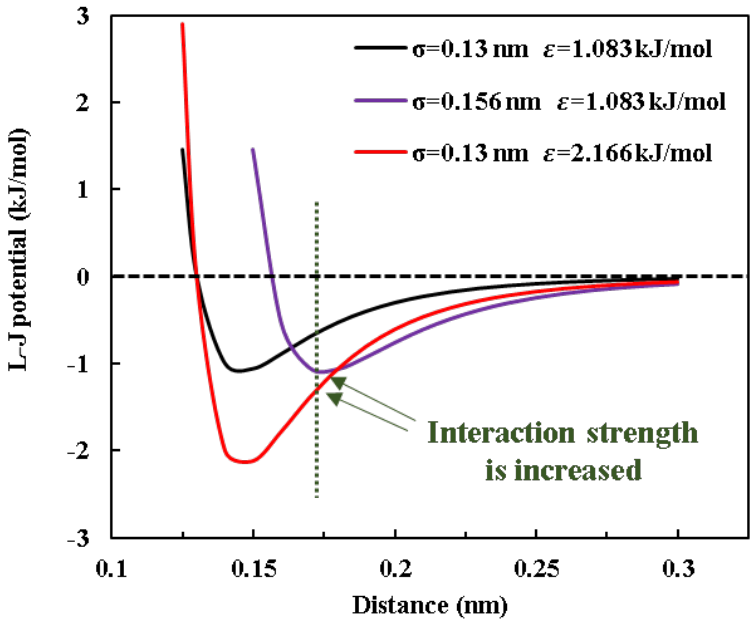

Figure 5. 3 L-J curves between an oxygen atom and a silicon atom for various exclusion diameters and potential well depths.

5.3 Impacting factors on the slip length

A relationship between the wettability condition and the slip length has been widely investigated, while only a few theoretical models have been proposed to predict the slip length. A scaling function between the contact angle and the slip length shown in equation (5.1) is derived based on a Green-Kubo relation, which computes the friction coefficient based on the total lateral forces acting on a surface. Note that this

model only considers the static contact angle and the viscous stress that contributing to the slip behavior, thus a Navier Boundary Condition, rather than a Generalized Navier Boundary Condition, is applied. The latter considers the uncompensated Young stress close to the contact line for the immiscible flow and can be used in all slip boundary conditions [302–305]. Furthermore, it is known that many other factors, such as surface roughness and a size of liquid molecules, also affect the slip length, apart from the contact angle. Thus, the main practicability of this model lies in that it has been verified to be applicable to a wide range of surface characteristics, including various solid densities, roughness, and commensurabilities of solid lattices and liquid molecules. Besides, previous research conducted by Blake also considered a theoretical method to calculate the slip length [129]. The equilibrium contact angle and the mobility of liquid molecules adjacent to a solid surface are related, and the proposed model incorporated the contact angle, the size of liquid molecules, and surface energy.

However, it is noted that the molecular structure of a solid surface is also an important factor that determines the magnitude of the slip length, which is not considered by the previous theoretical models mentioned above [217]. For example, the measured contact angles of a water droplet on a graphene surface and a boron nitride surface are almost the same, and the structures of nanoscale water in contact with graphene and with boron nitride are also very similar [306]. However, the friction coefficient and the slip length are quite different for the flow behavior of water on these two surfaces [307]. This difference is attributed to a greater corrugation of the energy landscape on boron nitride arising from specific electronic structure effects. The slip model in equation (5.1) predicts a slip length of approximately 0.5 nm for water flow on a graphene substrate, as the measured contact angle in the literature is approximately 86˚ to 95˚ [308–312]. This slip length is too conservative, which has been verified by many experiments and MD simulations [164,167–169]. The ultra-smooth structure of a graphene sheet can reduce a viscous drag at a water-graphene interface effectively and lead to an amplified slip length [277,278]. Therefore, it is very difficult to propose a model coupling all the factors that contribute to the slip length.

Moreover, it is noteworthy that in some experiments the measured slip length reached over micrometers. The reason for this exaggerated value has been discussed widely, and the main factors are usually attributed to the possible external dissolved gas and surface roughness. When there is external dissolved gas in water, a large slip length may occur as the nucleation of bubbles will form smooth gas films above which water can flow with small viscous dissipation [155,313,314]. Thus, the flow rate can also be significantly enhanced in this case, regardless of the wettability condition [315]. This phenomenon is usually termed apparent slip. Additionally, it was reported that the degree of slip increased with surface roughness, although an opposite trend was also observed by some scholars [200,316,317].

5.4 Contributions to the flow rate from the two aspects

It is acknowledged that surface forces play significant roles in the quasi-continuum water flow. The impact of surface forces can be discussed in two aspects, as shown in the flow chart in **Figure 5.4**. On one hand, in the tangential direction of water flow, a friction force at a liquid-solid interface is determined by the solid surface. This interfacial friction determines the dynamics of the slip plane, which is associated with the slip length. On the other hand, in the normal direction, there is induced disjoining pressure near the solid surface. The inhomogeneity of the pressure will result in the spatially varying viscosity, which deforms a velocity profile. The average cross-section velocity profile will deviate from a parabolic shape. For a Poiseuille flow type, these two aspects lead to the deviations of the flow rate from that predicted by a traditional Hagen-Poiseuille equation with constant viscosity and a no-slip boundary condition.

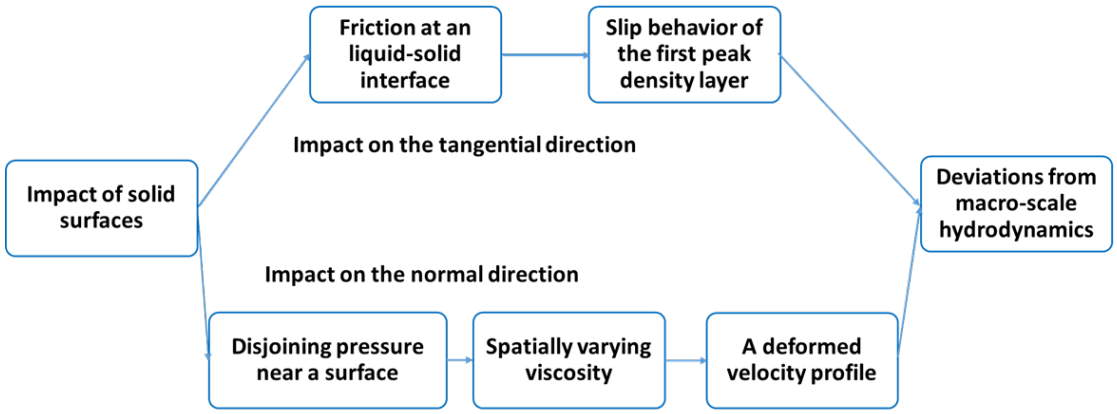

Figure 5. 4 The impact of surface forces on flow properties from two aspects at the nanoscale.

Moreover, the contributions from the two aspects are various under different wettability conditions. The flow rates for water flow within a slit nanopore under different wettability conditions are calculated by using equation (5.2). The channel height is chosen as 5 nm, and the applied pressure gradient is 10^{14} Pa/m. Equation (5.1) is used to relate the contact angle and the slip length. Besides, a linear relationship between the local effective viscosity and the contact angle is used for calculation. This relationship is shown in **Figure 5.1**, which is obtained as follows:

$$\mu_{le} = -0.0225\theta + 3.6182 \tag{5.6}$$

where μ_{le} represents the local effective viscosity. The results are displayed in **Figure 5.5**. The four lines in this figure represent the flow rate with a slip length, the flow rate with an effective viscosity, the flow rate with both factors, and the flow rate predicted by a traditional Hagen-Poiseuille equation, respectively. By comparing the flow rate only with a slip boundary condition and that coupling both aspects, it is found that the effective viscosity tends to increase the flow resistance when the contact angle is low, while it reduces the viscous drag when the contact angle is very high. Besides, the slip behavior always contributes to a higher flow rate, as the flow rate with the slip boundary condition is always larger than that predicted by the traditional Hagen-Poiseuille equation. The flow rate under a strongly hydrophobic condition can

be several orders of magnitude higher than that predicted by the traditional Hagen-Poiseuille equation due to a large slip length. Moreover, it can be concluded that under the hydrophilic condition, both the effective viscosity and the slip length have non-negligible effects on the total flow rate, as shown in the inset. However, the slip behavior becomes a dominant factor under a strongly hydrophobic condition.

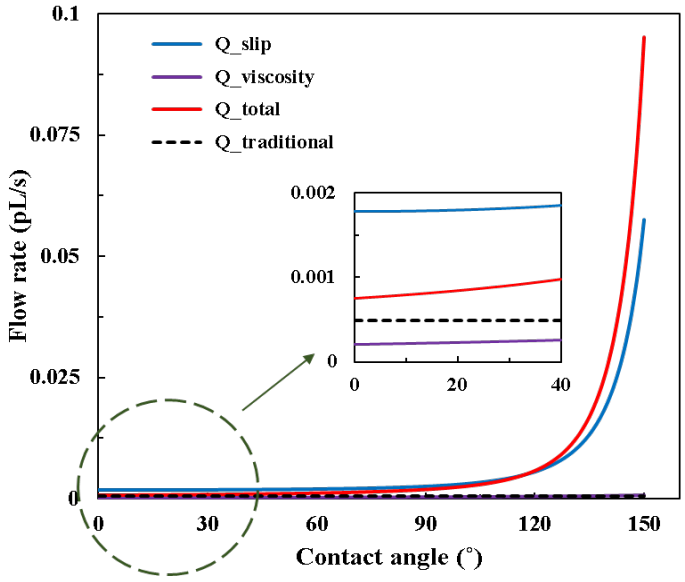

Figure 5. 5 The flow rate through a slit nanopore with a channel height of 5 nm under different wettability conditions; The inset shows the flow rate under strong hydrophilic conditions at an enlarged scale

5.5 Applications in chemical engineering – Capillary filling process

Capillarity effects play an essential role in many different fields of science and engineering, including nanotechnology, physical chemistry, and chemical engineering. Applications of capillary filling are prevalent in the chemical engineering field [318–321]. For liquid flow under nanoconfined conditions, the effective viscosity and slip behavior are incorporated into the L-W model. The modified models for a nanocapillary and a nanoslit accounting for these two effects are given as follows [322]:

$$L(t) = \left[\frac{D\gamma\cos\theta\left(1+\frac{8l_s}{D}\right)}{4\mu_{eff}(D)}\right]^{\frac{1}{2}} t^{\frac{1}{2}} \tag{5.7}$$

$$L(t) = \left[\frac{H\gamma\cos\theta\left(1+\frac{6l_s}{H}\right)}{3\mu_{eff}(H)}\right]^{\frac{1}{2}} t^{\frac{1}{2}} \tag{5.8}$$

where L is the imbibition length and t is time.

The proposed effective viscosity model and the slip model are inserted into the classic L-W model, and the results are compared with those obtained from the experiments conducted by Oh et al. [323]. In **Figure 5.6**, the imbibition length as a function of time calculated by the model is exhibited and the results obtained from experiments are compared. The model fits very well with the experimental results, thus validating the reliability of the model. Moreover, the predictions of the imbibition length by the classical L-W model by only considering the effective viscosity and by only accounting for the slip length are also displayed in this figure. For such a capillary filling process, the deviation from the results will be huge if the effective viscosity effect is neglected. However, the slippage effect only has a slight effect on the imbibition length compared with the effective viscosity. This arises from that under such a strongly hydrophilic condition, the effective viscosity for a slit pore with a channel height of 6 nm is obvious, while the slip length is less than 1 nanometer. Thus, in this case, the effective viscosity is the dominant factor for a capillary filling process, and the flow rate is highly affected by a velocity profile.

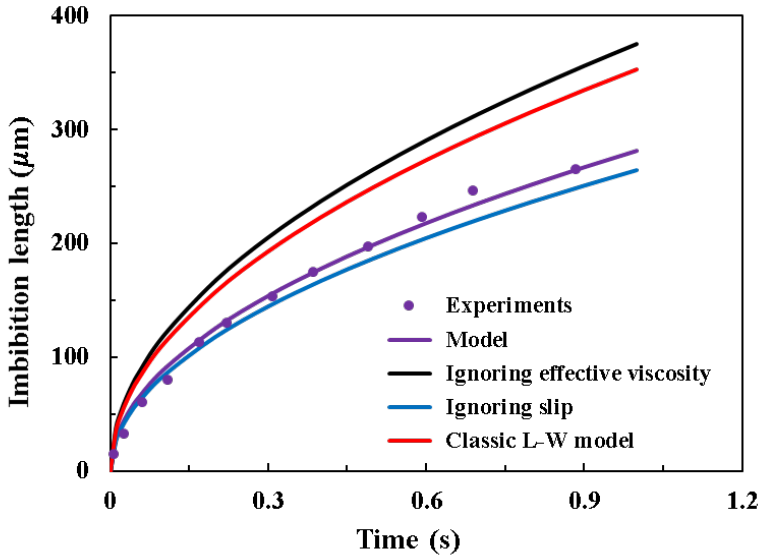

Figure 5. 6 The imbibition length predicted by the proposed model, by the classic L-W model, by the model that ignores the effective viscosity, by the model that ignores slip behavior, and that obtained from experiments

5.6 Summary

In this part, the quasi-continuum water flow behavior under nanoconfined conditions is investigated, and its applications in the chemical engineering field are discussed. It is found that the effective viscosity of water is highly affected by a wettability condition, and a linear relationship exists between the contact angle and the interfacial viscosity. A strongly hydrophilic surface tends to increase the effective viscosity dramatically, while a small decrease in the effective viscosity can be observed under a hydrophobic condition. This is mainly due to the different magnitudes of the Hamaker constant under various wettability conditions. Moreover, it is found that the applied slip length model considers most of the factors that affect the slip length, except for a molecular structure of a solid substrate. The reason for the scattered slip lengths reported in the literature has also been discussed.

The deviations of a flow rate from the prediction by the traditional Hagen-Poiseuille equation contributed by the effective viscosity and the slip length are analyzed. It is found that under strongly hydrophilic conditions, both factors are nonnegligible for the total flow rate, while the slip behavior becomes a dominant factor when the contact angle reaches over 100˚. In addition, an application of the above theories to a capillary filling process in the chemical engineering field has been discussed.

Chapter 6 The spreading of the precursor films

Recently, a research topic that draws increasingly wide attention is the fluid imbibition behavior in nanopores with the existence of precursor films. The precursor film propagation is a prevalent phenomenon during a wetting process, and the dynamic imbibition behavior with the precursor films has extensive applications in nanotechnology and chemical engineering [237]. For example, the performance of the external wetting of porous solids plays a key role in widely employed trickle bed reactors, which is associated with a lubrication approximation for thin film flow on an external surface [238]. The thin films propagating ahead of the main meniscus may manage to hide the chemical and geometrical details of the nano-channel walls, thereby exerting a major influence on the efficiency of nano-channel–coating strategies [139,239]. It is well known that the film dynamics can significantly affect an imbibition process in a nanoconfined system [214]. However, much of the research in this area was performed in the context of a droplet spreading process, with a focus only on the dynamics of a film itself. The impact of precursor films on a capillary filling process was usually ignored, and to the best of our knowledge, there is no theoretical model available for the dynamic imbibition process at the nanoscale considering the precursor films in the literature.

To investigate this research topic, an approach is to quit the continuum level and turn directly to the atomistic description of fluid flows as a collection of moving molecules. This is computationally demanding, which prevents the attainment of space and time macroscopic scales of experimental interest. In this part, the capillary dynamics of confined water in nanopores under a quasi-continuum flow regime is investigated, considering precursor films ahead of a main meniscus. A model for the imbibition behavior in nanopores is proposed, which takes the propagation of the precursor films into account. In addition, the increased viscosity of water near a solid wall and dynamic contact angle are incorporated in the proposed model. Experimental results are used to validate the model. It is found that the increased viscosity for

water near a solid surface significantly reduces the fluidity, and the fluid loss from the surface water into the precursor films plays a key role in the imbibition behavior. Ignoring this effect will highly overestimate the true imbibition length. For a nano-channel with a width of 5 nm, the predicted imbibition length without the consideration of the fluid loss will almost be double of the true imbibition length. Moreover, this deviation becomes smaller with the increase of the pore size. Furthermore, the dynamic contact angle has a minimal effect on the imbibition length, which indicates an improvement of nano-channel-coating efficiency by the propagation of the precursor films. The proposed model captures important physics for capillary dynamics at the nanoscale and has wide applications in many fields.

6.1 Model establishment

6.1.1 Water imbibition with precursor films

The water imbibition behavior in nanopores has been extensively investigated. However, most of these investigations have not considered precursor films and treated a flow region as a whole part. As introduced in Chapter 2, the dynamics of films is different from that of the bulk phase water, and thus the previous treatment has huge deficiencies. Moreover, this assumption cannot explain a paradox that precursor films propagate faster than the bulk phase while the viscosity of water in the films is much higher due to its strong interactions with a solid surface. Therefore, a model that captures the unique physics of precursor films in nanopores is required for a spontaneous imbibition process.

A spontaneous imbibition process with the existence of precursor films for water in a nanopore is shown in **Figure 6.1**. There are four parts in a flow region, whose middle is the bulk phase water and surface water. The viscosity of water in the middle of the flow region is not affected by a solid surface, and water beyond this region has a changed viscosity due to its interactions with the solid surface. Under strongly hydrophilic conditions, the viscosity of water close to the solid surface will be very high, and thus the water in this region is termed solidified water. Moreover, the surface water has higher mobility due to its contact with the vapor phase and will diffuse into the precursor films driven by the spreading force of the

solid surface. The energy of water in the precursor films acquired from the spreading power will be dissipated rapidly when they are pinned to the solid surface due to strong water-wall interactions, and thus they are transformed into the solidified layers. Moreover, as introduced in Chapter 2, the spreading power will be entirely dissipated in the films, and thus the water in the middle of the flow region is only driven by the capillary force arising from the liquid-vapor interfacial tension. Therefore, it can be anticipated that the water in the middle of the flow region behaves like a classical capillary filling process, which can be described by the macroscopic hydrodynamics. This flow region is defined as the macroscopic region, including the bulk phase water and the surface water. It should be noted that the thickness of the surface water is very thin, approximately one or two water layers, and thus it is impossible to differentiate the surface water from the bulk phase water. In other words, there only exists one meniscus at a certain time, composed of surface water molecules.

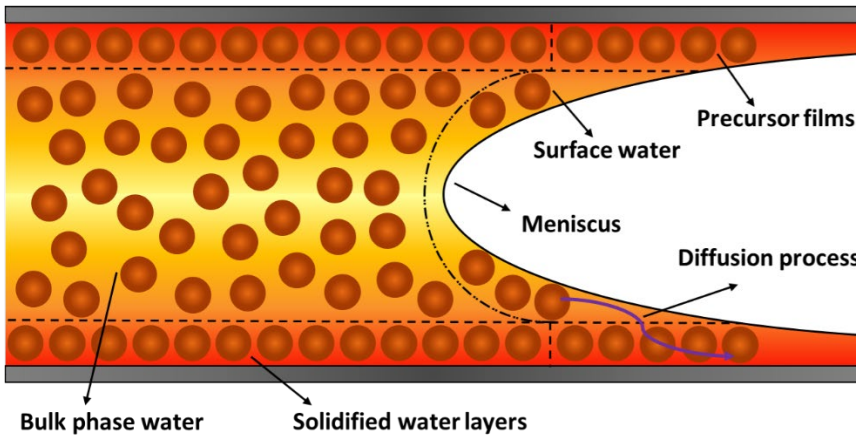

Figure 6. 1 A spontaneous imbibition process with precursor films for water in a nanopore

In **Figure 6.2 (a)**, a schematic of the imbibition length is illustrated. The bulk phase and the surface water are in the middle while the solidified layers and precursor films are attached to the solid surfaces. As mentioned in Chapter 2, the solidified water layers and the precursor films are from the surface water in the middle of the flow region due to diffusion. It can be imagined that the water in the solidified layers and the precursor films moves to the bulk phase, and an imaginary imbibition length L can be obtained,

as shown in **Figure 6.2 (b)**. Since the motion of the bulk phase water is a classical capillary filling process driven only by the capillary pressure, the total mass uptake during the spontaneous imbibition process is equivalent to the mass uptake of water in a nano-capillary with a radius of R'. Therefore, the imaginary imbibition length L can be computed by using the classical L-W model.

Moreover, the main feature characterizing a dynamic capillary filling process is the dynamic contact angle, which deviates from its equilibrium value due to the energy dissipation in a TPCL [324]. Therefore, the macroscopic region of water can be modeled by using the modified L-W model for a nano-capillary:

$$L\frac{dL}{dt} = \frac{\sigma_{lg}\cos\theta_t R'}{4\mu_b} \tag{6.1}$$

where R' is the radius of the macroscopic region in the capillary tube and θ_t is the dynamic contact angle. The model for a nano-channel is given by

$$L\frac{dL}{dt} = \frac{\sigma_{lg}\cos\theta_t H'}{6\mu_b} \tag{6.2}$$

where H' is the height of the macroscopic region in the channel.

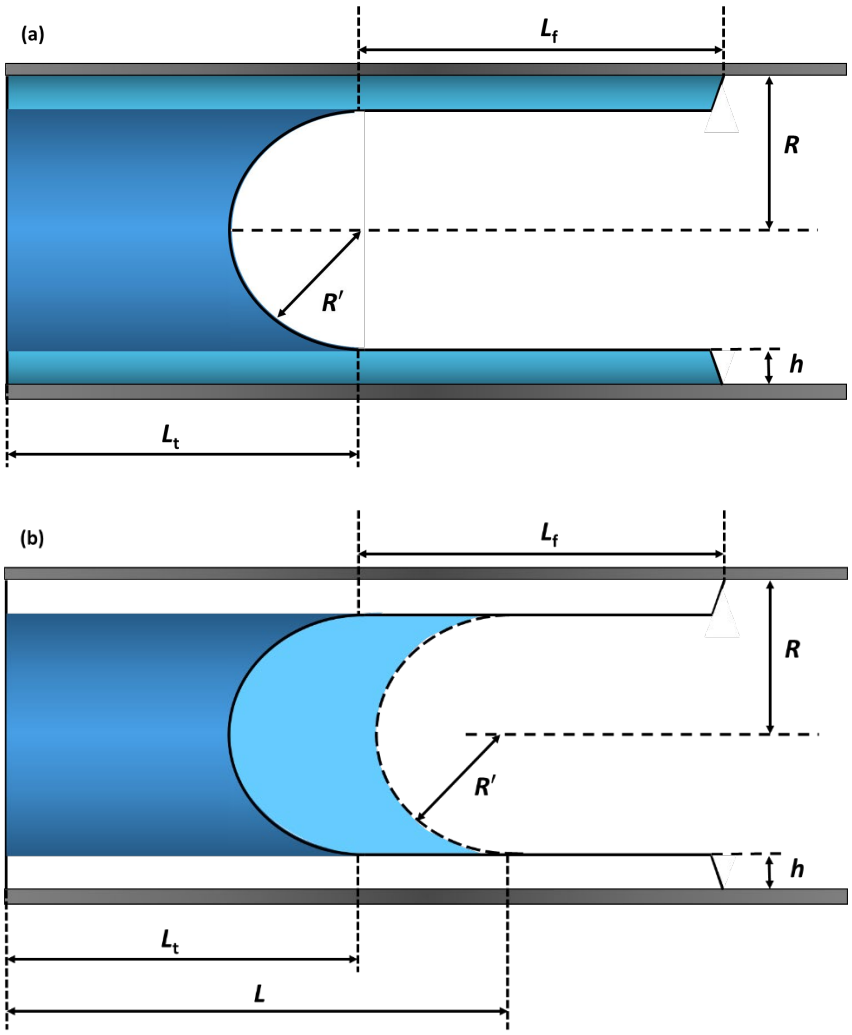

Figure 6. 2 (a) The schematic of the meniscus and films; (b) the equivalent imbibition length *L* excluding the impact of the precursor films

After the calculation of the imaginary imbibition length L, the fluid loss into the solidified layers and the precursor films should be quantified to obtain the true imbibition length L_t, which represents the penetration of the macroscopic region. Additionally, the radius (height) of the macroscopic region in the flow region in the capillary (channel) should be determined, and a relationship between the dynamic angle and the imbibition speed should be established.

6.1.2 The relationship between the imbibition speed and the contact angle

It is acknowledged that the dynamic contact angle is correlated with the velocity of the macroscopic region [227], and the motion of a TPCL is driven by the unbalanced surface tension. From the view of the molecular kinetic theory, the velocity of the TPCL is given by [325,326]

$$V = 2\kappa^0 \lambda \sinh[\frac{\sigma_{lg}\lambda^2(\cos\theta_e - \cos\theta_t)}{2k_bT}] \tag{6.3}$$

where κ^0 is the rate of the hopping process, λ is the jump length of a molecule, θ_e is the equilibrium contact angle, k_b is the Boltzmann constant, and T is temperature. κ^0 is computed by

$$\kappa^0 = \frac{k_bT}{\mu_b v_m}\exp[-\frac{\lambda^2\sigma_{lg}(1+\cos\theta_e)}{k_bT}] \tag{6.4}$$

where v_m is the molar volume. Usually, $\lambda^2\sigma_{lg}(1+\cos\theta_e)$ is much smaller than k_bT, and the part in the brackets in equation (6.3) is much smaller than 1. Thus, equation (6.3) can be linearized as

$$V = \frac{\kappa^0\sigma_{lg}\lambda^3(\cos\theta_e - \cos\theta_t)}{k_bT} \tag{6.5}$$

Therefore, the relationship between the dynamic angle and the imbibition speed can be established as

$$\sigma_{lg}(\cos\theta_e - \cos\theta_t) = \zeta\frac{dL}{dt} \tag{6.6}$$

$$\zeta = \frac{v_m\mu_b}{\lambda^3}\exp[\frac{\lambda^2\sigma_{lg}(1+\cos\theta_e)}{k_bT}] \tag{6.7}$$

Inserting equation (6.6) into equations (6.1) and (6.2), the imbibition length without water loss L can be computed as

$$2\mu_b L^2 + \zeta R' L = \sigma_{lg} R' \cos\theta_e\, t \tag{6.8}$$

$$3\mu_b L^2 + \zeta H' L = \sigma_{lg} H' \cos\theta_e\, t \tag{6.9}$$

Thus, it can be seen that the imbibition length without water loss L and time t follows a parabolic relationship.

6.1.3 The thickness of solidified water layers

It is acknowledged that the viscosity of water close to a solid surface is greatly changed. In a completely wetting case, it is mentioned in Chapter 4 that the mobility of the first two layers close to the solid surface is significantly reduced, and thus the film thickness is regarded to be the sum of the thickness of two water layers and the void layer between water molecules and the solid surface, which is approximately 0.65 nm [327]. Some spontaneous imbibition experiments at the nanoscale under completely wetting conditions also showed that there are two solidified water layers attached to a solid surface [219,221], which are consistent with these calculations.

6.1.4 The true imbibition length

As seen in **Figure 6.1**, the water lost in the macroscopic region flows into the solidified layers and films, and thus the true imbibition length can be computed by:

$$L_t = L - (L_t + L_f)\frac{A_f \rho_f}{A_m \rho_b} \tag{6.10}$$

where L_f is the length of the precursor film ahead of the meniscus, ρ_b is the bulk phase density, ρ_f is the density of the solidified water layers and the precursor films, A_f is the cross-section area of the precursor film, and A_m is the cross-section area of the macroscopic region. For a nano-capillary, this equation is given by:

$$L_t = \frac{LR'^2\rho_b - L_f(R^2 - R'^2)\rho_f}{R'^2\rho_b + (R^2 - R'^2)\rho_f} \tag{6.11}$$

For a nano-channel, the equation for the true imbibition length becomes:

$$L_t = \frac{LH'\rho_b - L_f(H - H')\rho_f}{H'\rho_b + (H - H')\rho_f} \tag{6.12}$$

A reliable prediction of L_f plays a key role in the quantification of the true imbibition length. As introduced in Chapter 2, the film length increases very slowly before it reaches a microscale. Thus, equation (2.7) is used to predict the length of a precursor film. In equation (2.7), the velocity of a TPCL can be computed by equations (6.1) and (6.2) for a nano-capillary and nano-channel, respectively:

$$V = \frac{dL}{dt} = \frac{\sigma_{lg} R' cos\theta_e}{4\mu_b L + \zeta R'} \tag{6.13}$$

$$V = \frac{dL}{dt} = \frac{\sigma_{lg} H' cos\theta_e}{6\mu_b L + \zeta H'} \tag{6.14}$$

Therefore, the length of the precursor film can be computed by:

$$L_f = \sqrt{\frac{A_H S}{\mu_b{}^2 (\frac{\sigma_{lg} R' cos\theta_e}{4\mu_b L + \zeta R'})^2}} \tag{6.15}$$

$$L_f = \sqrt{\frac{A_H S}{\mu_b{}^2 (\frac{\sigma_{lg} H' cos\theta_e}{6\mu_b L + \zeta H'})^2}} \tag{6.16}$$

As one of the most important preconditions of equation (2.7) is that the imbibition velocity is very slow, it can be seen that the length of a precursor film increases very steadily. After the calculation of the length of the precursor film, the imbibition length can be obtained by equations (6.11) and (6.12) for a nano-capillary and a nano-channel, respectively.

6.2 Model validation

In order to check the validity of the proposed model, the results predicted by the model are compared with the published experimental and simulation data [219,221]. The calculation parameters are listed in **Table 6. 1**.

Table 6. 1 Parameters used in the calculation

Parameter	Symbol	Unit	Value	Reference value
Temperature	T	K	298	
Liquid-vapor interfacial tension	σ_{lg}	N/m	0.072	
The viscosity of the bulk phase water	μ_b	Pa·s	0.001	
Length per hop	λ	nm	0.3	0.3 [129]
Equilibrium contact angle	θ_e	Dimensionless	0	0 [219,221]
Boltzmann constant	k_b	J/K	1.38×10^{-23}	
Molar volume	v_m	nm^3	2.99×10^{-2}	

Bulk phase density	ρ_b	kg/m^3	1	
The density of the solidified water layers and the precursor films	ρ_f	kg/m^3	1.15	1.15 [36]
Fluid/solid Hamaker constant	A_H	J	8.6×10^{-20}	$6.94\sim8.6\times10^{-20}$ [328]
The relative permittivity of media	ε_r	Dimensionless	81.5	81.5
Permittivity in vacuum	ε_0	F/m	8.85×10^{-12}	8.85×10^{-12}
The difference between the electric potentials of two interfaces	$\Delta\zeta$	V	0.05	0.05~0.07 [329,330]
Reciprocal of the Debye length	κ	nm^{-1}	1	1 [68,123]

6.2.1 Validation of the proposed model by capillary filling experiments

Experimental results are used to validate the proposed model at first. Haneveld et al. fabricated silicon-based nanochannels with channel heights ranging from 5 nm to 47 nm, based on the use of a thin thermal silicon oxide spacer layer. For all channel heights, the filling kinetics were recorded and compared with the bulk phase behavior. **Figure 6.3** shows the true imbibition length calculated by the proposed model and that obtained from their experiments. [221]. It is obvious that in all cases with different channel heights, the results calculated by the proposed model match very well with the experimental observations, and thus the model can reliably predict the true imbibition length in a single nano-channel.

Moreover, the results obtained from the model are compared with spontaneous imbibition experiments for water uptake in three-dimensional networks of hydrophilic silica pores. The experiments were conducted by Gruener et al. [219]. They chose a Vycor glass as a porous host, which was a virtually pure fused silica glass permeated by a three-dimensional network of interconnected tortuous pores[219][219][219][219][219][219][218][219][219][218][227]. For such a network, the total mass uptake per unit area including geometric factors are given by:

$$m = L_t \rho \frac{\phi}{\tau} \tag{6.17}$$

where m is the total mass uptake per unit area by the network, ϕ is porosity, and τ is tortuosity. **Figure 6.4** shows the results obtained from the model and experiments. It can be seen that the model predicts the true imbibition length correctly. Furthermore, the imbibition length predicted by the classical L-W model is illustrated. The classical L-W model will significantly overestimate the true imbibition length, and thus the modifications are required.

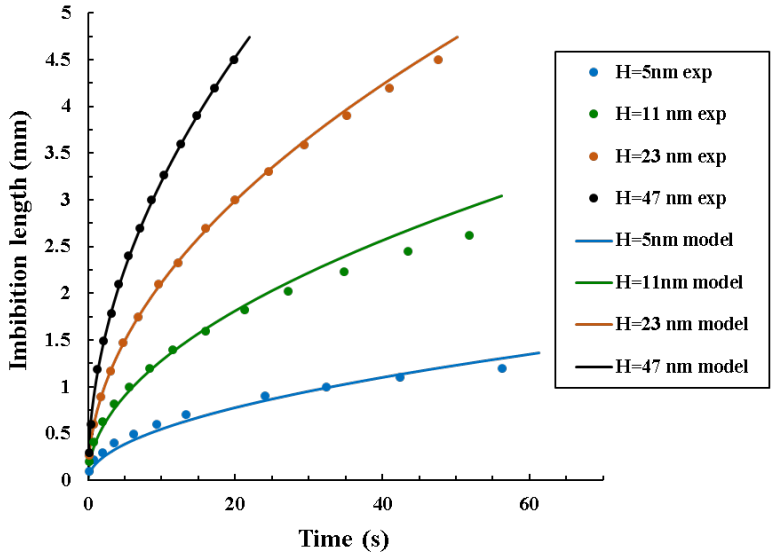

Figure 6. 3 The true imbibition lengths from the model and experiments for nano-channels

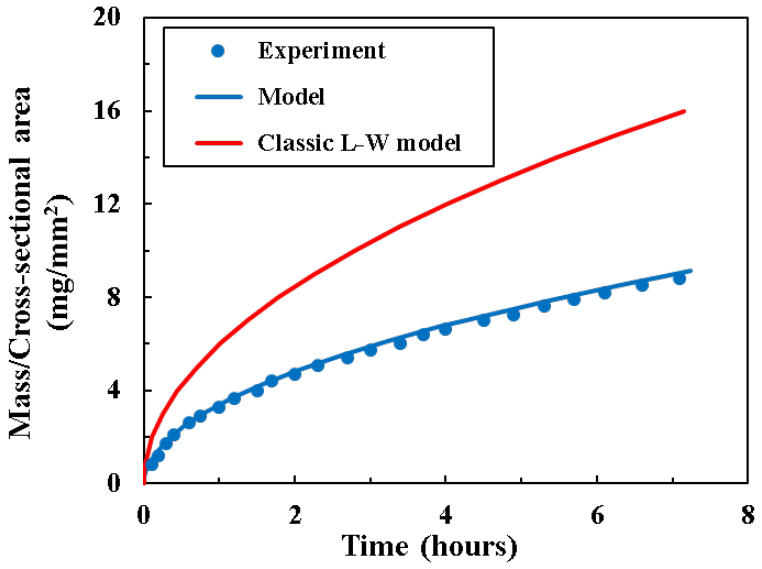

Figure 6. 4 The true imbibition lengths from the model and experiments for a three-dimensional network

It can be seen that the same experimental results are used for the validation of the proposed effective viscosity model in Chapter 4 and the proposed imbibition model in this Chapter. In Chapter 4, the modified effective viscosity model is inserted into the traditional L-W model. The precursor film ahead of the main meniscus is not considered, and the flow region is regarded as a whole part, including the bulk phase and the solidified layers. However, this treatment is simplified, and it can be seen that the results predicted by the model are not very accurate for small channels. Apart from the reasons mentioned in Chapter 4, ignoring the precursor films is another factor for the small deviations. The proposed imbibition model in this Chapter, however, captures the physics of the precursor films and gives a better match with the imbibition results. Therefore, the proposed model in this Chapter is more accurate.

6.2.2 Validation of the proposed model by simulations

In addition to the experimental results, simulation data is also used to verify the proposed model. Chibbaro et al. applied hydrokinetic Lattice Boltzmann (LB) and MD simulations of capillary filling of highly wetting fluids in nano-channels, which provided clear evidence of the formation of thin precursor films ahead of the main meniscus [331]. The imbibition behavior of the main meniscus predicted by the proposed model and their presented results are compared, as shown in **Figure 6.5**. The vertical axis is the square of the imbibition length, and the horizontal axis represents the time. The results are presented in reduced capillary units. The gray dashed line represents the classic L-W model with no modifications, and thus it has a unit slope. It can be seen that this line cannot match the LB and MD data. The authors obtained a better fit by moving this line vertically, as shown by the red dashed line. However, this fit has no clear physical meaning. The fitted line doesn't start from the origin of the coordinate axis, which is unrealistic. Besides, the uniqueness of the imbibition behavior at the nanoscale is not captured, as there are no modifications to the classic L-W model. However, this model can predict the imbibition behavior more

precisely, as shown in the black solid line. It can be seen that this line can fit the LB and MD data very well, and thus the proposed model is further validated.

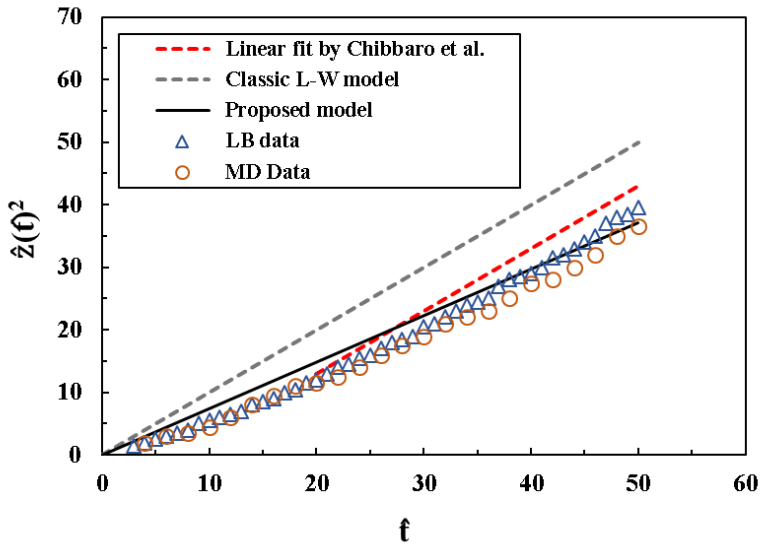

Figure 6. 5 The true imbibition length predicted by the proposed model and by the MD and LB simulations

To sum up, three different ways are used to validate the proposed model. The first one is the capillary filling experiment in single capillary channels, the second one is the capillary filling experiment in a porous media composed of capillary tubes, and the last one is the LB and MD simulations. Therefore, the proposed model is reliable and can be widely applied.

6.3 Results and discussion

6.3.1 The dynamics of a meniscus

For spontaneous imbibition of water in nano-channels, the edge of a meniscus in a macroscopic region is driven by the unbalanced surface tension. The dynamic contact angle changes continuously, which is related to the meniscus velocity. In **Figure 6.6**, the change in the dynamic contact angle with time for nano-channels is shown. The contact angle reduces rapidly at first and then decreases steadily towards the equilibrium one. It is noted that the deviations of the dynamic contact angles from the equilibrium ones

are always less than 1˚ in all cases. This result indicates that the dynamic wetting process has a minimal effect on the imbibition length under the completely wetting case.

It is acknowledged that the dynamic contact angle arises from the surface roughness and chemical heterogeneity. The main reason for a negligible change in the dynamic contact angle lies in the fact that the effect of a solid surface on a meniscus can be neglected. This can be addressed in two aspects; the first one is that the spreading power due to the solid surface is completely dissipated in the solidified water layers and the precursor films, and thus the only driving force for the motion of the meniscus is the liquid-vapor surface tension. The other one is that the viscosity of the water in the macroscopic region reaches the bulk phase value, so the dynamics of the meniscus is not affected by the solid surface and the meniscus behaves like a classical capillary filling process. As the macroscopic water slides above the solidified water layers and is slightly or not affected by the solid surface, the dynamic angle will approach the equilibrium contact angle under Young's condition.

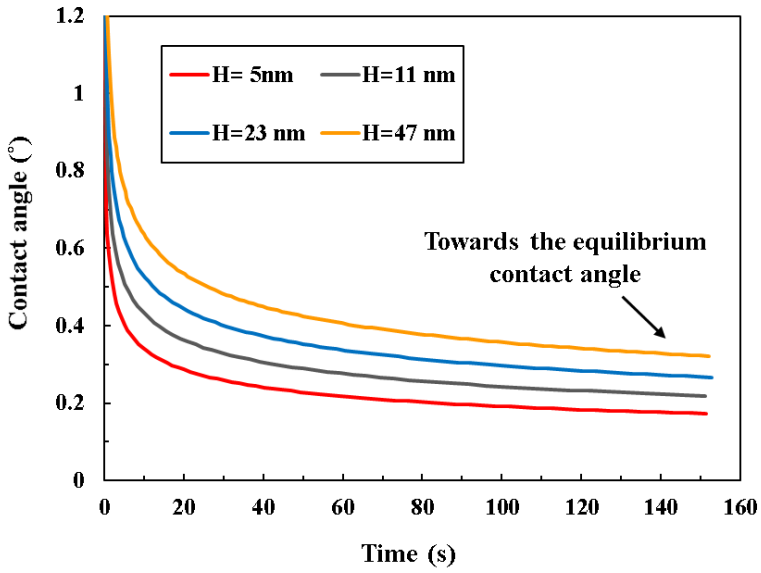

Figure 6. 6 The change in the dynamic contact angle for nano-channels

Moreover, it is noted that a meniscus is close to a semicircle. Normally, the curvature on the meniscus is not constant when a film coexists with the meniscus, due to the impact of adsorptive surface forces on the region close to the solid surface. As introduced in Chapter 2, a liquid-vapor interface is considered as a

surface of constant partial specific Gibbs free energy, composing of a capillary component and an adsorptive component. The bulk phase is only controlled by the capillary force arising from the liquid-vapor surface tension, and the film is dominated by the adsorptive forces induced by the solid surface [332]. The former one has a constant curvature while the curvature of the latter is infinite. Between the bulk phase region and the film region, a transition zone exists, which is controlled by both the capillary component and the adsorption component [333,334]. The curvature on any point of the meniscus in this region is different. A schematic is shown in **Figure 6.7**. In a completely wetting case in this study, the motion of the meniscus is considered to be driven only by the capillary force, as the spreading power of a dry surface is totally dissipated in the precursor films. Therefore, it is supposed that the transition zone is much smaller than that in the partially wetting case.

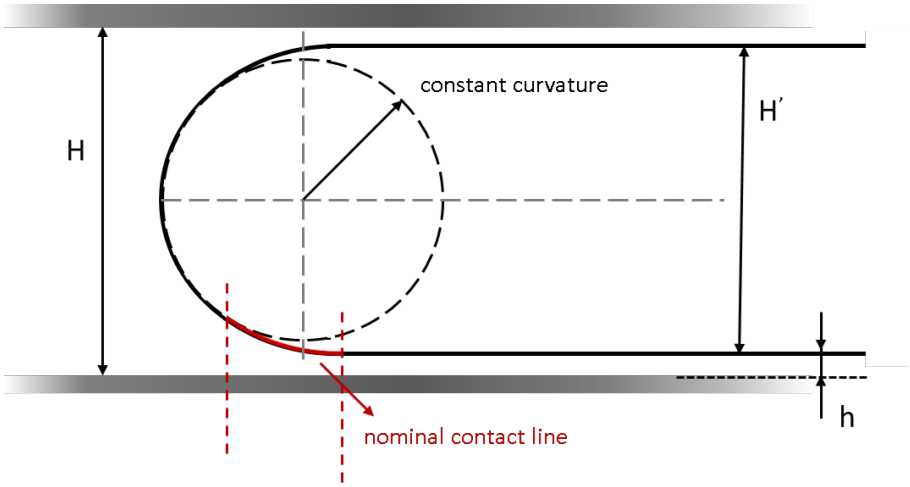

Figure 6. 7 The transition region between a meniscus and a precursor film

Additionally, it is found that the water in the transition region behaves like bulk water during the wetting process, and it will not diffuse out of this region and flow into the precursor films [252]. Thus, the nominal contact line in **Figure 6.7** represents the transition region when the meniscus and the precursor films coexist under the equilibrium condition, which is not associated with the surface water. The surface water indicates the source of the propagating precursor films. During a dynamic process, the surface water will diffuse above the nominal contact line, flow into the films, and get quick damping once pinned by the

solid surface. In many experiments, the terraced layering of the precursor films close to the nominal contact line was observed, due to that the surface water cannot be transferred into a precursor film instantly [335–337]. A schematic of the terraced layering phenomenon is illustrated in **Figure 6.8**.

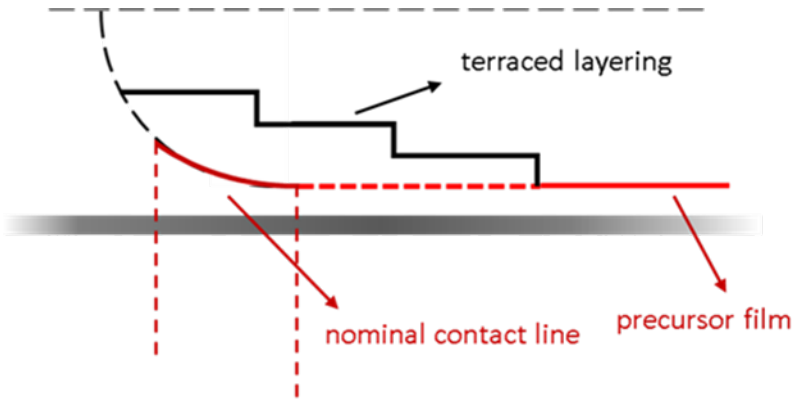

Figure 6. 8 The terraced layering water above a nominal contact line

6.3.2 The effects of precursor films

For water imbibition in nanopores, the imbibition speed becomes slower and slower with time, and the imbibition length increases slowly. Theoretically, the length of a precursor film also increases steadily; however, a change in the film length is usually negligible in the time scale during experiments. Thus, it can be regarded as a constant, and the precursor films in this stage are usually termed adiabatic films [245]. Moreover, some experiments found that when a film is sufficiently long ahead of a meniscus, the film flattens as it spreads. This is because the leading edge is far from the meniscus, and water cannot be supplemented from the meniscus instantly. Thus, the film will become self-diffused. This phenomenon is more prevalent for droplet spreading at the mesoscale, where the film thickness is in the range of 3~1000 nm. In this case, the film thickness will not be constant, and there is a gradient of the disjoining pressure along the film, acting as a driving force for the self-diffusion of the precursor film [259,338]. In this study, a constant film thickness is assumed, since the focus of this work is the true imbibition length of the main meniscus. Therefore, the terraced layering of water close to the meniscus and the diffusive film due to the disjoining pressure gradient are not investigated.

Furthermore, the imbibition length L without fluid loss and that calculated by the classical L-W model for nano-channels are compared, as shown in **Figure 6.9 (a)** and **(b)**. The length calculated by the classical L-W model ignores the increased viscosity effect near a solid surface and the precursor films ahead of the main meniscus. It is shown that the classical L-W model significantly overestimates the imbibition length, and the deviation is much more obvious for channels with small channel heights. This is mainly because the classical L-W model ignores the reduced mobility of the water molecules near the solid surface. When the channel height is very small, the region of water molecules with reduced mobility will account for a large part of the total flow region, and thus the deviation will become significant. Additionally, the imbibition length L also highly deviates from the true imbibition length, as the fluid diffusion into the films is neglected. This deviation proves that the precursor films come from the macroscopic part of the flow region; otherwise, the imbibition length L will match the experimental results, instead of the true imbibition length L_t. The viscosity of water close to a solid surface is much higher than that of the bulk phase value, and thus the fast propagation of the precursor films ahead of the meniscus cannot arise from the slip behavior of water molecules within the increased viscosity region near the solid surface. The continuous and fast diffusion of the surface water in the macroscopic region into the precursor films is the only explanation for this issue.

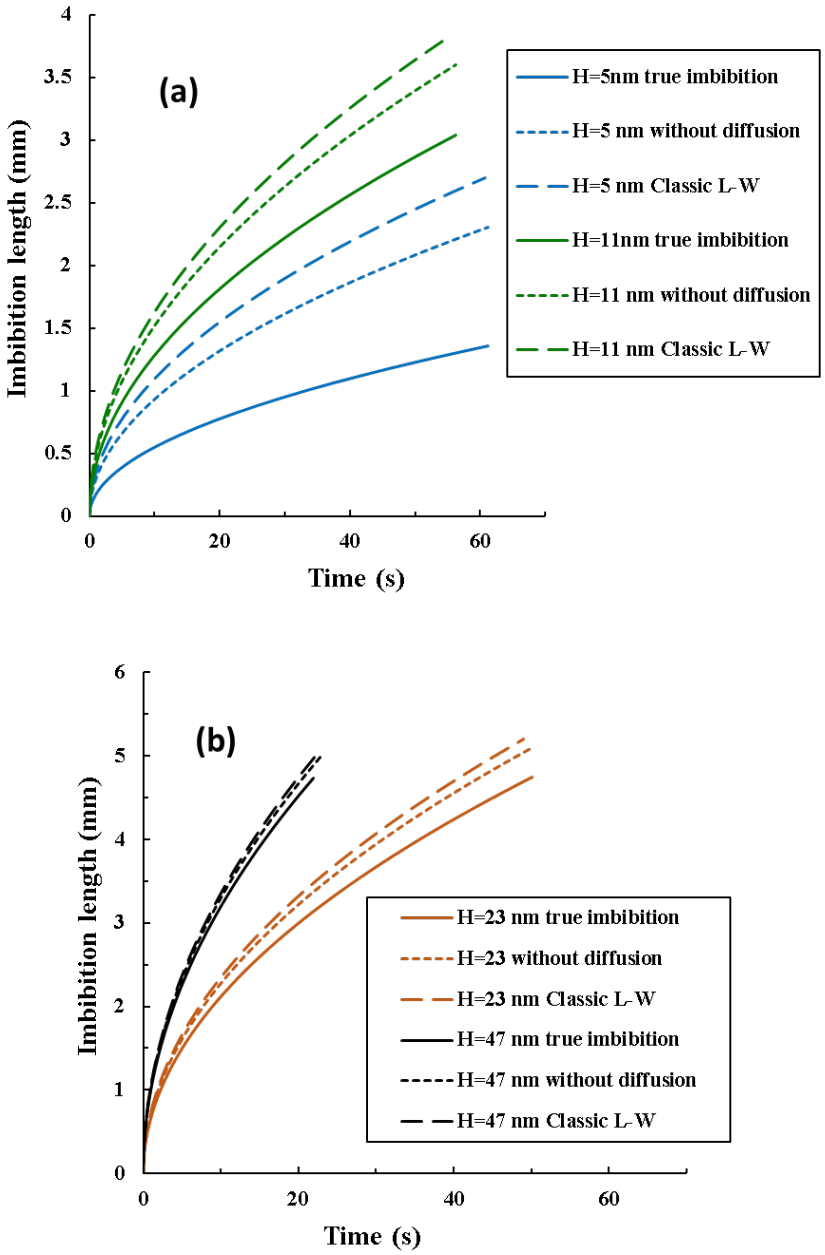

Figure 6. 9 (a) The imbibition length without diffusion and that calculated by the classical L-W model for nano-channels with channel heights of 5 nm and 11 nm; (b) the imbibition length without diffusion and that calculated by the classical L-W model for nano-channels with channel heights of 23 nm 47 nm

6.3.3 The effects of solidified water layers

The properties of films and a macroscopic region are different, mainly in three aspects: viscosity, density, and a molecular structure. It is known that the first two water layers have higher densities compared with

the bulk phase. Moreover, it was known that the mobility of the first two water layers was significantly reduced, especially the first layer whose mobility is reduced by an order of magnitude. Therefore, the water film thickness is chosen as the thickness of two water layers.

The properties of the solidified water layers have many applications in the engineering field; an important one is the water retention phenomenon during the production process of shale gas. As mentioned in Chapter 1, during the exploitation phase, a great amount of water is required for hydraulic fracturing of multi-lateral horizontal wells. However, only a small fraction of the injected water can be recovered during a flowback process because of spontaneous. After the flowback phase, the residual water will exist in the form of films attached to solid surfaces with very low mobility [121]. It is well known that micropores (<2nm) and mesopores (<50nm) are dominated in shale formations [69]. Therefore, the water volume of films will take a great portion of the void volume, leading to low recovery of the injected water.

6.3.4 The dimension issue

As discussed in Chapter 1, the quasi-continuum flow regime is considered in this work, and precursor films only occur when a bulk phase exists. It should be noted that when the confinement is so extreme that a bulk phase vanishes, the continuum theory will be totally violated. This is called sub-continuum flow, indicating that the size of a liquid molecule is comparable to the size of the flow domain. Within such sub-continuum systems, the whole cross-area for liquid flow is under the impact of the solid surfaces, and the movement of individual molecules must be considered when predicting mass and momentum transport [339]. Thomas and McGaughey assessed this flow regime and found that the confinement-induced changes to the liquid structure may reduce flow enhancement [49]. Moreover, the non-local rheological properties have been predicted in strongly confined situations, associated with a length characterizing non-locality typically in a range of several molecules diameters [340]. Furthermore, the single-file transport behavior was investigated by some scholars, and various specific phenomena were reported, like non-

fickian transport and fast ion transfer [341,342]. All these new phenomena make the sub-continuum flow problem a different research topic, which is still an open challenge.

6.4 Summary

In this part, the capillary dynamics of confined water in nanopores considering precursor films are investigated. Models for imbibition lengths in nano-channels and nano-capillaries are proposed, which are validated by experimental and MD results. The increased viscosity effect for water near a solid surface is considered in the models, and the motion of a meniscus is regarded to be driven by a dynamic contact angle based on the Molecular Kinetic Theory. Furthermore, the fluid loss from the surface water into precursor films is incorporated in the proposed models. It is found that under a completely wetting case, the first two water layers have significantly increased viscosity compared with the bulk phase. Besides, the surface water diffusion from the macroscopic region into the precursor films is an important phenomenon for capillary dynamics of nanoconfined water, which is a determinant for the imbibition behavior for both the main meniscus and the precursor films. For a nano-channel with a width of 5 nm, the predicted imbibition length without the consideration of the fluid loss will almost be double of the true imbibition length. Moreover, this deviation becomes smaller and smaller as the pore size increases. Furthermore, it is found that the impact of the dynamic contact angle on the motion of the meniscus can be neglected, indicating a possible efficiency of nano-channel-coating by the precursor films. The proposed models capture important physics for capillary dynamics at the nanoscale and will have wide applications in the chemical and engineering field.

Chapter 7 Conclusions and recommendations

In this thesis, the water imbibition behavior in shale was investigated. Theoretical models were proposed which consider the unique characteristics for water flow under nanoconfined conditions. The main work and conclusions are summarized as follows:

1. A model that describes the solid-solid friction is applied and modified to compute the friction force for a liquid-solid friction process. The trajectories for water molecules within the first density layer are analyzed and a method for the calculation of friction is proposed based on the trajectories and total L-J curves. The modified model is validated with MD simulations. It is found that the liquid-solid friction has many similarities in mechanisms with the solid-solid friction, in terms of the energy barrier, based on Eyring's kinetic theory of liquid molecules. All friction processes arise from the dissipation of the energy that is acquired by the molecules to overcome energy barriers. Moreover, a close relationship between the slip process and friction is analyzed, and a theoretical relationship between the slip velocity and friction force is obtained. The slip velocity of the first water density layer and the friction force at a water-graphene interface follow a hyperbolic-like relationship, which is almost linear under realistic conditions.

2. A theoretical model for the effective viscosity for water imbibition in shale formations is proposed according to Eyring's molecular kinetic theory. Strong interactions between water molecules and solid surfaces are considered based on the disjoining pressure. The validity of the proposed viscosity model to predict spontaneous imbibition is checked by experimental results in the published literature. Besides, the main factors that affect the effective viscosity, including a pore size, a pore shape, the properties of a solid material, and the existence of an initial water film, are discussed. The effective viscosity is much higher for water under confined conditions, and it increases rapidly when the characteristic length of nanopores is lower than 10 nm. The effective viscosity for cylindrical nanopores is always larger than that for slit nanopores when the characteristic lengths are the same, and the difference is more obvious for small

nanopores. Besides, the solid properties strongly affect the magnitude of the effective viscosity. The effective viscosity for water under hydrophilic conditions is much higher than that under hydrophobic conditions. The molecular component is the dominant mechanism among the components that contribute to the increased viscosity, and the electrical component, as well as the structural component, can be neglected.

3. A unified model for water flow in a quasi-continuum regime is proposed, coupling the effective viscosity and the slip behavior. It is found that the effective viscosity of water is highly affected by a wettability condition, and a linear relationship exists between a contact angle and the interfacial viscosity. A strongly hydrophilic surface tends to increase the effective viscosity dramatically, while a small decrease in the effective viscosity can be observed under a hydrophobic condition. This is mainly due to the different magnitudes of the Hamaker constant under various wettability conditions. Moreover, it is found that the applied slip length model considers most of the factors that affect the slip length, except for a molecular structure of a solid substrate.

The deviations of a flow rate from the prediction by the traditional Hagen-Poiseuille equation contributed by the effective viscosity and the slip length are analyzed. It is found that under strongly hydrophilic conditions, both factors are nonnegligible for the total flow rate, while the slip behavior becomes a dominant factor when the contact angle reaches over 100˚. In addition, an application of the above theories to a capillary filling process in the chemical engineering field has been discussed.

4. The capillary dynamics of confined water in nanopores are investigated, considering the propagation of precursor films. Models for imbibition lengths in nano-channels and nano-capillaries are proposed and validated by experimental and MD results. The increased viscosity effect for water near a solid, as well as the dynamic contact angle, are incorporated in the proposed model. Furthermore, the fluid loss from the surface water into precursor films is considered. It is found that under a completely wetting case, the surface water diffusion from a macroscopic region into the precursor films is an important phenomenon

for capillary dynamics of nanoconfined water, which is a determinant for the imbibition behavior for both the main meniscus and the precursor films. Furthermore, it is found that the impact of the dynamic contact angle on the motion of the meniscus is negligible. The proposed models capture important physics for capillary dynamics at the nanoscale and will have wide applications in the chemical and engineering field. The recommendations for future work include:

1. The effect of salt dissolved in water is not considered in this work. It is known that the salinity may affect the water imbibition behavior in nanopores, as many scholars have observed the osmosis pressure-driven flow in nano-fluidic experiments. The slip behavior for the water boundary layer should be further investigated, considering the salt-solid interactions.

2. For solid materials with high energy, the effective thickness of the precursor films may be below the diameter of one water molecule. In this case, the capillary dynamics will be highly affected by the dynamic contact angle, rather than the precursor films. This research topic requires further research.

3. The research of the imbibition behavior of oil in nanopores is still lacking. The properties of the oil are totally different from water, and there may be other mechanisms of spontaneous imbibition for oil in nanopores. This research topic needs much experimental and theoretical work.

References

[1] A. Behrang, P. Mohammadmoradi, S. Taheri, A. Kantzas, A theoretical study on the permeability of tight media; Effects of slippage and condensation, Fuel. 181 (2016) 610–617. https://doi.org/10.1016/j.fuel.2016.05.048.

[2] H. Tran, A. Sakhaee-Pour, Viscosity of shale gas, Fuel. 191 (2017) 87–96. https://doi.org/10.1016/j.fuel.2016.11.062.

[3] Y. Xu, O. Adefidipe, H. Dehghanpour, A flowing material balance equation for two-phase flowback analysis, J. Pet. Sci. Eng. 142 (2016) 170–185. https://doi.org/10.1016/j.petrol.2016.01.018.

[4] I. Vandecasteele, I.M. Rivero, S. Sala, C. Baranzelli, R. Barranco, O. Batelaan, C. Lavalle, Impact of shale gas development on water resources: a case study in northern Poland, Environ. Manage. 55 (2015) 1285–1299.

[5] J.-P. Nicot, B.R. Scanlon, Water use for shale-gas production in Texas, US, Environ. Sci. Technol. 46 (2012) 3580–3586.

[6] O. Ezulike, H. Dehghanpour, C. Virues, R. V Hawkes, R.S. Jones Jr, Flowback fracture closure: A key factor for estimating effective pore volume, SPE Reserv. Eval. Eng. 19 (2016) 567–582.

[7] A. Settari, R.B. Sullivan, R.C. Bachman, The modeling of the effect of water blockage and geomechanics in waterfracs, in: SPE Annu. Tech. Conf. Exhib., Society of Petroleum Engineers, 2002.

[8] Y. Cheng, Impact of water dynamics in fractures on the performance of hydraulically fractured wells in gas-shale reservoirs, J. Can. Pet. Technol. 51 (2012) 143–151.

[9] Z. Sun, J. Shi, T. Zhang, K. Wu, Y. Miao, D. Feng, F. Sun, S. Han, S. Wang, C. Hou, X. Li, The modified gas-water two phase version flowing material balance equation for low permeability

CBM reservoirs, J. Pet. Sci. Eng. 165 (2018) 726–735. https://doi.org/10.1016/j.petrol.2018.03.011.

[10] D.J. Bonthuis, D. Horinek, L. Bocquet, R.R. Netz, Electrohydraulic power conversion in planar nanochannels, Phys. Rev. Lett. 103 (2009) 144503.

[11] D. Gillespie, High energy conversion efficiency in nanofluidic channels, Nano Lett. 12 (2012) 1410–1416.

[12] D. Cohen-Tanugi, J.C. Grossman, Water desalination across nanoporous graphene, Nano Lett. 12 (2012) 3602–3608.

[13] S.J. Kim, S.H. Ko, K.H. Kang, J. Han, Direct seawater desalination by ion concentration polarization, Nat. Nanotechnol. 5 (2010) 297–301.

[14] J. Rouquerol, D. Avnir, C.W. Fairbridge, D.H. Everett, J.M. Haynes, N. Pernicone, J.D.F. Ramsay, K.S.W. Sing, K.K. Unger, Recommendations for the characterization of porous solids (Technical Report), Pure Appl. Chem. 66 (1994) 1739–1758.

[15] Y. Li, A. Kalantari-Dahaghi, A. Zolfaghari, P. Dong, S. Negahban, D. Zhou, Fractal-based real gas flow model in shales: An interplay of nano-pore and nano-fracture networks, Int. J. Heat Mass Transf. 127 (2018) 1188–1202. https://doi.org/10.1016/j.ijheatmasstransfer.2018.08.077.

[16] K. Wu, Z. Chen, J. Li, J. Xu, K. Wang, S. Wang, X. Dong, Z. Zhu, Y. Peng, X. Jia, X. Li, Manipulating the Flow of Nanoconfined Water by Temperature Stimulation, Angew. Chemie - Int. Ed. 57 (2018) 8432–8437. https://doi.org/10.1002/anie.201712915.

[17] K. Wu, Z. Chen, J. Li, Z. Lei, J. Xu, K. Wang, R. Li, X. Dong, Y. Peng, S. Yang, F. Zhang, Z. Chen, Y. Gao, Nanoconfinement Effect on n-Alkane Flow, J. Phys. Chem. C. (2019). https://doi.org/10.1021/acs.jpcc.9b03903.

[18] J. Tao, X. Song, T. Zhao, S. Zhao, H. Liu, Confinement effect on water transport in CNT membranes, Chem. Eng. Sci. 192 (2018) 1252–1259. https://doi.org/10.1016/j.ces.2018.05.018.

[19] M.H. Köhler, J.R. Bordin, C.F. de Matos, M.C. Barbosa, Water in nanotubes: The surface effect, Chem. Eng. Sci. 203 (2019) 54–67. https://doi.org/10.1016/j.ces.2019.03.062.

[20] C. Bakli, S. Chakraborty, Capillary filling dynamics of water in nanopores, Appl. Phys. Lett. 101 (2012). https://doi.org/10.1063/1.4758683.

[21] M.R. Stukan, P. Ligneul, J.P. Crawshaw, E.S. Boek, Spontaneous imbibition in nanopores of different roughness and wettability, Langmuir. 26 (2010) 13342–13352.

[22] F.F. Abraham, The interfacial density profile of a Lennard-Jones fluid in contact with a (100) Lennard-Jones wall and its relationship to idealized fluid/wall systems: A Monte Carlo simulation, J. Chem. Phys. 68 (1978) 3713–3716. https://doi.org/10.1063/1.436229.

[23] P. Tarazona, L. Vicente, A model for density oscillations in liquids between solid walls, Mol. Phys. 56 (1985) 557–572. https://doi.org/10.1080/00268978500102521.

[24] C. Zhang, Z. Liu, P. Deng, Contact angle of soil minerals: A molecular dynamics study, Comput. Geotech. 75 (2016) 48–56. https://doi.org/10.1016/j.compgeo.2016.01.012.

[25] A.A. Milischuk, B.M. Ladanyi, Structure and dynamics of water confined in silica nanopores, J. Chem. Phys. 135 (2011). https://doi.org/10.1063/1.3657408.

[26] C. Sendner, D. Horinek, L. Bocquet, R.R. Netz, Interfacial water at hydrophobic and hydrophilic surfaces: Slip, viscosity, and diffusion, Langmuir. 25 (2009) 10768–10781. https://doi.org/10.1021/la901314b.

[27] M. Wu, W. Wei, X. Liu, K. Liu, S. Li, Structure and dynamic properties of stretched water in graphene nanochannels by molecular dynamics simulation: Effects of stretching extent, Phys. Chem. Chem. Phys. 21 (2019) 19163–19171. https://doi.org/10.1039/c9cp03981c.

[28] E. Wagemann, E. Oyarzua, J.H. Walther, H.A. Zambrano, Slip divergence of water flow in graphene nanochannels: The role of chirality, Phys. Chem. Chem. Phys. 19 (2017) 8646–8652. https://doi.org/10.1039/c6cp07755b.

[29] M. Kargar, A. Lohrasebi, Water flow modeling through a graphene-based nanochannel: Theory and simulation, Phys. Chem. Chem. Phys. 21 (2019) 3304–3309. https://doi.org/10.1039/C8CP06839A.

[30] H. Hoang, G. Galliero, Local viscosity of a fluid confined in a narrow pore, Phys. Rev. E - Stat. Nonlinear, Soft Matter Phys. 86 (2012) 1–10. https://doi.org/10.1103/PhysRevE.86.021202.

[31] M. Neek-Amal, F.M. Peeters, I. V. Grigorieva, A.K. Geim, Commensurability Effects in Viscosity of Nanoconfined Water, ACS Nano. 10 (2016) 3685–3692. https://doi.org/10.1021/acsnano.6b00187.

[32] J.A. Thomas, A.J.H. McGaughey, Effect of surface wettability on liquid density, structure, and diffusion near a solid surface, J. Chem. Phys. 126 (2007). https://doi.org/10.1063/1.2424934.

[33] J.A. Thomas, A.J.H. Mcgaughey, Reassessing Fast Water Transport Through Carbon Nanotubes, Nano Lett. 8 (2008) 2788–2793. https://doi.org/10.1016/B978-008044475-8/50017-2.

[34] J.W. Van Honschoten, N. Brunets, N.R. Tas, Capillarity at the nanoscale, Chem. Soc. Rev. 39 (2010) 1096–1114. https://doi.org/10.1039/b909101g.

[35] L. Bocquet, E. Charlaix, Nanofluidics, from bulk to interfaces, Chem. Soc. Rev. 39 (2010) 1073–1095. https://doi.org/10.1039/b909366b.

[36] D. Feng, X. Li, X. Wang, J. Li, X. Zhang, Capillary filling under nanoconfinement: The relationship between effective viscosity and water-wall interactions, Int. J. Heat Mass Transf. 118 (2018) 900–910. https://doi.org/10.1016/j.ijheatmasstransfer.2017.11.049.

[37] D. Feng, X. Li, K. Wu, J. Li, W. Zhao, Capillary dynamic under nanoconfinement: Coupling the energy dissipation of contact line and confined water, Int. J. Heat Mass Transf. 127 (2018) 329–338. https://doi.org/10.1016/j.ijheatmasstransfer.2018.07.114.

[38] D. Feng, X. Li, X. Wang, J. Li, T. Zhang, Z. Sun, M. He, Q. Liu, J. Qin, S. Han, J. Hu, Anomalous Capillary Rise under Nanoconfinement: A View of Molecular Kinetic Theory, Langmuir. 34 (2018) 7714–7725. https://doi.org/10.1021/acs.langmuir.8b01397.

[39] D. Feng, K. Wu, X. Wang, J. Li, X. Li, Modeling the confined fluid flow in micro-nanoporous media under geological temperature and pressure, Int. J. Heat Mass Transf. 145 (2019) 118758. https://doi.org/10.1016/j.ijheatmasstransfer.2019.118758.

[40] S. Joseph, N.R. Aluru, Why are carbon nanotubes fast transporters of water?, Nano Lett. 8 (2008) 452–458. https://doi.org/10.1021/nl072385q.

[41] H. Zhang, H. Ye, Y. Zheng, Z. Zhang, Prediction of the viscosity of water confined in carbon nanotubes, Microfluid. Nanofluidics. 10 (2011) 403–414. https://doi.org/10.1007/s10404-010-0678-0.

[42] R.B. Schoch, J. Han, P. Renaud, Transport phenomena in nanofluidics, Rev. Mod. Phys. 80 (2008) 839–883. https://doi.org/10.1103/RevModPhys.80.839.

[43] R. Bhadauria, N.R. Aluru, A quasi-continuum hydrodynamic model for slit shaped nanochannel flow, J. Chem. Phys. 139 (2013). https://doi.org/10.1063/1.4818165.

[44] K.P. Travis, B.D. Todd, D.J. Evans, Departure from Navier-Stokes hydrodynamics in confined liquids, Phys. Rev. E - Stat. Physics, Plasmas, Fluids, Relat. Interdiscip. Top. 55 (1997) 4288–4295. https://doi.org/10.1103/PhysRevE.55.4288.

[45] T. Becker, F. Mugele, Nanofluidics: viscous dissipation in layered liquid films, Phys. Rev. Lett. 91 (2003) 166104.

[46] A. Maali, T. Cohen-Bouhacina, G. Couturier, J.-P. Aimé, Oscillatory dissipation of a simple confined liquid, Phys. Rev. Lett. 96 (2006) 86105.

[47] J. Gao, R. Szoszkiewicz, U. Landman, E. Riedo, Structured and viscous water in subnanometer gaps, Phys. Rev. B. 75 (2007) 115415.

[48] D.Y.C. Chan, R.G. Horn, The drainage of thin liquid films between solid surfaces, J. Chem. Phys. 83 (1985) 5311–5324.

[49] J.A. Thomas, A.J.H. McGaughey, Water flow in carbon nanotubes: Transition to subcontinuum transport, Phys. Rev. Lett. 102 (2009) 1–4. https://doi.org/10.1103/PhysRevLett.102.184502.

[50] L. Bocquet, J.L. Barrat, Flow boundary conditions from nano- to micro-scales, Soft Matter. 3 (2007) 685–693. https://doi.org/10.1039/b616490k.

[51] Y. Leng, P.T. Cummings, Fluidity of hydration layers nanoconfined between mica surfaces, Phys. Rev. Lett. 94 (2005) 26101.

[52] Q. Wang, X. Chen, A.N. Jha, H. Rogers, Natural gas from shale formation–the evolution, evidences and challenges of shale gas revolution in United States, Renew. Sustain. Energy Rev. 30 (2014) 1–28.

[53] B.K. Sovacool, Cornucopia or curse? Reviewing the costs and benefits of shale gas hydraulic fracturing (fracking), Renew. Sustain. Energy Rev. 37 (2014) 249–264.

[54] K.B. Medlock III, A.M. Jaffe, P.R. Hartley, Shale gas and US national security, (2011).

[55] J. Yuan, D. Luo, L. Feng, A review of the technical and economic evaluation techniques for shale gas development, Appl. Energy. 148 (2015) 49–65. https://doi.org/10.1016/j.apenergy.2015.03.040.

[56] J. Kersting, V. Duscha, J. Schleich, K. Keramidas, The impact of shale gas on the costs of climate policy, Clim. Policy. 18 (2018) 442–458.

[57] M. Melikoglu, Shale gas: Analysis of its role in the global energy market, Renew. Sustain. Energy Rev. 37 (2014) 460–468.

[58] C. McGlade, J. Speirs, S. Sorrell, Unconventional gas–a review of regional and global resource estimates, Energy. 55 (2013) 571–584.

[59] A.C. Aplin, J.H.S. Macquaker, Mudstone diversity: Origin and implications for source, seal, and reservoir properties in petroleum systems, Am. Assoc. Pet. Geol. Bull. 95 (2011) 2031–2059. https://doi.org/10.1306/03281110162.

[60] F.T. Mackenzie, R.M. Garrels, Evolution of sedimentary rocks, Norton New York, 1971.

[61] A.B. Ronov, The Earth's sedimentary shell (quantitative patterns of its structure, compositions, and evolution) The 20th VI Vernadskiy Lecture, March 12, 1978, Int. Geol. Rev. 24 (1982) 1313–1363.

[62] C.E. Weaver, Clays, muds, and shales, Elsevier, 1989.

[63] P.E. Potter, J.B. Maynard, P.J. Depetris, Mud and mudstones: Introduction and overview, Springer Science & Business Media, 2005.

[64] C.J. Modica, S.G. Lapierre, Estimation of kerogen porosity in source rocks as a function of thermal transformation: Example from the Mowry Shale in the Powder River Basin of Wyoming, Am. Assoc. Pet. Geol. Bull. 96 (2012) 87–108. https://doi.org/10.1306/04111110201.

[65] K.L. Milliken, M. Rudnicki, D.N. Awwiller, T. Zhang, Organic matter-hosted pore system, Marcellus Formation (Devonian), Pennsylvania, Am. Assoc. Pet. Geol. Bull. 97 (2013) 177–200. https://doi.org/10.1306/07231212048.

[66] X. Cui, A.M.M. Bustin, R.M. Bustin, Measurements of gas permeability and diffusivity of tight reservoir rocks: different approaches and their applications, Geofluids. 9 (2009) 208–223.

[67] T. Zhang, G.S. Ellis, S.C. Ruppel, K. Milliken, R. Yang, Effect of organic-matter type and thermal maturity on methane adsorption in shale-gas systems, Org. Geochem. 47 (2012) 120–131.

[68] J. Li, X. Li, K. Wu, X. Wang, J. Shi, L. Yang, H. Zhang, Z. Sun, R. Wang, D. Feng, Water Sorption and Distribution Characteristics in Clay and Shale: Effect of Surface Force, Energy and Fuels. 30 (2016) 8863–8874. https://doi.org/10.1021/acs.energyfuels.6b00927.

[69] M.E. Curtis, C.H. Sondergeld, R.J. Ambrose, C.S. Rai, Microstructural investigation of gas shales in two and three dimensions using nanometer-scale resolution imaging, Am. Assoc. Pet. Geol. Bull. 96 (2012) 665–677. https://doi.org/10.1306/08151110188.

[70] G.R. Chalmers, R.M. Bustin, I.M. Power, Characterization of gas shale pore systems by porosimetry, pycnometry,surfacearea,andfield emission scanning electron microscopy/ transmission electron microscopy image analyses: Examples from the Barnett, Woodford, Haynesville, Marcellus,andDoig units, Am. Assoc. Pet. Geol. Bull. 96 (2012) 1099–1119. https://doi.org/10.1306/10171111052.

[71] R.M. Slatt, N. Buckner, Y. Abousleiman, R. Sierra, P.R. Philp, A. Miceli-Romero, R. Portas, N. O'Brien, M. Tran, R. Davis, T. Wawrzyniec, Outcrop-behind outcrop (quarry): Multiscale characterization of the woodford gas shale, Oklahoma, AAPG Mem. 97 (2012) 382–402. https://doi.org/10.1306/13321481M97441.

[72] R.G. Loucks, R.M. Reed, S.C. Ruppel, U. Hammes, Spectrum of pore types and networks in mudrocks and a descriptive classification for matrix-related mudrock pores, Am. Assoc. Pet. Geol. Bull. 96 (2012) 1071–1098. https://doi.org/10.1306/08171111061.

[73] R.M. Slatt, N.R. O'Brien, Pore types in the Barnett and Woodford gas shales: Contribution to understanding gas storage and migration pathways in fine-grained rocks, Am. Assoc. Pet. Geol. Bull. 95 (2011) 2017–2030. https://doi.org/10.1306/03301110145.

[74] J.L. Rubinstein, A.B. Mahani, Myths and facts on wastewater injection, hydraulic fracturing, enhanced oil recovery, and induced seismicity, Seismol. Res. Lett. 86 (2015) 1060–1067.

[75] M.J. Economides, K.G. Nolte, Reservoir stimulation, Prentice Hall Englewood Cliffs, NJ, 1989.

[76] K.B. Gregory, R.D. Vidic, D.A. Dzombak, Water management challenges associated with the production of shale gas by hydraulic fracturing, Elements. 7 (2011) 181–186.

[77] O.A. Adefidipe, H. Dehghanpour, C.J. Virues, Immediate gas production from shale gas wells: A two-phase flowback model, Soc. Pet. Eng. - SPE USA Unconv. Resour. Conf. 2014. (2014) 247–262. https://doi.org/10.2118/168982-ms.

[78] F.R. Spellman, Environmental impacts of hydraulic fracturing, CRC Press, 2012.

[79] X. Yan, Z.Q. Huang, J. Yao, Y. Li, D. Fan, H. Sun, K. Zhang, An efficient numerical hybrid model for multiphase flow in deformable fractured-shale reservoirs, SPE J. 23 (2018) 1412–1437. https://doi.org/10.2118/191122-pa.

[80] P. Cao, J. Liu, Y.K. Leong, A multiscale-multiphase simulation model for the evaluation of shale gas recovery coupled the effect of water flowback, Fuel. 199 (2017) 191–205. https://doi.org/10.1016/j.fuel.2017.02.078.

[81] M. Xu, H. Dehghanpour, Advances in understanding wettability of gas shales, Energy and Fuels. 28 (2014) 4362–4375. https://doi.org/10.1021/ef500428y.

[82] A. Zolfaghari, H. Dehghanpour, M. Noel, D. Bearinger, Laboratory and field analysis of flowback water from gas shales, J. Unconv. Oil Gas Resour. 14 (2016) 113–127.

[83] M. Binazadeh, M. Xu, A. Zolfaghari, H. Dehghanpour, Effect of Electrostatic Interactions on Water Uptake of Gas Shales: The Interplay of Solution Ionic Strength and Electrostatic Double Layer, Energy and Fuels. 30 (2016) 992–1001. https://doi.org/10.1021/acs.energyfuels.5b02990.

[84] K. Makhanov, A. Habibi, H. Dehghanpour, E. Kuru, Liquid uptake of gas shales: A workflow to estimate water loss during shut-in periods after fracturing operations, J. Unconv. Oil Gas Resour. 7 (2014) 22–32. https://doi.org/10.1016/j.juogr.2014.04.001.

[85] Y. Sun, B. Bai, M. Wei, Microfracture and surfactant impact on linear cocurrent brine imbibition in gas-saturated shale, Energy & Fuels. 29 (2015) 1438–1446.

[86] H. Roshan, S. Ehsani, C.E. Marjo, M.S. Andersen, R.I. Acworth, Mechanisms of water adsorption into partially saturated fractured shales: An experimental study, Fuel. 159 (2015) 628–637.

[87] H. Bahrami, R. Rezaee, B. Clennell, Water blocking damage in hydraulically fractured tight sand gas reservoirs: An example from Perth Basin, Western Australia, J. Pet. Sci. Eng. 88–89 (2012) 100–106. https://doi.org/10.1016/j.petrol.2012.04.002.

[88] H. Singh, A critical review of water uptake by shales, J. Nat. Gas Sci. Eng. 34 (2016) 751–766. https://doi.org/10.1016/j.jngse.2016.07.003.

[89] R. Dutta, Quantification of fracturing fluid migration due to spontaneous imbibition in fractured tight formations, (2012).

[90] L. Yang, X. Shi, K. Zhang, H. Ge, J. Gao, X. Tan, P. Xu, L. Li, The effects of fracturing fluid imbibition on fracture conductivity in tight reservoirs, 51st US Rock Mech. / Geomech. Symp. 2017. 3 (2017) 1930–1934.

[91] W. Jing, L. Huiqing, Q. Genbao, P. Yongcan, G. Yang, Investigations on spontaneous imbibition and the influencing factors in tight oil reservoirs, Fuel. 236 (2019) 755–768. https://doi.org/10.1016/j.fuel.2018.09.053.

[92] D. Xu, B. Bai, H. Wu, J. Hou, Z. Meng, R. Sun, Z. Li, Y. Lu, W. Kang, Mechanisms of imbibition enhanced oil recovery in low permeability reservoirs: Effect of IFT reduction and wettability alteration, Fuel. 244 (2019) 110–119. https://doi.org/10.1016/j.fuel.2019.01.118.

[93] E. Ghanbari, H. Dehghanpour, The fate of fracturing water: A field and simulation study, Fuel. 163 (2016) 282–294. https://doi.org/10.1016/j.fuel.2015.09.040.

[94] Q. Lan, E. Ghanbari, H. Dehghanpour, R. Hawkes, Water Loss Versus Soaking Time: Spontaneous Imbibition in Tight Rocks, Energy Technol. 2 (2014) 1033–1039. https://doi.org/10.1002/ente.201402039.

[95] L. Yang, D. Liu, H. Ge, Y. Shen, C. Li, K. Zhang, Experimental investigation on the effects of flow resistance on the fracturing fluids imbibition into gas shale, Soc. Pet. Eng. - SPE Asia Pacific Hydraul. Fract. Conf. (2016). https://doi.org/10.2118/181825-ms.

[96] Z. Zhou, B. Hoffman, D. Bearinger, X. Li, Experimental and numerical study on spontaneous imbibition of fracturing fluids in shale gas formation, Soc. Pet. Eng. - SPE Can. Unconv. Resour. Conf. 2014. 1 (2014) 425–437. https://doi.org/10.2118/171600-ms.

[97] M.A.Q. Siddiqui, X. Chen, S. Iglauer, H. Roshan, A Multiscale Study on Shale Wettability: Spontaneous Imbibition Versus Contact Angle, Water Resour. Res. 55 (2019) 5012–5032. https://doi.org/10.1029/2019WR024893.

[98] T. Zhang, X. Li, Z. Sun, D. Feng, Y. Miao, P. Li, Z. Zhang, An analytical model for relative permeability in water-wet nanoporous media, Chem. Eng. Sci. 174 (2017) 1–12. https://doi.org/10.1016/j.ces.2017.08.023.

[99] O. Vincent, A. Szenicer, A.D. Stroock, Capillarity-driven flows at the continuum limit, Soft Matter. 12 (2016) 6656–6661. https://doi.org/10.1039/c6sm00733c.

[100] J. Zang, X. Yan, Y. Li, X. Zeng, Y. Huang, The flow resistance experiments of supercritical pressure water in 2 × 2 rod bundle, Int. J. Heat Mass Transf. 147 (2020) 118873. https://doi.org/10.1016/j.ijheatmasstransfer.2019.118873.

[101] J.W. van Honschoten, N.R. Tas, M. Elwenspoek, The profile of a capillary liquid bridge between solid surfaces, Am. J. Phys. 78 (2010) 277–286. https://doi.org/10.1119/1.3273854.

[102] E. Oyarzua, J.H. Walther, A. Mejía, H.A. Zambrano, Early regimes of water capillary flow in slit silica nanochannels, Phys. Chem. Chem. Phys. 17 (2015) 14731–14739. https://doi.org/10.1039/c5cp01862e.

[103] A. Cihan, T.K. Tokunaga, J.T. Birkholzer, Adsorption and Capillary Condensation-Induced Imbibition in Nanoporous Media, Langmuir. 35 (2019) 9611–9621. https://doi.org/10.1021/acs.langmuir.9b00813.

[104] W. Stroberg, S. Keten, W.K. Liu, Hydrodynamics of capillary imbibition under nanoconfinement, Langmuir. 28 (2012) 14488–14495. https://doi.org/10.1021/la302292w.

[105] A. Borysenko, B. Clennell, R. Sedev, I. Burgar, J. Ralston, M. Raven, D. Dewhurst, K. Liu, Experimental investigations of the wettability of clays and shales, J. Geophys. Res. Solid Earth. 114 (2009) 1–11. https://doi.org/10.1029/2008JB005928.

[106] K. Makhanov, H. Dehghanpour, E. Kuru, An experimental study of spontaneous imbibition in Horn River shales, in: SPE Can. Unconv. Resour. Conf., Society of Petroleum Engineers, 2012.

[107] K. Ksiezniak, A. Rogala, J. Hupka, Wettability of shale rock as an indicator of fracturing fluid composition, Physicochem. Probl. Miner. Process. 51 (2015).

[108] D. Wang, R. Butler, J. Zhang, R. Seright, Wettability survey in bakken shale with surfactant-formulation imbibition, SPE Reserv. Eval. Eng. 15 (2012) 695–705. https://doi.org/10.2118/153853-PA.

[109] E.O. Odusina, C.H. Sondergeld, C.S. Rai, NMR Study of Shale Wettability, Can. Unconv. Resour. Conf. (2011) 15. https://doi.org/10.2118/147371-MS.

[110] E. Ghanbari, H. Dehghanpour, Impact of rock fabric on water imbibition and salt diffusion in gas shales, Int. J. Coal Geol. 138 (2015) 55–67. https://doi.org/10.1016/j.coal.2014.11.003.

[111] A.W. Neumann, R. David, Y. Zuo, Applied surface thermodynamics, CRC press, 2010.

[112] P. Blecua, R. Lipowsky, J. Kierfeld, Line tension effects for liquid droplets on circular surface domains, Langmuir. 22 (2006) 11041–11059.

[113] Y. Yuan, T.R. Lee, Contact angle and wetting properties, in: Surf. Sci. Tech., Springer, 2013: pp. 3–34.

[114] A. Marmur, Line tension and the intrinsic contact angle in solid–liquid–fluid systems, J. Colloid Interface Sci. 186 (1997) 462–466.

[115] X. Yu, J. Li, Z. Chen, K. Wu, L. Zhang, G. Hui, M. Yang, Molecular dynamics computations of brine-CO2/CH4-shale contact angles: Implications for CO2 sequestration and enhanced gas recovery, Fuel. 280 (2020) 118590.

[116] R. Lucas, Ueber das Zeitgesetz des kapillaren Aufstiegs von Flüssigkeiten, Kolloid-Zeitschrift. 23 (1918) 15–22.

[117] E.W. Washburn, The dynamics of capillary flow, Phys. Rev. 17 (1921) 273–283. https://doi.org/10.1103/PhysRev.17.273.

[118] G. Mason, N.R. Morrow, Developments in spontaneous imbibition and possibilities for future work, J. Pet. Sci. Eng. 110 (2013) 268–293. https://doi.org/10.1016/j.petrol.2013.08.018.

[119] B. V. Derjaguin, N. V. Churaev, Polymolecular adsorption and capillary condensation in narrow slit pores, Prog. Surf. Sci. 40 (1992) 173–191. https://doi.org/10.1016/0079-6816(92)90045-J.

[120] N. V. Churaev, M.J. Setzer, J. Adolphs, Influence of surface wettability on adsorption isotherms of water vapor, J. Colloid Interface Sci. 197 (1998) 327–333. https://doi.org/10.1006/jcis.1997.5292.

[121] M. Tuller, O. Dani, L.M. Dudley, Adsorption and capillary condensation in porous media: Liquid retention and interfacial configurations in angular pores, Water Resour. Res. 35 (1999) 1949–1964. https://doi.org/10.1029/1999WR900098.

[122] J. Li, X. Li, X. Wang, Y. Li, K. Wu, J. Shi, L. Yang, D. Feng, T. Zhang, P. Yu, Water distribution characteristic and effect on methane adsorption capacity in shale clay, Int. J. Coal Geol. 159 (2016) 135–154. https://doi.org/10.1016/j.coal.2016.03.012.

[123] J. Li, X. Li, K. Wu, D. Feng, T. Zhang, Y. Zhang, Thickness and stability of water film confined inside nanoslits and nanocapillaries of shale and clay, Int. J. Coal Geol. 179 (2017) 253–268. https://doi.org/10.1016/j.coal.2017.06.008.

[124] B.V. Derjaguin, N.V. Churaev, V.M. Muller, V.I. Kisin, Surface forces, Springer, 1987.

[125] T.F. Tadros, Encyclopedia of colloid and interface science, Springer Berlin, 2013.

[126] M. Windows, M. Corporation, K. Hori, A. Sakajiri, Wetting and spreading dynamics, (n.d.).

[127] H.-K. Ge, L. Yang, Y.-H. Shen, K. Ren, F.-B. Meng, W.-M. Ji, S. Wu, Experimental investigation of shale imbibition capacity and the factors influencing loss of hydraulic fracturing fluids, Pet. Sci. 12 (2015) 636–650.

[128] L. Yang, H. Ge, X. Shi, Y. Cheng, K. Zhang, H. Chen, Y. Shen, J. Zhang, X. Qu, The effect of microstructure and rock mineralogy on water imbibition characteristics in tight reservoirs, J. Nat. Gas Sci. Eng. 34 (2016) 1461–1471.

[129] T.D. Blake, Slip between a liquid and a solid: D.M. Tolstoi's (1952) theory reconsidered, Colloids and Surfaces. 47 (1990) 135–145. https://doi.org/10.1016/0166-6622(90)80068-F.

[130] M. Whitby, L. Cagnon, M. Thanou, N. Quirke, Enhanced fluid flow through nanoscale carbon pipes, Nano Lett. 8 (2008) 2632–2637. https://doi.org/10.1021/nl080705f.

[131] J.A. Thomas, A.J.H. McGaughey, O. Kuter-Arnebeck, Pressure-driven water flow through carbon nanotubes: Insights from molecular dynamics simulation, Int. J. Therm. Sci. 49 (2010) 281–289. https://doi.org/10.1016/j.ijthermalsci.2009.07.008.

[132] J.K. Holt, H.G. Park, Y. Wang, M. Stadermann, A.B. Artyukhin, C.P. Grigoropoulos, A. Noy, O. Bakajin, Fast mass transport through sub-2-nanometer carbon nanotubes, 312 (2006) 1034–1038.

[133] C. Cottin-Bizonne, B. Cross, A. Steinberger, E. Charlaix, Boundary slip on smooth hydrophobic surfaces: Intrinsic effects and possible artifacts, Phys. Rev. Lett. 94 (2005) 1–4. https://doi.org/10.1103/PhysRevLett.94.056102.

[134] J.L. Barrat, L. Bocquet, Large slip effect at a nonwetting fluid-solid interface, Phys. Rev. Lett. 82 (1999) 4671–4674. https://doi.org/10.1103/PhysRevLett.82.4671.

[135] O.I. Vinogradova, Implications of hydrophobic slippage for the dynamic measurements of hydrophobic forces, Langmuir. 14 (1998) 2827–2837. https://doi.org/10.1021/la970332q.

[136] J. Janeček, R.R. Netz, Interfacial water at hydrophobic and hydrophilic surfaces: Depletion versus adsorption, Langmuir. 23 (2007) 8417–8429. https://doi.org/10.1021/la700561q.

[137] D.M. Huang, C. Sendner, D. Horinek, R.R. Netz, L. Bocquet, Water slippage versus contact angle: A quasiuniversal relationship, Phys. Rev. Lett. 101 (2008) 1–4. https://doi.org/10.1103/PhysRevLett.101.226101.

[138] G. Nagayama, P. Cheng, Effects of interface wettability on microscale flow by molecular dynamics simulation, Int. J. Heat Mass Transf. 47 (2004) 501–513.

[139] C. Cottin-Bizonne, J.-L. Barrat, L. Bocquet, E. Charlaix, Low-friction flows of liquid at nanopatterned interfaces, Nat. Mater. 2 (2003) 237–240.

[140] V.S.J. Craig, C. Neto, D.R.M. Williams, Shear-Dependent boundary slip in an aqueous newtonian liquid, Phys. Rev. Lett. 87 (2001) 54504-1-54504–4. https://doi.org/10.1103/PhysRevLett.87.054504.

[141] F. Brochará, P.G. de Gennes, Shear-Dependent Slippage at a Polymer/Solid Interface, Langmuir. 8 (1992) 3033–3037. https://doi.org/10.1021/la00048a030.

[142] P.A. Thompson, S.M. Troian, A general boundary condition for liquid flow at solid surfaces, Nature. 389 (1997) 360–362. https://doi.org/10.1038/38686.

[143] Y. Zhu, S. Granick, Rate-Dependent Slip of Newtonian Liquid at Smooth Surfaces, Phys. Rev. Lett. 87 (2001) 1–4. https://doi.org/10.1103/PhysRevLett.87.096105.

[144] C. Neto, V.S.J. Craig, D.R.M. Williams, Evidence of shear-dependent boundary slip in newtonian liquids, Eur. Phys. J. E. 12 (2003) 59–62. https://doi.org/10.1140/epjed/e2003-01-015-3.

[145] M. Ma, L. Shen, J. Sheridan, Z. Liu, C. Chen, Q. Zheng, Friction law for water flowing in carbon nanotubes, ICONN 2010 - Proc. 2010 Int. Conf. Nanosci. Nanotechnol. (2010) 392–395. https://doi.org/10.1109/ICONN.2010.6045251.

[146] C. Cottin-Bizonne, S. Jurine, J. Baudry, J. Crassous, F. Restagno, E. Charlaix, Nanorheology: an investigation of the boundary condition at hydrophobic and hydrophilic interfaces, Eur. Phys. J. E. 9 (2002) 47–53.

[147] S.E. Campbell, G. Luengo, V.I. Srdanov, F. Wudl, J.N. Israelachvili, Very low viscosity at the solid–liquid interface induced by adsorbed C 60 monolayers, Nature. 382 (1996) 520–522.

[148] P. Joseph, P. Tabeling, Direct measurement of the apparent slip length, Phys. Rev. E. 71 (2005) 35303.

[149] R. Pit, H. Hervet, L. Léger, Friction and slip of a simple liquid at a solid surface, Tribol. Lett. 7 (1999) 147–152.

[150] O.I. Vinogradova, G.E. Yakubov, Dynamic effects on force measurements. 2. Lubrication and the atomic force microscope, Langmuir. 19 (2003) 1227–1234.

[151] E. Bonaccurso, M. Kappl, H.J. Butt, Hydrodynamic Force Measurements: Boundary Slip of Water on Hydrophilic Surfaces and Electrokinetic Effects, Phys. Rev. Lett. 88 (2002) 4. https://doi.org/10.1103/PhysRevLett.88.076103.

[152] R. Pit, H. Hervet, L. Léger, Direct experimental evidence of slip in hexadecane: solid interfaces, Phys. Rev. Lett. 85 (2000) 980–983. https://doi.org/10.1103/PhysRevLett.85.980.

[153] E. Lauga, M.P. Brenner, Dynamic mechanisms for apparent slip on hydrophobic surfaces, Phys. Rev. E - Stat. Physics, Plasmas, Fluids, Relat. Interdiscip. Top. 70 (2004) 7. https://doi.org/10.1103/PhysRevE.70.026311.

[154] D.A. Doshi, E.B. Watkins, J.N. Israelachvili, J. Majewski, Reduced water density at hydrophobic surfaces: Effect of dissolved gases, Proc. Natl. Acad. Sci. U. S. A. 102 (2005) 9458–9462. https://doi.org/10.1073/pnas.0504034102.

[155] P.G. De Gennes, On fluid/wall slippage, Langmuir. 18 (2002) 3413–3414. https://doi.org/10.1021/la0116342.

[156] L.Y. Wang, F.C. Wang, F.Q. Yang, H.A. Wu, Molecular kinetic theory of boundary slip on textured surfaces by molecular dynamics simulations, Sci. China Physics, Mech. Astron. 57 (2014) 2152–2160. https://doi.org/10.1007/s11433-014-5586-y.

[157] E. Bonaccurso, H.J. Butt, V.S.J. Craig, Surface Roughness and Hydrodynamic Boundary Slip of a Newtonian Fluid in a Completely Wetting System, Phys. Rev. Lett. 90 (2003) 4. https://doi.org/10.1103/PhysRevLett.90.144501.

[158] T.A. Ho, D. V. Papavassiliou, L.L. Lee, A. Strioloa, Liquid water can slip on a hydrophilic surface, Proc. Natl. Acad. Sci. U. S. A. 108 (2011) 16170–16175. https://doi.org/10.1073/pnas.1105189108.

[159] S.N. Jamadagni, R. Godawat, S. Garde, How surface wettability affects the binding, folding, and dynamics of hydrophobic polymers at interfaces, Langmuir. 25 (2009) 13092–13099. https://doi.org/10.1021/la9011839.

[160] L. Gao, T.J. Mccarthy, Teflon is Hydrophilic. Comments on Definitions of Hydrophobic, Shear versus Tensile Hydrophobicity , and Wettability Characterization, Langmuir. 24 (2008) 546–550.

[161] S.K. Kannam, B.D. Todd, J.S. Hansen, P.J. Daivis, How fast does water flow in carbon nanotubes?, J. Chem. Phys. 138 (2013). https://doi.org/10.1063/1.4793396.

[162] M. Majumder, N. Chopra, R. Andrews, B.J. Hinds, Nanoscale hydrodynamics: enhanced flow in carbon nanotubes, Nature. 438 (2005) 44.

[163] F. Du, L. Qu, Z. Xia, L. Feng, L. Dai, Membranes of vertically aligned superlong carbon nanotubes, Langmuir. 27 (2011) 8437–8443.

[164] X. Qin, Q. Yuan, Y. Zhao, S. Xie, Z. Liu, Measurement of the rate of water translocation through carbon nanotubes, Nano Lett. 11 (2011) 2173–2177.

[165] P. Koumoutsakos, R.L. Jaffe, T. Werder, J.H. Walther, On the validity of the no-slip condition in nanofluidics, (2003).

[166] K. Falk, F. Sedlmeier, L. Joly, R.R. Netz, L. Bocquet, Molecular origin of fast water transport in carbon nanotube membranes: Superlubricity versus curvature dependent friction, Nano Lett. 10 (2010) 4067–4073. https://doi.org/10.1021/nl1021046.

[167] T.G. Myers, Why are slip lengths so large in carbon nanotubes?, Microfluid. Nanofluidics. 10 (2011) 1141–1145.

[168] X. Gu, M. Chen, Shape dependence of slip length on patterned hydrophobic surfaces, Appl. Phys. Lett. 99 (2011) 63101.

[169] W. Xiong, J.Z. Liu, M. Ma, Z. Xu, J. Sheridan, Q. Zheng, Strain Engineering Water Transport in Graphene Nano-channels, (2011) 1–17. https://doi.org/10.1103/PhysRevE.84.056329.

[170] S. Kumar Kannam, B.D. Todd, J.S. Hansen, P.J. Daivis, Slip length of water on graphene: Limitations of non-equilibrium molecular dynamics simulations, J. Chem. Phys. 136 (2012). https://doi.org/10.1063/1.3675904.

[171] C. Neto, D.R. Evans, E. Bonaccurso, H.J. Butt, V.S.J. Craig, Boundary slip in Newtonian liquids: A review of experimental studies, Reports Prog. Phys. 68 (2005) 2859–2897. https://doi.org/10.1088/0034-4885/68/12/R05.

[172] J. Krim, Friction and energy dissipation mechanisms in adsorbed molecules and molecularly thin films, Adv. Phys. 61 (2012) 155–323. https://doi.org/10.1080/00018732.2012.706401.

[173] B.N. Balzer, M. Gallei, M. V. Hauf, M. Stallhofer, L. Wiegleb, A. Holleitner, M. Rehahn, T. Hugel, Nanoscale friction mechanisms at solid-liquid interfaces, Angew. Chemie - Int. Ed. 52 (2013) 6541–6544. https://doi.org/10.1002/anie.201301255.

[174] A.A. Chialvo, L. Vlcek, P.T. Cummings, Surface corrugation effects on the water-graphene interfacial and confinement behavior, J. Phys. Chem. C. 117 (2013) 23875–23886. https://doi.org/10.1021/jp408893b.

[175] C.H. Choi, U. Ulmanella, J. Kim, C.M. Ho, C.J. Kim, Effective slip and friction reduction in nanograted superhydrophobic microchannels, Phys. Fluids. 18 (2006). https://doi.org/10.1063/1.2337669.

[176] T. Chen, T. Liu, L.P. Wang, S. Chen, Relations between skin friction and other surface quantities in viscous flows, Phys. Fluids. 31 (2019). https://doi.org/10.1063/1.5120454.

[177] J. Baudry, E. Charlaix, A. Tonck, D. Mazuyer, Experimental evidence for a large slip effect at a nonwetting fluid-solid interface, Langmuir. 17 (2001) 5232–5236. https://doi.org/10.1021/la0009994.

[178] D.C. Tretheway, C.D. Meinhart, Apparent fluid slip at hydrophobic microchannel walls, Phys. Fluids. 14 (2002). https://doi.org/10.1063/1.1432696.

[179] J.M.P. Nicholson, H. Power, O. Tammisola, S. Hibberd, E.D. Kay, Fluid dynamics of the slip boundary condition for isothermal rimming flow with moderate inertial effects, Phys. Fluids. 31 (2019). https://doi.org/10.1063/1.5085497.

[180] K. Wang, L. Yang, Y. Yu, G. Hou, Influence of slip boundary on the hydrofoil with a curved slip boundary condition for the lattice Boltzmann method, Phys. Fluids. 30 (2018). https://doi.org/10.1063/1.5052323.

[181] N. Tiwari, J.M. Davis, Influence of boundary slip on the dynamics and stability of thermocapillary spreading with a significant gravitational counterflow, Phys. Fluids. 26 (2014). https://doi.org/10.1063/1.4898566.

[182] H.P. Jennissen, Boundary-layer exchange by bubble: A novel method for generating transient nanofluidic layers, Phys. Fluids. 17 (2005). https://doi.org/10.1063/1.1990207.

[183] M.D. Ma, L. Shen, J. Sheridan, J.Z. Liu, C. Chen, Q. Zheng, Friction of water slipping in carbon nanotubes, Phys. Rev. E - Stat. Nonlinear, Soft Matter Phys. 83 (2011) 1–7. https://doi.org/10.1103/PhysRevE.83.036316.

[184] L. Bocquet, J.L. Barrat, Hydrodynamic boundary conditions, correlation functions, and Kubo relations for confined fluids, Phys. Rev. E. 49 (1994) 3079–3092. https://doi.org/10.1103/PhysRevE.49.3079.

[185] L. Bocquet, J.L. Barrat, On the Green-Kubo relationship for the liquid-solid friction coefficient, J. Chem. Phys. 139 (2013). https://doi.org/10.1063/1.4816006.

[186] K. Huang, I. Szlufarska, Green-Kubo relation for friction at liquid-solid interfaces, Phys. Rev. E - Stat. Nonlinear, Soft Matter Phys. 89 (2014). https://doi.org/10.1103/PhysRevE.89.032119.

[187] M. Rodahl, B. Kasemo, On the measurement of thin liquid overlayers with the quartz-crystal microbalance, Int. Conf. Solid-State Sensors Actuators, Eurosensors IX, Proc. 2 (1995) 743–746. https://doi.org/10.1016/S0924-4247(97)80002-7.

[188] K. Falk, F. Sedlmeier, L. Joly, R.R. Netz, L. Bocquet, Ultralow liquid/solid friction in carbon nanotubes: Comprehensive theory for alcohols, alkanes, OMCTS, and water, Langmuir. 28 (2012) 14261–14272. https://doi.org/10.1021/la3029403.

[189] H. Zeng, M. Tirrell, J. Israelachvili, Limit cycles in dynamic adhesion and friction processes: A discussion, J. Adhes. 82 (2006) 933–943. https://doi.org/10.1080/00218460600875979.

[190] U.D. Schwarz, O. Zwörner, P. Köster, R. Wiesendanger, Quantitative analysis of the frictional properties of solid materials at low loads. II. Mica and germanium sulfide, Phys. Rev. B - Condens. Matter Mater. Phys. 56 (1997) 6997–7000. https://doi.org/10.1103/PhysRevB.56.6997.

[191] H. Yoshizawa, Y.L. Chen, J. Israelachvili, Fundamental mechanisms of interfacial friction. 1. Relation between adhesion and friction, J. Phys. Chem. 97 (1993) 4128–4140. https://doi.org/10.1021/j100118a033.

[192] R. Szoszkiewicz, B. Bhushan, B.D. Huey, A.J. Kulik, G. Gremaud, Correlations between adhesion hysteresis and friction at molecular scales, J. Chem. Phys. 122 (2005). https://doi.org/10.1063/1.1886751.

[193] M. Nosonovsky, B. Bhushan, Multiscale friction mechanisms and hierarchical surfaces in nano- and bio-tribology, Mater. Sci. Eng. R Reports. 58 (2007) 162–193. https://doi.org/10.1016/j.mser.2007.09.001.

[194] F.P. Bowden, F.P. Bowden, D. Tabor, The friction and lubrication of solids, Oxford university press, 2001.

[195] B. Bhushan, Introduction to tribology, John Wiley & Sons, 2013.

[196] M.J. Sutcliffe, S.R. Taylor, A. Cameron, Molecular asperity theory of boundary friction, Wear. 51 (1978) 181–192. https://doi.org/10.1016/0043-1648(78)90065-0.

[197] Z. Chen, M.R. Vazirisereshk, A. Khajeh, A. Martini, S.H. Kim, Effect of Atomic Corrugation on Adhesion and Friction: A Model Study with Graphene Step Edges, J. Phys. Chem. Lett. 10 (2019) 6455–6461. https://doi.org/10.1021/acs.jpclett.9b02501.

[198] Y. Peng, Z. Wang, K. Zou, Friction and Wear Properties of Different Types of Graphene Nanosheets as Effective Solid Lubricants, Langmuir. 31 (2015) 7782–7791. https://doi.org/10.1021/acs.langmuir.5b00422.

[199] Z. Ye, P. Egberts, G.H. Han, A.T.C. Johnson, R.W. Carpick, A. Martini, Load-Dependent Friction Hysteresis on Graphene, ACS Nano. 10 (2016) 5161–5168. https://doi.org/10.1021/acsnano.6b00639.

[200] J.S. Ellis, M. Thompson, Slip and coupling phenomena at the liquid-solid interface, Phys. Chem. Chem. Phys. 6 (2004) 4928–4938. https://doi.org/10.1039/b409342a.

[201] H. Lee, H. Jeong, J. Suh, W.H. Doh, J. Baik, H.J. Shin, J.H. Ko, J. Wu, Y.H. Kim, J.Y. Park, Nanoscale Friction on Confined Water Layers Intercalated between MoS2 Flakes and Silica, J. Phys. Chem. C. 123 (2019) 8827–8835. https://doi.org/10.1021/acs.jpcc.8b11426.

[202] M.B. Elinski, B.D. Menard, Z. Liu, J.D. Batteas, Adhesion and Friction at Graphene/Self-Assembled Monolayer Interfaces Investigated by Atomic Force Microscopy, J. Phys. Chem. C. 121 (2017) 5635–5641. https://doi.org/10.1021/acs.jpcc.7b00012.

[203] J. Li, W. Cao, J. Li, M. Ma, J. Luo, Molecular Origin of Superlubricity between Graphene and a Highly Hydrophobic Surface in Water, J. Phys. Chem. Lett. 10 (2019) 2978–2984. https://doi.org/10.1021/acs.jpclett.9b00952.

[204] A. Porras-Vazquez, L. Martinie, P. Vergne, N. Fillot, Independence between friction and velocity distribution in fluids subjected to severe shearing and confinement, Phys. Chem. Chem. Phys. 20 (2018) 27280–27293. https://doi.org/10.1039/c8cp04620d.

[205] B. Gecim, W.O. Winer, Lubricant limiting shear stress effect on EHD film thickness, (1980).

[206] M. Nosonovsky, Model for solid-liquid and solid-solid friction of rough surfaces with adhesion hysteresis, J. Chem. Phys. 126 (2007). https://doi.org/10.1063/1.2739525.

[207] S. Lichter, A. Roxin, S. Mandre, Mechanisms for liquid slip at solid surfaces, Phys. Rev. Lett. 93 (2004) 1–4. https://doi.org/10.1103/PhysRevLett.93.086001.

[208] J.L. Barrat, L. Bocquet, Influence of wetting properties on hydrodynamic boundary conditions at a fluid/solid interface, Faraday Discuss. (1999) 119–127.

[209] E. Bertrand, T.D. Blake, J. De Coninck, Influence of solid-liquid interactions on dynamic wetting: A molecular dynamics study, J. Phys. Condens. Matter. 21 (2009). https://doi.org/10.1088/0953-8984/21/46/464124.

[210] S. Supple, N. Quirke, Molecular dynamics of transient oil flows in nanopores I: Imbibition speeds for single wall carbon nanotubes, J. Chem. Phys. 121 (2004) 8571–8579.

[211] A. Hamraoui, K. Thuresson, T. Nylander, V. Yaminsky, Can a dynamic contact angle be understood in terms of a friction coefficient?, J. Colloid Interface Sci. 226 (2000) 199–204.

[212] M.A. Tenan, S. Hackwood, G. Beni, Friction in capillary systems, J. Appl. Phys. 53 (1982) 6687–6692.

[213] G. Martic, T.D. Blake, J. De Coninck, Dynamics of imbibition into a pore with a heterogeneous surface, Langmuir. 21 (2005) 11201–11207.

[214] S. Kelly, C. Torres-Verdín, M.T. Balhoff, Anomalous liquid imbibition at the nanoscale: The critical role of interfacial deformations, Nanoscale. 8 (2016) 2751–2767. https://doi.org/10.1039/c5nr04462f.

[215] K. Wu, Z. Chen, J. Li, X. Li, J. Xu, X. Dong, Wettability effect on nanoconfined water flow, Proc. Natl. Acad. Sci. U. S. A. 114 (2017) 3358–3363. https://doi.org/10.1073/pnas.1612608114.

[216] P.A. Thompson, M.O. Robbins, Shear flow near solids: Epitaxial order and flow boundary conditions, Phys. Rev. A. 41 (1990) 6830–6837. https://doi.org/10.1103/PhysRevA.41.6830.

[217] R.S. Voronov, D. V. Papavassiliou, L.L. Lee, Review of fluid slip over superhydrophobic surfaces and its dependence on the contact angle, Ind. Eng. Chem. Res. 47 (2008) 2455–2477. https://doi.org/10.1021/ie0712941.

[218] D. Feng, X. Li, X. Wang, J. Li, T. Zhang, Z. Sun, M. He, Q. Liu, J. Qin, S. Han, Capillary filling of confined water in nanopores: coupling the increased viscosity and slippage, Chem. Eng. Sci. 186 (2018) 228–239.

[219] S. Gruener, T. Hofmann, D. Wallacher, A. V. Kityk, P. Huber, Capillary rise of water in hydrophilic nanopores, Phys. Rev. E - Stat. Nonlinear, Soft Matter Phys. 79 (2009) 6–9. https://doi.org/10.1103/PhysRevE.79.067301.

[220] N. Tas, J. Haneveld, H. Jansen, N. Brunets, J. Van, Capillarity effects in silicon based nanochannels, 85 (2004) 5363.

[221] J. Haneveld, N.R. Tas, N. Brunets, H. V. Jansen, M. Elwenspoek, Capillary filling of sub- 10 nm nanochannels, J. Appl. Phys. 104 (2008). https://doi.org/10.1063/1.2952053.

[222] S.E. Jarlgaard, M.B.L. Mikkelsen, P. Skafte-Pedersen, H. Bruus, A. Kristensen, Capillary filling speed in silicon dioxide nanochannels, 2006 NSTI Nanotechnol. Conf. Trade Show - NSTI Nanotech 2006 Tech. Proc. 2 (2006) 521–523.

[223] T.Q. Vo, M. Barisik, B. Kim, Near-surface viscosity effects on capillary rise of water in nanotubes, Phys. Rev. E - Stat. Nonlinear, Soft Matter Phys. 92 (2015) 1–8. https://doi.org/10.1103/PhysRevE.92.053009.

[224] L. Li, Y. Kazoe, K. Mawatari, Y. Sugii, T. Kitamori, Viscosity and wetting property of water confined in extended nanospace simultaneously measured from highly-pressurized meniscus motion, J. Phys. Chem. Lett. 3 (2012) 2447–2452. https://doi.org/10.1021/jz3009198.

[225] R.J. Jiang, F.Q. Song, H.M. Li, Flow characteristics of deionized water in microtubes, Chinese Phys. Lett. 23 (2006) 3305–3308. https://doi.org/10.1088/0256-307X/23/12/051.

[226] S. Semal, T.D. Blake, V. Geskin, M.J. De Ruijter, G. Castelein, J. De Coninck, Influence of surface roughness on wetting dynamics, Langmuir. 15 (1999) 8765–8770.

[227] S. Ahadian, H. Mizuseki, Y. Kawazoe, On the kinetics of the capillary imbibition of a simple fluid through a designed nanochannel using the molecular dynamics simulation approach, J. Colloid Interface Sci. 352 (2010) 566–572.

[228] V.M. Starov, M.G. Velarde, Wetting and spreading dynamics, CRC press, 2019.

[229] H. Eyring, Viscosity, plasticity, and diffusion as examples of absolute reaction rates, J. Chem. Phys. 4 (1936) 283–291. https://doi.org/10.1063/1.1749836.

[230] S. Glasstone, H. Eyring, K.J. Laidler, The theory of rate processes, McGraw-Hill, 1941.

[231] B.W. Cherry, C.M. Holmes, Kinetics of wetting of surfaces by polymers, J. Colloid Interface Sci. 29 (1969) 174–176. https://doi.org/10.1016/0021-9797(69)90367-1.

[232] G.D. Yarnold, B.J. Mason, A Theory of the Angle of Contact, Proc. Phys. Soc. Sect. B. 62 (1949) 121.

[233] T.D. Blake, J.M. Haynes, Kinetics of liquidliquid displacement, J. Colloid Interface Sci. 30 (1969) 421–423.

[234] T.D. Blake, The physics of moving wetting lines, J. Colloid Interface Sci. 299 (2006) 1–13.

[235] G. Martic, F. Gentner, D. Seveno, J. De Coninck, T.D. Blake, The possibility of different time scales in the dynamics of pore imbibition, J. Colloid Interface Sci. 270 (2004) 171–179.

[236] G. Martic, F. Gentner, D. Seveno, D. Coulon, J. De Coninck, T.D. Blake, A molecular dynamics simulation of capillary imbibition, Langmuir. 18 (2002) 7971–7976.

[237] A. Noy, H.G. Park, F. Fornasiero, J.K. Holt, C.P. Grigoropoulos, O. Bakajin, Nanofluidics in carbon nanotubes, Nano Today. 2 (2007) 22–29.

[238] S. Das, C. Narayanam, S. Roy, R. Khanna, A model of wetting of partially wettable porous solids by thin liquid films, Chem. Eng. J. 320 (2017) 104–115. https://doi.org/10.1016/j.cej.2017.02.151.

[239] N.R. Tas, J. Haneveld, H. V Jansen, M. Elwenspoek, A. van den Berg, Capillary filling speed of water in nanochannels, Appl. Phys. Lett. 85 (2004) 3274–3276.

[240] W.B. Hardy, III. The spreading of fluids on glass, London, Edinburgh, Dublin Philos. Mag. J. Sci. 38 (1919) 49–55.

[241] P. Bahadur, P.S. Yadav, K. Chaurasia, A. Leh, R. Tadmor, Chasing drops: Following escaper and pursuer drop couple system, J. Colloid Interface Sci. 332 (2009) 455–460.

[242] D. Ausserré, A.M. Picard, L. Léger, Existence and role of the precursor film in the spreading of polymer liquids, Phys. Rev. Lett. 57 (1986) 2671.

[243] V.J. Novotny, A. Marmur, Wetting autophobicity, J. Colloid Interface Sci. 145 (1991) 355–361.

[244] A. Marmur, M.D. Lelah, The dependence of drop spreading on the size of the solid surface, J. Colloid Interface Sci. 78 (1980) 262–265.

[245] M.N. Popescu, G. Oshanin, S. Dietrich, A.M. Cazabat, Precursor films in wetting phenomena, J. Phys. Condens. Matter. 24 (2012) 1–51. https://doi.org/10.1088/0953-8984/24/24/243102.

[246] J.R. Philip, Unitary approach to capillary condensation and adsorption, J. Chem. Phys. 66 (1977) 5069–5075. https://doi.org/10.1063/1.433814.

[247] P.G. De Gennes, Wetting: Statics and dynamics, Rev. Mod. Phys. 57 (1985) 827–863. https://doi.org/10.1103/RevModPhys.57.827.

[248] H. Hervet, Dynamics of Wetting: Precursor Film on Dry Solid, CR Acad. Sci. II. 299 (1984) 499–503.

[249] L.H. Tanner, The spreading of silicone oil drops on horizontal surfaces, J. Phys. D. Appl. Phys. 12 (1979) 1473.

[250] O. V Voinov, Hydrodynamics of wetting, Fluid Dyn. 11 (1976) 714–721.

[251] D.H. Bangham, Z. Saweris, The behaviour of liquid drops and adsorbed films at cleavage surfaces of mica, Trans. Faraday Soc. 34 (1938) 554–570.

[252] Q. Yuan, Y.P. Zhao, Precursor film in dynamic wetting, electrowetting, and electro-elasto-capillarity, Phys. Rev. Lett. 104 (2010) 16–19. https://doi.org/10.1103/PhysRevLett.104.246101.

[253] B.J. Ackerson, P.N. Pusey, Shear-induced order in suspensions of hard spheres, Phys. Rev. Lett. 61 (1988) 1033.

[254] M. Cieplak, J. Koplik, J.R. Banavar, Boundary conditions at a fluid-solid interface, Phys. Rev. Lett. 86 (2001) 803–806. https://doi.org/10.1103/PhysRevLett.86.803.

[255] S. Romero-Vargas Castrillón, N. Giovambattista, I.A. Aksay, P.G. Debenedetti, Structure and energetics of thin film water, J. Phys. Chem. C. 115 (2011) 4624–4635.

[256] H. Sakuma, K. Kawamura, Structure and dynamics of water on muscovite mica surfaces, Geochim. Cosmochim. Acta. 73 (2009) 4100–4110.

[257] T. Zhang, F. Javadpour, X. Li, K. Wu, J. Li, Y. Yin, Mesoscopic method to study water flow in nanochannels with different wettability, Phys. Rev. E. 102 (2020) 1–17. https://doi.org/10.1103/PhysRevE.102.013306.

[258] L. Leger, J.F. Joanny, Liquid spreading, Reports Prog. Phys. 55 (1992) 431.

[259] J.F. Joanny, Dynamics of wetting: Interface profile of a spreading liquid, J. Mécanique Théorique Appliquée. (1986) 249–271.

[260] J.F. Joanny, P.-G. De Gennes, Upward creep of a wetting fluid: a scaling analysis, J. Phys. 47 (1986) 121–127.

[261] S. Villette, M.P. Valignat, A.M. Cazabat, L. Jullien, F. Tiberg, Wetting on the molecular scale and the role of water. A case study of wetting of hydrophilic silica surfaces, Langmuir. 12 (1996) 825–830.

[262] N. Fraysse, M.P. Valignat, A.M. Cazabat, F. Heslot, P. Levinson, The spreading of layered microdroplets, J. Colloid Interface Sci. 158 (1993) 27–32.

[263] V.J. Novotny, Migration of liquid polymers on solid surfaces, J. Chem. Phys. 92 (1990) 3189–3196.

[264] M. Voué, M.P. Valignat, G. Oshanin, A.M. Cazabat, J. De Coninck, Dynamics of spreading of liquid microdroplets on substrates of increasing surface energies, Langmuir. 14 (1998) 5951–5958.

[265] J.F. Kincaid, H. Eyring, A.E. Stearn, The theory of absolute reaction rates and its application to viscosity and diffusion in the liquid state, Chem. Rev. 28 (1941) 301–365. https://doi.org/10.1021/cr60090a005.

[266] W. Zhong, D. Tomanek, First-principles theory of atomic-scale friction, 64 (1990) 3054–3057.

[267] J.E. Sacco, J.B. Sokoloff, A. Widom, Dynamical friction in sliding condensed-matter systems, Phys. Rev. B. 20 (1979) 5071–5083. https://doi.org/10.1103/PhysRevB.20.5071.

[268] S. Lichter, A. Martini, R.Q. Snurr, Q. Wang, Liquid slip in nanoscale channels as a rate process, Phys. Rev. Lett. 98 (2007) 1–4. https://doi.org/10.1103/PhysRevLett.98.226001.

[269] A. Martini, A. Roxin, R.Q. Snurr, Q. Wang, S. Lichter, Molecular mechanisms of liquid slip, J. Fluid Mech. 600 (2008) 257–269. https://doi.org/10.1017/S0022112008000475.

[270] S. Plimpton, Fast parallel algorithms for short-range molecular dynamics, J. Comput. Phys. 117 (1995) 1–19.

[271] A. Stukowski, Visualization and analysis of atomistic simulation data with OVITO-the Open Visualization Tool, Model. Simul. Mater. Sci. Eng. 18 (2010). https://doi.org/10.1088/0965-0393/18/1/015012.

[272] P. Hänggi, P. Talkner, M. Borkovec, Reaction-rate theory: Fifty years after Kramers, Rev. Mod. Phys. 62 (1990) 251–341. https://doi.org/10.1103/RevModPhys.62.251.

[273] T. Ala-Nissila, R. Ferrando, S.C. Ying, Collective and single particle diffusion on surfaces, Adv. Phys. 51 (2002) 949–1078. https://doi.org/10.1080/00018730110107902.

[274] J.S. Babu, S.P. Sathian, The role of activation energy and reduced viscosity on the enhancement of water flow through carbon nanotubes, J. Chem. Phys. 134 (2011). https://doi.org/10.1063/1.3592532.

[275] A.T. Celebi, C.T. Nguyen, R. Hartkamp, A. Beskok, The role of water models on the prediction of slip length of water in graphene nanochannels, J. Chem. Phys. 151 (2019). https://doi.org/10.1063/1.5123713.

[276] F. Sofos, T. Karakasidis, A. Liakopoulos, Transport properties of liquid argon in krypton nanochannels: Anisotropy and non-homogeneity introduced by the solid walls, Int. J. Heat Mass Transf. 52 (2009) 735–743. https://doi.org/10.1016/j.ijheatmasstransfer.2008.07.022.

[277] E. Wagemann, J.H. Walther, E.R. Cruz-Chú, H.A. Zambrano, Water Flow in Silica Nanopores Coated by Carbon Nanotubes from a Wetting Translucency Perspective, J. Phys. Chem. C. 123 (2019) 25635–25642. https://doi.org/10.1021/acs.jpcc.9b05294.

[278] S. Faucher, N. Aluru, M.Z. Bazant, D. Blankschtein, A.H. Brozena, J. Cumings, J. Pedro De Souza, M. Elimelech, R. Epsztein, J.T. Fourkas, A.G. Rajan, H.J. Kulik, A. Levy, A. Majumdar, C. Martin, M. McEldrew, R.P. Misra, A. Noy, T.A. Pham, M. Reed, E. Schwegler, Z. Siwy, Y.

Wang, M. Strano, Critical Knowledge Gaps in Mass Transport through Single-Digit Nanopores: A Review and Perspective, J. Phys. Chem. C. 123 (2019) 21309–21326. https://doi.org/10.1021/acs.jpcc.9b02178.

[279] S.K. Kannam, B.D. Todd, J.S. Hansen, P.J. Daivis, Slip flow in graphene nanochannels, J. Chem. Phys. 135 (2011). https://doi.org/10.1063/1.3648049.

[280] R.B. Bird, Transport phenomena, Appl. Mech. Rev. 55 (2002) R1–R4.

[281] F. Persson, L.H. Thamdrup, M.B.L. Mikkelsen, S.E. Jaarlgard, P. Skafte-Pedersen, H. Bruus, A. Kristensen, Double thermal oxidation scheme for the fabrication of SiO2 nanochannels, Nanotechnology. 18 (2007) 245301.

[282] H.A. Zambrano, J.H. Walther, R.L. Jaffe, Molecular dynamics simulations of water on a hydrophilic silica surface at high air pressures, J. Mol. Liq. 198 (2014) 107–113. https://doi.org/10.1016/j.molliq.2014.06.003.

[283] F. Jabbari, A. Rajabpour, S. Saedodin, S. Wongwises, Effect of water/carbon interaction strength on interfacial thermal resistance and the surrounding molecular nanolayer of CNT and graphene flake, J. Mol. Liq. 282 (2019) 197–204. https://doi.org/10.1016/j.molliq.2019.03.003.

[284] T.K. Tokunaga, DLVO-based estimates of adsorbed water film thicknesses in geologic CO2 reservoirs, Langmuir. 28 (2012) 8001–8009.

[285] N. V. Churaev, G. Starke, J. Adolphs, Isotherms of capillary condensation influenced by formation of adsorption films. 1. Calculation for model cylindrical and slit pores, J. Colloid Interface Sci. 221 (2000) 246–253. https://doi.org/10.1006/jcis.1999.6592.

[286] N. V Churaev, Contact angles and surface forces, Adv. Colloid Interface Sci. 58 (1995) 87–118.

[287] H. Ye, H. Zhang, Z. Zhang, Y. Zheng, Size and temperature effects on the viscosity of water inside carbon nanotubes, Nanoscale Res. Lett. 6 (2011) 1–5. https://doi.org/10.1186/1556-276X-6-87.

[288] F. Persson, L.H. Thamdrup, M.B.L. Mikkelsen, S.E. Jaarlgard, P. Skafte-Pedersen, H. Bruus, A. Kristensen, Double thermal oxidation scheme for the fabrication of SiO2 nanochannels, Nanotechnology. 18 (2007). https://doi.org/10.1088/0957-4484/18/24/245301.

[289] W. Ouyang, W. Wang, Fabrication and characterization of sub-100/10 nm planar nanofluidic channels by triple thermal oxidation and silicon-glass anodic bonding, Biomicrofluidics. 8 (2014) 52106.

[290] M.A. Alibakhshi, Q. Xie, Y. Li, C. Duan, Accurate measurement of liquid transport through nanoscale conduits, Sci. Rep. 6 (2016) 24936.

[291] L.H. Thamdrup, F. Persson, H. Bruus, A. Kristensen, H. Flyvbjerg, Experimental investigation of bubble formation during capillary filling of Si O 2 nanoslits, Appl. Phys. Lett. 91 (2007) 163505.

[292] H.-H. Liu, B. Lai, J. Chen, Unconventional spontaneous imbibition into shale matrix: theory and a methodology to determine relevant parameters, Transp. Porous Media. 111 (2016) 41–57.

[293] P. Kim, H.-Y. Kim, J.K. Kim, G. Reiter, K.Y. Suh, Multi-curvature liquid meniscus in a nanochannel: Evidence of interplay between intermolecular and surface forces, Lab Chip. 9 (2009) 3255–3260.

[294] S. Kelly, M.T. Balhoff, C. Torres-Verdín, Quantification of bulk solution limits for liquid and interfacial transport in nanoconfinements, Langmuir. 31 (2015) 2167–2179. https://doi.org/10.1021/la504742w.

[295] N.R. Haria, G.S. Grest, C.D. Lorenz, Viscosity of nanoconfined water between hydroxyl basal surfaces of kaolinite: Classical simulation results, J. Phys. Chem. C. 117 (2013) 6096–6104. https://doi.org/10.1021/jp312181u.

[296] N. Wei, X. Peng, Z. Xu, Breakdown of fast water transport in graphene oxides, Phys. Rev. E - Stat. Nonlinear, Soft Matter Phys. 89 (2014) 1–8. https://doi.org/10.1103/PhysRevE.89.012113.

[297] Z. Qin, M.J. Buehler, Nonlinear Viscous Water at Nanoporous Two-Dimensional Interfaces Resists High-Speed Flow through Cooperativity, Nano Lett. 15 (2015) 3939–3944. https://doi.org/10.1021/acs.nanolett.5b00809.

[298] J. Petravic, P. Harrowell, Spatial dependence of viscosity and thermal conductivity through a planar interface, J. Phys. Chem. B. 113 (2009) 2059–2065.

[299] H.C. Hamaker, The London-van der Waals attraction between spherical particles, Physica. 4 (1937) 1058–1072. https://doi.org/10.1016/S0031-8914(37)80203-7.

[300] S. Lee, W.M. Sigmund, AFM study of repulsive van der Waals forces between Teflon AF^{TM} thin film and silica or alumina, Colloids Surfaces A Physicochem. Eng. Asp. 204 (2002) 43–50.

[301] R.S. Voronov, D. V. Papavassiliou, L.L. Lee, Boundary slip and wetting properties of interfaces: Correlation of the contact angle with the slip length, J. Chem. Phys. 124 (2006). https://doi.org/10.1063/1.2194019.

[302] T. Qian, X.P. Wang, P. Sheng, Molecular scale contact line hydrodynamics of immiscible flows, Phys. Rev. E - Stat. Physics, Plasmas, Fluids, Relat. Interdiscip. Top. 68 (2003) 15. https://doi.org/10.1103/PhysRevE.68.016306.

[303] T. Qian, X.-P. Wang, P. Sheng, Molecular hydrodynamics of the moving contact line in two-phase immiscible flows, (2005) 1–36. http://arxiv.org/abs/cond-mat/0510403.

[304] J.F. Gerbeau, T. Lelièvre, Generalized Navier boundary condition and geometric conservation law for surface tension, Comput. Methods Appl. Mech. Eng. 198 (2009) 644–656. https://doi.org/10.1016/j.cma.2008.09.011.

[305] A.M.P. Boelens, J.J. De Pablo, Generalised Navier boundary condition for a volume of fluid approach using a finite-volume method, Phys. Fluids. 31 (2019). https://doi.org/10.1063/1.5055036.

[306] H. Li, X.C. Zeng, Wetting and interfacial properties of water nanodroplets in contact with graphene and monolayer boron–nitride sheets, ACS Nano. 6 (2012) 2401–2409.

[307] G. Tocci, L. Joly, A. Michaelides, Friction of water on graphene and hexagonal boron nitride from Ab initio methods: Very different slippage despite very similar interface structures, Nano Lett. 14 (2014) 6872–6877. https://doi.org/10.1021/nl502837d.

[308] C.-J. Shih, Q.H. Wang, S. Lin, K.-C. Park, Z. Jin, M.S. Strano, D. Blankschtein, Breakdown in the wetting transparency of graphene, Phys. Rev. Lett. 109 (2012) 176101.

[309] F. Taherian, V. Marcon, N. F. A. van der Vegt, F. Leroy, What Is the Contact Angle of Water on Graphene?, Langmuir. 29 (2013) 1457–1465. https://doi.org/10.1021/la304645w.

[310] T. Werder, J.H. Walther, R.L. Jaffe, T. Halicioglu, P. Koumoutsakos, On the water-carbon interaction for use in molecular dynamics simulations of graphite and carbon nanotubes, J. Phys. Chem. B. 107 (2003) 1345–1352. https://doi.org/10.1021/jp0268112.

[311] R.L. Jaffe, P. Gonnet, T. Werder, J.H. Walther, P. Koumoutsakos, Water-carbon interactions 2: Calibration of potentials using contact angle data for different interaction models, Mol. Simul. 30 (2004) 205–216. https://doi.org/10.1080/08927020310001659124.

[312] I. Pagonabarraga, B. Rotenberg, D. Frenkel, Recent advances in the modelling and simulation of electrokinetic effects: Bridging the gap between atomistic and macroscopic descriptions, Phys. Chem. Chem. Phys. 12 (2010) 9566–9580. https://doi.org/10.1039/c004012f.

[313] S.C. Yang, Effects of surface roughness and interface wettability on nanoscale flow in a nanochannel, Microfluid. Nanofluidics. 2 (2006) 501–511. https://doi.org/10.1007/s10404-006-0096-5.

[314] N. Ishida, T. Inoue, M. Miyahara, K. Higashitani, Nano bubbles on a hydrophobic surface in water observed by tapping-mode atomic force microscopy, Langmuir. 16 (2000) 6377–6380. https://doi.org/10.1021/la000219r.

[315] S. Granick, Y. Zhu, H. Lee, Slippery questions about complex fluids flowing past solids, Nat. Mater. 2 (2003) 221–227.

[316] E. Lauga, M. Brenner, H. Stone, Microfluidics: The No-Slip Boundary Condition, Springer Handb. Exp. Fluid Mech. (2007) 1219–1240. https://doi.org/10.1007/978-3-540-30299-5_19.

[317] P. Joseph, C. Cottin-Bizonne, J.M. Benoît, C. Ybert, C. Journet, P. Tabeling, L. Bocquet, Slippage ofWater Past Superhydrophobic Carbon Nanotube Forests in Microchannels, Phys. Rev. Lett. 97 (2006) 1–4. https://doi.org/10.1103/PhysRevLett.97.156104.

[318] P. Hajiani, F. Larachi, Reducing Taylor dispersion in capillary laminar flows using magnetically excited nanoparticles: Nanomixing mechanism for micro/nanoscale applications, Chem. Eng. J. 203 (2012) 492–498. https://doi.org/10.1016/j.cej.2012.05.030.

[319] S. Pal, K. Madane, A.A. Kulkarni, Antisolvent based precipitation: Batch, capillary flow reactor and impinging jet reactor, Chem. Eng. J. 369 (2019) 1161–1171. https://doi.org/10.1016/j.cej.2019.03.107.

[320] S.R. Gorthi, H.S. Gaikwad, P.K. Mondal, G. Biswas, Surface Tension Driven Filling in a Soft Microchannel: Role of Streaming Potential, Ind. Eng. Chem. Res. 59 (2020) 3839–3853. https://doi.org/10.1021/acs.iecr.9b00767.

[321] P. Randive, A. Dalal, K.C. Sahu, G. Biswas, P.P. Mukherjee, Wettability effects on contact line dynamics of droplet motion in an inclined channel, Phys. Rev. E - Stat. Nonlinear, Soft Matter Phys. 91 (2015) 1–16. https://doi.org/10.1103/PhysRevE.91.053006.

[322] D. Feng, X. Li, X. Wang, J. Li, T. Zhang, Z. Sun, M. He, Q. Liu, J. Qin, S. Han, Capillary filling of confined water in nanopores: Coupling the increased viscosity and slippage, Chem. Eng. Sci. 186 (2018) 228–239. https://doi.org/10.1016/j.ces.2018.04.055.

[323] J.M. Oh, T. Faez, S. De Beer, F. Mugele, Capillarity-driven dynamics of water-alcohol mixtures in nanofluidic channels, Microfluid. Nanofluidics. 9 (2010) 123–129. https://doi.org/10.1007/s10404-009-0517-3.

[324] P. Wu, A. Nikolov, D. Wasan, Capillary dynamics driven by molecular self-layering, Adv. Colloid Interface Sci. 243 (2017) 114–120. https://doi.org/10.1016/j.cis.2017.02.004.

[325] R. Sedev, The molecular-kinetic approach to wetting dynamics: Achievements and limitations, Adv. Colloid Interface Sci. 222 (2015) 661–669.

[326] T.D. Blake, J. De Coninck, The influence of solid–liquid interactions on dynamic wetting, Adv. Colloid Interface Sci. 96 (2002) 21–36.

[327] L. Zhang, K. Wu, Z. Chen, J. Li, X. Yu, S. Yang, G. Hui, M. Yang, Quasi-Continuum Water Flow under Nanoconfined Conditions: Coupling the Effective Viscosity and the Slip Length, Ind. Eng. Chem. Res. (2020).

[328] B.E. Novich, T.A. Ring, Colloid stability of clays using photon correlation spectroscopy, Clays Clay Miner. 32 (1984) 400–406.

[329] S. Takahashi, Water imbibition, electrical surface forces, and wettability of low permeability fractured porous media, Citeseer, 2009.

[330] D. Erickson, D. Li, C. Werner, An improved method of determining the ζ-potential and surface conductance, J. Colloid Interface Sci. 232 (2000) 186–197.

[331] S. Chibbaro, L. Biferale, F. Diotallevi, S. Succi, K. Binder, D. Dimitrov, A. Milchev, S. Girardo, D. Pisignano, Evidence of thin-film precursors formation in hydrokinetic and atomistic simulations of nano-channel capillary filling, Epl. 84 (2008). https://doi.org/10.1209/0295-5075/84/44003.

[332] K.V. Kumar, C. Valenzuela-Calahorro, J.M. Juarez, M. Molina-Sabio, J. Silvestre-Albero, F. Rodriguez-Reinoso, Hybrid isotherms for adsorption and capillary condensation of N2 at 77K on

porous and non-porous materials, Chem. Eng. J. 162 (2010) 424–429. https://doi.org/10.1016/j.cej.2010.04.058.

[333] I. V. Kuchin, O.K. Matar, R. V. Craster, V.M. Starov, Influence of the Disjoining Pressure on the Equilibrium Interfacial Profile in Transition Zone Between a Thin Film and a Capillary Meniscus, Colloids Interface Sci. Commun. 1 (2014) 18–22. https://doi.org/10.1016/j.colcom.2014.06.002.

[334] I. V. Kuchin, O.K. Matar, R. V. Craster, V.M. Starov, Modeling the effect of surface forces on the equilibrium liquid profile of a capillary meniscus, Soft Matter. 10 (2014) 6024–6037. https://doi.org/10.1039/c4sm01018c.

[335] M.P. Valignat, M. Voué, G. Oshanin, A.M. Cazabat, Structure and dynamics of thin liquid films on solid substrates, Colloids Surfaces A Physicochem. Eng. Asp. 154 (1999) 25–31.

[336] A.M. Cazabat, N. Fraysse, F. Heslot, P. Levinson, J. Marsh, F. Tiberg, M.P. Valignat, Pancakes, Adv. Colloid Interface Sci. 48 (1994) 1–17.

[337] F. Heslot, N. Fraysse, A.M. Cazabat, Molecular layering in the spreading of wetting liquid drops, Nature. 338 (1989) 640–642.

[338] F. Brochard, P.G. De Gennes, Spreading laws for liquid polymer droplets: interpretation of the «foot», J. Phys. Lettres. 45 (1984) 597–602.

[339] H. Verweij, M.C. Schillo, J. Li, Fast mass transport through carbon nanotube membranes, Small. 3 (2007) 1996–2004.

[340] J.S. Hansen, P.J. Daivis, K.P. Travis, B.D. Todd, Parameterization of the nonlocal viscosity kernel for an atomic fluid, Phys. Rev. E - Stat. Nonlinear, Soft Matter Phys. 76 (2007) 1–8. https://doi.org/10.1103/PhysRevE.76.041121.

[341] J.C. Rasaiah, S. Garde, G. Hummer, Water in nonpolar confinement: from nanotubes to proteins and beyond, Annu. Rev. Phys. Chem. 59 (2008) 713–740.

[342] C. Lutz, M. Kollmann, C. Bechinger, Single-file diffusion of colloids in one-dimensional channels, Phys. Rev. Lett. 93 (2004) 26001.